2011-04-27

Experimental Study of Liquid Squeeze-flow as it Relates to Human Voice Production

Daniel Victor Lo Forte
Brigham Young University - Provo

Experimental Study of Liquid Squeeze-Flow as it Relates to Human Voice Production

Daniel V. Lo Forte

A thesis submitted to the faculty of
Brigham Young University
in partial fulfillment of the requirements for the degree of

Master of Science

Scott L. Thomson, Chair
Steven E. Gorrell
R. Daniel Maynes

Department of Mechanical Engineering

Brigham Young University

June 2011

ABSTRACT

Experimental Study of Liquid Squeeze-Flow as it Relates to
Human Voice Production

Daniel V. Lo Forte
Department of Mechanical Engineering, BYU
Master of Science

Approximately 7.5 million people suffer from voice disorders in the United States. Previous studies indicate that the quality of the fluid layer that coats the vocal folds appears to be different for people with voice disorders than for people whose voice is considered normal. These studies suggest that the composition and/or physical properties of the fluid layer may contribute to voice disorders. Despite these findings, little research has been undertaken to investigate the role of the fluid layer on voice, and in almost all cases, the fluid layer is considered to be insignificant. The purpose of this reasearch was to investigate the role of the fluid layer and the potential it may have to influence voice production; particularly, to identify some aspects of the fluid layer that have the potential to contribute to voice disorders.

In order to investigate the potential significance of the effects of a fluid layer on vocal fold operation, an existing lumped model was modified to incorporate the Newtonian squeeze-flow equation as a fluid model during the colliding portion of the oscillatory cycle. Results indicated that thicker films produced more significant deviations from the case with no fluid layer.

Experimental testing was performed to validate existing analytical equations for squeezing flow of Newtonian and non-Newtonian fluids confined between parallel axisymmetric plates. Based on available published data on the rheological properties of the fluid layer found on the surface of the vocal folds, several fluids with a range of fluid properties were selected. Reasonable agreement was found for much of data collected for the Newtonian fluid cases within measurement tolerances. For the non-Newtonian cases, the constitutive equation was found to be in poor agreement with the measured physical characteristics of the selected non-Newtonian fluids. A summary of the collected experimental data is provided so that it can be used in for validation and comparison in future research.

A preliminary computational model based on the classical two-mass vocal fold model was implemented which incorporated squeezing effects of a thin Newtonian film of fluid on the surface of the vocal folds. Results indicated that the fluid layer may not be insignificant, although further tests and modeling are required.

Finally, different fluids were applied to a physical model of the vocal folds and measurements were taken to determine the effects of the application of fluid. The results showed significant changes in the vocal fold model response that indicated the fluid layer affects vocal fold operation in important ways. Some of the changes in response could not be attributed solely to the fluid layer. Suggestions regarding future work with physical model testing are given which may help clarify the effects of a fluid layer on vocal fold flow-induced vibration.

Keywords: squeeze flow, thin film, voice, airway surface liquid

ACKNOWLEDGMENTS

I am grateful for the opportunity to pursue graduate work at Brigham Young University and to my Father in Heaven for enabling me to come to this point. It has truly been a blessing to be surrounded by so many good people both academically and otherwise.

I am thankful for my advisor Dr. Scott Thomson for his willingness and enthusiasm to provide me the opportunity for graduate studies. I appreciate his sincere encouragement at poignant times throughout my research as well as his insights which helped me progress in my work.

I would like to thank the other members of my committee Dr. Daniel Maynes, and Dr. Steve Gorrell for the time they spent reviewing my work and providing valuable feedback.

I am especially grateful for the funding I received through research and teaching assistantships from both the Mechanical Engineering Department and the National Institute of Deafness and Other Communicative Disorders. As a result, I was able to focus on my work full-time.

I would like to thank Preston Murray and Kevin Cole for their invaluable help. Working with Preston on the synthetic models allowed me to accomplish so much more than I would have otherwise. He always had good ideas and a willingness and enthusiasm to work hard. A substantial component of my research required instrumentation for which Kevin's knowledge and experience was critical. Both are outstanding individuals with whom it would be a great joy to work with.

I am thankful for my wife, Kim, for her support, and for our children Dallin, Kaeden, Lexi, and Kate. I am so thankful for their constant love and the joy that comes into my life from them.

TABLE OF CONTENTS

LIST OF TABLES

LIST OF FIGURES

CHAPTER 1. INTRODUCTION

1.1 Overview

In almost all professions, verbal communication is essential. However, 7.5 million people in the United States suffer from voice disorders that impede or eliminate their ability to speak [1]. In particular, there are a variety of voice disorders which occur as a result of vocal abuse or misuse. During periods of prolonged or excessive use, the vocal folds can become injured.

While vibration and the repeated collision of the vocal folds occurs during normal operation, adverse conditions can lead to voice disorders (dysphonias). The source of many voice disorders is presumed to be the result of severe contact stresses between the vocal folds as they vibrate and several studies have attempted to quantify these stresses [2–10]. During vocal fold motion, normal and tangential stresses are developed in the vocal fold tissues. These stresses may be amplified or damped by the presence and properties of the fluid layer (mucus layer) that coats the vocal folds. It is thought that the purpose of the fluid layer is to maintain hydration of the vocal fold and airway tissues. However, disease, diet, environment and medications can affect the liquid layer. For example, Hsiao et al. [11] observed individuals with and without laryngeal tension-fatigue syndrome and suggested that high mucus viscosity, mucus aggregation, and rough-looking mucus surface may exacerbate symptoms of the dysphonia. Presently there is insufficient data regarding the mechanical influence of the fluid layer on the vocal fold tissues.

The purpose of the research described in this thesis was primarily to determine if the fluid layer that coats the vocal folds has the potential to affect vocal fold operation. This was accomplished by: (1) experimentally measuring fluid forces for conditions similar to those found on real vocal folds and comparing the experimental measurements with existing fluid force equations, (2) applying a validated analytical model approximating a liquid layer to a numerical vocal fold model, and (3) observing the effects of fluid applied directly to a synthetic vocal fold model to predict its potential effect on real vocal fold operation. The experimental data obtained may also be used for

the validation of future numerical models of the fluid layer, and also help estimate fluid property parameter ranges in which vocal fold contact stresses may be influenced.

1.2 Background

1.2.1 Vocal Fold Anatomy

The vocal folds are tissues in the larynx that play a central role in generating sound for the human voice (see Fig. 1.1). This sound is produced when air from the lungs passes over the vocal folds, causing them to vibrate; this is known as phonation. During phonation, the vocal folds collide repeatedly against each other. During collision and the immediately succeeding separation, the fluid layers on each fold interact.

The vocal folds are composed of five layers of tissue (see Fig. 1.2) [12]. The deepest layer of the vocal folds is the thyroarytenoid muscle, next to which is the lamina propria. The lamina propria consists of three layers (superficial, intermediate, and deep) that differ in elasticity and thickness. The epithelium is a thin layer of cells that covers the superficial lamina propria. The vocal fold is often represented as consisting of three groupings of these layers: the body, the ligament, and the cover. The body is the muscle. The ligament consists of the intermediate and deep layers of the lamina propria. The cover is comprised of the superficial lamina propria and the epithelium. During phonation, the predominant feature of vocal fold vibration is a "mucosal wave" that propagates vertically along the surface of the cover layer.

The respiratory airway epithelium is coated with a thin fluid – the airway surface liquid, or ASL – which consists of two layers [15]. The "sol" layer consists of a thin (~6 μm) Newtonian fluid directly in contact with the epithelium [16]. This layer is covered by a non-Newtonian "mucus" layer reported to have a thickness of approximately 7 to 70 μm [17].

While the mucus layer has been measured *in vivo* at up to 70 μm [18, 19] in pigs and rats, others have reported that it may have a greater localized depth during phonation. Normally, a fluid layer of less than 70 μm [17] would not be visible using videolaryngostroboscopy. However, Hsiung [20] used videolaryngostroboscopy to view the vocal folds during phonation before and after surgery of patients with vocal nodules and found that mucus was visible on the vocal folds. This indicated much greater local depths of the fluid layer. Hsiao et al. [11] observed the vocal

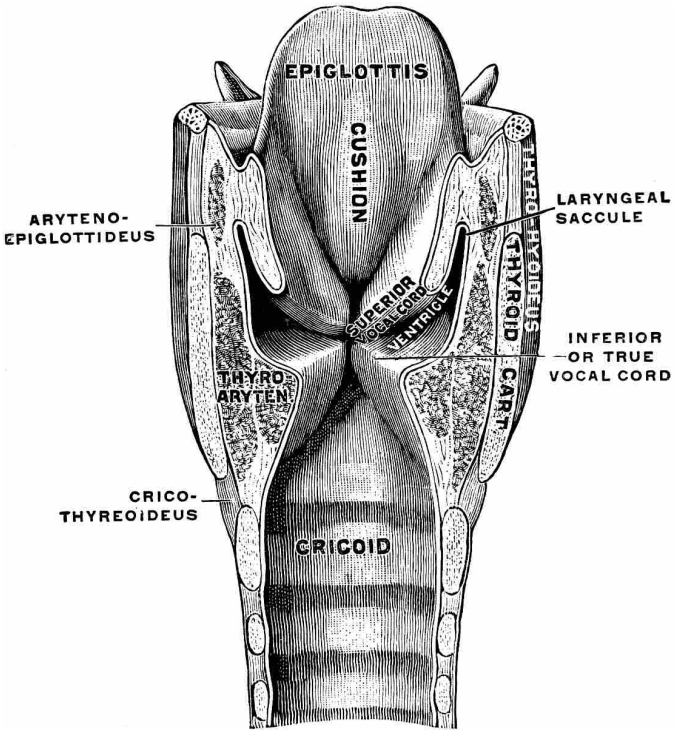

Figure 1.1: Coronal cross-section of the larynx. [13]

folds of a group of 301 individuals diagnosed with laryngeal tension-fatigue syndrome and another group of 25 vocally-normal individuals. He used videostrobolaryngoscopy to view the glottis at rest prior to phonation, during phonation, and at rest after phonation. He reported that 61% of the patients had visible mucus during phonation and that sometimes the mucus was "sticky" enough so that 1 or 2 "threads" of fluid bridged across the folds. He also reported that mucus was not always visible when the vocal folds were at rest. He also found that the mucus surface was more uneven on subjects with tension-fatigue syndrome than those without the disorder. In a recent study, Bonilha et al. [21] found visible mucus aggregation on 97% of the vocally normal subjects observed with videolaryngostroboscopy. Consequently, when studying the vocal fold region, it is necessary to consider fluid layers with depths greater than 70 μm.

Although a fluid layer is present on the vocal folds, it is not certain that there are distinct sol and mucus layers. The fluid for the sol layer is secreted by glands that open at and are located just beneath the epithelium. The mucus layer fluid exists primarily due to the secretions of "goblet" cells, also located just beneath the epithelium. Short hair-like structures called cilia (~6 μm long) cover the surface of the airway and are submerged in the sol layer. The depth of the sol layer

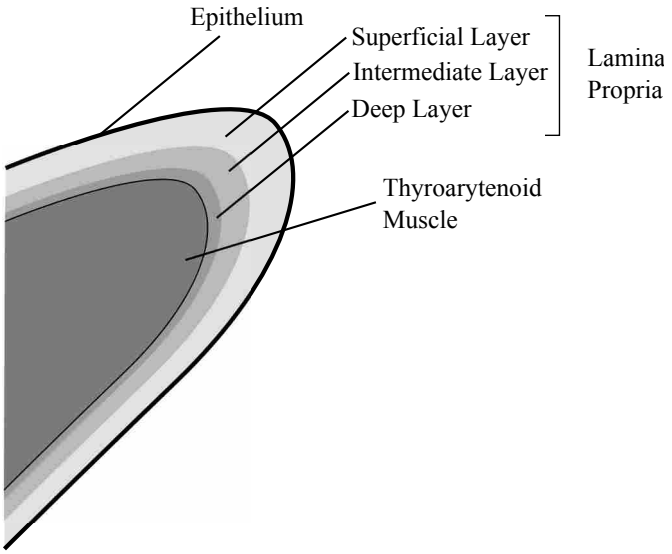

Figure 1.2: Vocal fold cross-section showing different layers of tissue, after [14].

was reported to be same as the length of the cilia [15]. The cilia help propel the ASL upwards through the airway. However, although these biological devices (cilia and fluid-secreting glands) cover most of the airway, none are found on the vocal fold surface itself [22]. The source of the fluid layer on the vocal folds is therefore unclear. There is a fluid exchange between the vocal fold tissues and the superficial fluid layer known as transepithelial ion and water fluxes that may help maintain the fluid layer properties [17, 23]. Despite the lack of information regarding the specific composition of the fluid on the vocal folds, a fluid layer is clearly found there and it is likely similar in composition to the ASL [22].

1.2.2 Vocal Fold Function

Prior to phonation, laryngeal muscles contract and bring opposing vocal folds into close proximity. The space between the vocal folds is called the glottis. The air pressure beneath the vocal folds is called the subglottal pressure. Sufficient subglottal pressure from the lungs (onset phonation threshold pressure) induces self-oscillation of the vocal folds. Self-oscillation occurs as energy imparted to the vocal folds from the air flow accelerates the vocal folds laterally outward, followed by lateral deceleration as the energy is absorbed and damped by the vocal fold tissue. The folds ultimately reverse direction and accelerate medially (toward the center). The self-oscillating process continues as long as the lung pressure remains above what is called the offset phonation

threshold pressure. Thus, onset phonation threshold pressure is the minimum pressure required to initiate self-oscillation, whereas offset phonation threshold pressure is the pressure at which the self-oscillation ceases. These oscillations–along with the corresponding fluctuations in airflow through the larynx–produce the sound for speech. The average frequency of oscillation is around 125 Hz for an adult male and 240 Hz for an adult female [24].

At low subglottal pressures, just above onset, the vocal folds begin to vibrate without touching. As the subglottal pressure is raised, the vocal folds begin to come into contact with each other and the fluid layers from each vocal fold come into contact with each other, merge, and form a liquid bridge that is sequentially squeezed, stretched, and that then ruptures.

1.2.3 Voice Disorders

Studies have been performed to discover the causes of voice disorders. One of the primary suspects is severe contact stresses. Some common voice disorders that can be caused by severe contact stresses are nodules, polyps, and contact ulcers. Nodules are small benign growths on the vocal folds and are the most common voice disorder. They are like callouses, usually form in pairs (one on each vocal fold), and form on the area of the vocal folds that are suspected to have the highest contact pressure during phonation (e.g., the central region of the vocal fold). Polyps are benign growths that are similar to nodules, but are softer and more like a blister than a callous. They most often form on only one vocal fold. Contact ulcers are less common, but are also caused by severe forces between the vocal folds during phonation or even gastroesophageal reflux. The surface tissues of the vocal folds become worn away and ulcerated sores form.

While the mere presence of a fluid layer has been shown to affect vocal fold operation [25], variation of the properties of the fluid layer likely affects the magnitude of those changes [26,27]. Several studies have sought to quantify the magnitude of vocal fold contact stresses during phonation ([2–5, 7–9, 28–33]). However, few, if any, have carefully investigated the role the fluid layer plays in the development of the contact stresses despite indications that a fluid layer appears to (1) affect vocal fold operation in significant ways and (2) is altered for subjects experiencing voice disorders [11, 20, 21]. Therefore, investigation of the effect of the fluid layer on vocal fold operation is necessary to determine its significance in terms of contact stresses and voice disorders.

1.3 Previous Work

It is presumed that contact stresses may be affected by the fluid layer [22]. During phonation, the fluid layer may dissipate impact energy during collision of the vocal folds, reducing contact stresses, and/or cause the adherence of the vocal folds during separation (e.g., liquid mediated adhesion), locally amplifying contact stresses. The contact stresses induced by the fluid layer are likely dependent on the specific fluid properties, such as viscosity. Previous studies indicate that hydration and the fluid layer may affect vocal fold operation [25, 34–40]. It has been suggested that the aggregation of fluid and/or the increased viscosity of the fluid layer may locally amplify contact stresses between the vocal folds during phonation, perhaps causing the development of voice disorders, but also exacerbating the symptoms of existing voice disorders [21, 22, 41]. However, none of these studies have attempted to quantify the mechanical stress induced in the vocal fold tissues by the fluid layer or suggest critical fluid properties for which induced stresses could damage vocal fold tissues.

1.3.1 Previous Experimental Testing of Fluid Layer on Vocal Fold Operation

Studies indicate that hydration and the properties of the fluid layer alter vocal fold operation. Jiang et al. [36] observed that phonation threshold pressure (PTP) decreased with re-hydration of excised canine larynges which were initially dehydrated with warm, dry air and then re-hydrated with humidified air. Verdolini et al. [34, 42] found that systemic dehydration resulted in an increased PTP. Sivasankar and Fisher [38] reported that oral breathing for 15 minutes increased PTP and concluded this to be a result of superficial drying of the vocal fold mucosa. They later posited that superficial laryngeal dehydration caused increases in PTP in a separate study [43]. Aside from oral breathing, secretory (surface) dehydration may result from pathological conditions (e.g., diabetes), pharmacological agents (e.g., antihistamines), and environmental factors (e.g., extended phonation in low-humidity air-conditioned environments) [39, 40]. Ayache et al. [25] applied an artificial mucus (xanthan gum polymer mixture) of two different viscosities to freshly excised porcine (pig) larynges and observed that the fundamental frequency decreased, while vocal fold contact time increased.

While these studies provide evidence that the properties of the vocal fold liquid layer may alter vocal fold vibration, they have not directly studied the fluid layer or the contact stresses that exist between vocal folds or within the vocal fold tissues during phonation. It is thus expedient to collect experimental data to elucidate the role of the fluid layer on vocal fold operation. Further indications that the fluid layer is significant could then warrant the development of fluid layer models for application in future finite element and/or reduced-order models that could be used for the study of the fluid layer and its effects.

In order to perform the research described in this thesis, a fluid closely approximating the fluid layer found on human vocal folds must be used. However, as was discussed previously, the precise source and properties of the liquid layer covering the vocal folds is unclear. Some attempts have been made to measure the rheological properties of mucus [44]. However, certain studies indicate that the exact composition, and consequently, the fluid properties of the liquid layer may be affected by the inhalation [26] and/or swallowing of substances [27]. Therefore, for the purposes of this research, a range of fluid properties must be tested in order to determine the potential effects of the liquid layer on vocal fold operation. Effort was made to obtain a mucus gel simulant with properties similar to published data [44].

1.3.2 Vocal Fold Modeling

Due to inherent difficulties associated with *in vivo* and excised vocal fold study, computational and synthetic models are often used. Reduced-order and lumped parameter computational models are attractive because of the minimal computational cost, but they lack the spatial resolution of higher-order finite element models. Reduced-order models include the single-mass model [45] (a self-oscillating model driven by the average of the inlet and outlet pressures of the glottis), the two-mass model [46], a self-oscillating model which captures the fundamental converging-diverging nature of the vocal fold tissues, a body-cover model [47] which incorporates primary differences in tissue properties between the deep and superficial layers of the vocal fold, and multi-mass models [48, 49] which aim to resolve finer details of vocal fold vibration. Additionally, many finite element models have been developed and studied [32, 33, 50, 51]. Alipour, et al. [50] developed a two-dimensional, three-layered, continuum model with varying tissue properties. Thomson et al. [51] used a two-dimensional, fluid-structure interaction, continuum model and compared the

results with experimental results obtained from a synthetic, silicone, physical model of the same dimensions and physical properties. Tao and Jiang [32, 33] used a quasi-three-dimensional, self-oscillating, continuum model to study impact pressures. In both reduced-order and finite element simulations, simplifying assumptions are made to reduce complexity and computational time. To the author's knowledge, the effects of the fluid layer on phonation have typically been considered to be negligible and thus have been excluded from prior computational models.

Alternatively, synthetic models have been developed and used in the study of voice production (e.g., [51]). Synthetic models have certain advantages over computational models. Synthetic models exhibit complex physical phenomena that can be difficult to model accurately, such as turbulence, three-dimensional geometric effects, contact modeling, and nonlinear material properties. Additionally, the application of a liquid layer to the vocal fold tissues in a self-oscillating finite-element model with accurate contact force modeling is a non-trivial problem that could perhaps be more easily studied using physical models.

1.4 Research Overview

The research described in this thesis consisted of three experimental tests utilizing Newtonian and non-Newtonian fluids. First, oscillatory and colliding/separating squeeze-flow testing of three Newtonian and three non-Newtonian fluids was performed in which simultaneous force and film thickness measurements were recorded. The data obtained from this testing validated the Newtonian squeeze flow equation and qualified its use as a liquid layer model to be incorporated into a computational vocal fold model. Second, the Newtonian squeeze-flow equation was incorporated into a lumped parameter model during the closing phase of vocal fold vibration. The results of this model warranted the further investigation of the effects of the liquid layer on a synthetic model. Third, the effects of three Newtonian and two non-Newtonian fluids (simulating human mucus) on the flow-induced vibratory response of a synthetic vocal fold model was tested. Simultaneous intraglottal force, subglottal pressure, radiated sound, and high speed image data of the model during vibration were recorded. Dry and wet cases were compared to ascertain the effects of the liquid layer on the synthetic model's vibratory patterns.

1.5 Outline of Thesis

Chapter 2 explains fundamental rheological principles. These principles help describe important characteristics of the Newtonian and non-Newtonian fluids which were used as a substitute for the liquid found on human vocal folds. An explanation of the definitions and measurement methods used for viscoelastic fluid properties is given. A description of the Newtonian squeeze-flow equation used in this work and its assumptions is given. Finally, the equations used for squeeze-flow of a non-Newtonian, Maxwell fluid and its assumptions are given.

Chapter 3 describes the experimental methods used for oscillatory and colliding/separating flow testing which was performed. Experimental results validating the Newtonian squeeze-flow equation for use as a liquid layer model are given. An analysis of the non-Newtonian squeeze-flow equation and its potential as an appropriate liquid layer model is discussed. A description of all of the test setups and the experimental methods used to collect and analyze measured data is given. The potential of the liquid layer to affect vocal fold operation is discussed.

Chapter 4 describes the modification of the classical two-mass vocal fold model to incorporate a Newtonian liquid layer model. Preliminary results which indicate the potential effects of a liquid layer on voice are given. The limitations of the present model and the need for a more refined model are discussed.

Chapter 5 describes the experimental testing that was performed using a synthetic vocal fold model during vibration with the application of a liquid layer. A novel method for the measurement of force during model vibration, both wet and dry, is described. Results indicating the potential effects of a liquid layer on vocal fold operation are discussed. The meaning of the results is applied theoretically to human vocal fold operation.

Chapter 6 briefly summarizes significant results, outlines the primary contributions, and gives a brief discussion of potential areas for future work in the study of the liquid layer on human vocal fold operation and other related areas of research.

CHAPTER 2. THIN-FILM SQUEEZE-FLOW THEORY

2.1 Fluid Rheology

Rheology is the study of the deformation and flow of matter. A description of the rheological tests used to determine the relevant flow properties for this work are here discussed. The following discussion stems from that provided in [52].

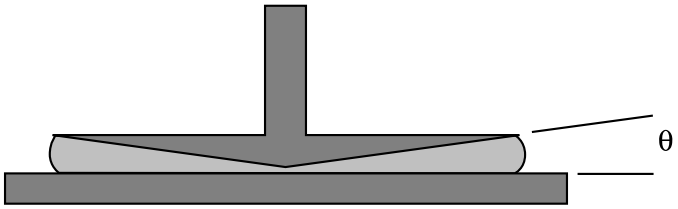

Figure 2.1: Cone and plate geometry

Shear stresses can be applied to a fluid using many different geometric configurations, one of which is a cone and plate geometry (see Fig. 2.1). Fluid fills the gap between the cone and plate, and as the cone is rotated, Couette flow is very nearly approximated between the cone and plate. The shear stress applied to the fluid can be computed directly from the torque applied to the cone. Strain is calculated from the angular displacement of the cone about its axis. Instruments for measuring fluid properties in this manner are called rheometers. Fluid properties for this thesis research were obtained using the TA Instruments AR 2000ex Rheometer.

Fluids can be divided into two major groups based on the relationship between shear stress and shear strain rate. If the relationship is linear in a particular region, the fluid is considered to be a Newtonian fluid in that region. Non-linear stress-strain rate behavior is classified as non-Newtonian. In the case of a Newtonian fluid, the shear stress is simply related to the shearing strain rate by a proportionality constant called dynamic viscosity, μ, as shown:

$$\sigma = \mu \dot{\gamma}, \tag{2.1}$$

where σ is shear stress, and $\dot{\gamma}$ is shearing strain rate. The fluid property viscosity is generally temperature-dependent and tends to decrease with increasing temperature for liquids. The relative sensitivity of viscosity to temperature varies among fluids.

Non-Newtonian fluids are grouped into specific categories based on the relationship between shearing stress and shearing strain rate. If the slope of the shearing stress to strain rate curve decreases with increasing strain rate, the fluid is classified as pseudo-plastic or shear-thinning. Fluids for which the slope of the shearing stress to strain rate curve increases with increasing strain rate are termed dilatant or shear-thickening.

Another property of non-Newtonian fluids is the relative change in shear stress with time when a constant shearing strain rate is applied. If shear stress increases in time for a constant strain rate, the fluid is called rheopectic. Fluids with decreasing stress in time are thixotropic. Fluids with no change in shear stress are termed time-independent. Viscoelastic fluids have both viscous and elastic components which cause them to both flow and elastically deform.

Creep is the strain history of a substance when subjected to an applied stress. A creep test for a fluid is performed by applying a constant shear stress, σ, and measuring the resulting strain versus time, $\gamma(t)$. If strain continues to be measured after the sudden removal of the applied shear stress, this is called a creep-relaxation test.

In dynamic tests, an oscillating, sinusoidal angular displacement of angular frequency, ω, is applied to the cone in a cone and plate configuration, and the torque is measured over time. The shearing stress and strain are calculated from the torque and angular displacement. The applied shearing strain is represented by

$$\gamma(t) = \gamma_0 \sin(\omega t), \tag{2.2}$$

where $\gamma(t)$ is strain history and γ_0 is the amplitude of the strain. The stress is also sinusoidal in the steady-state for linear viscoelastic materials, but lags behind the applied strain by a factor, δ,

known as the loss angle, or loss tangent, as described below:

$$\begin{aligned}\sigma(\omega,t) &= \sigma_0 \sin(\omega t + \delta), \\ &= \sigma_0 [\sin(\omega t)\cos\delta + \cos(\omega t)\sin\delta],\end{aligned} \tag{2.3}$$

where σ_0 is the amplitude of the oscillatory stress and ω is the angular frequency. Letting the storage or elastic modulus $G' = \frac{\sigma_0}{\gamma_0}\cos\delta$ and the viscous, or loss, modulus $G'' = \frac{\sigma_0}{\gamma_0}\sin\delta$, Eq. 2.3 can be rewritten as

$$\sigma(\omega,t) = \gamma_0 [G' \sin(\omega t) + G'' \cos(\omega t)]. \tag{2.4}$$

Figure 2.2 shows an example of the stress and strain histories during an oscillatory test.

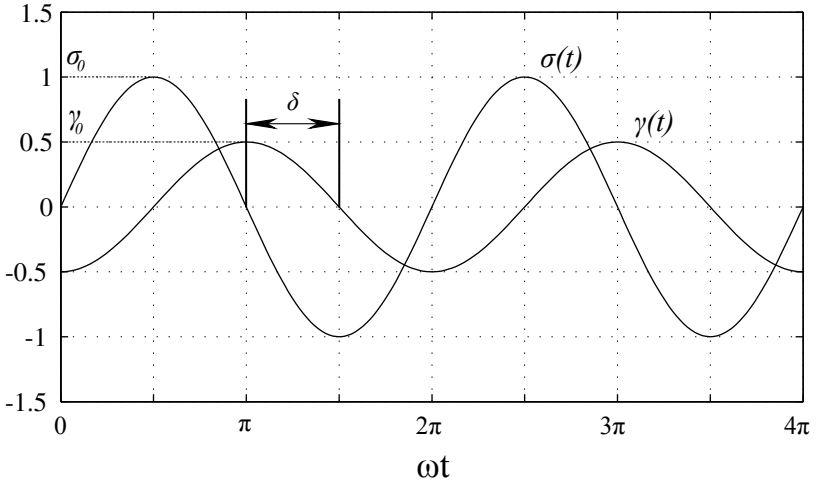

Figure 2.2: Example of an oscillatory test. $\sigma(t)$ is the stress history, $\gamma(t)$ is the strain history, δ is the loss tangent, σ_0 is the peak stress, and γ_0 is the peak strain (after [52]).

G' characterizes the elastic contributions of a material and is known as the elastic or storage modulus. G'' characterizes the viscous contributions and is known as the loss modulus. As an example, an ideal linear viscous material (such as a Newtonian fluid) would have $G'' = \eta\omega$, $\delta = \frac{\pi}{2}$, where η = constant viscosity. An ideal linear elastic material would have $G' = G_e$ and $\delta = 0$, where G_e is the shear modulus [52].

Lumped parameter models can be used to approximate the behavior of non-Newtonian fluids, or more specifically, to relate the shear stress to the shearing strain rate of a fluid. Lumped

parameter models use idealized spring and damper elements. For example, a purely viscous or Newtonian fluid can be represented as an idealized damper. A purely elastic material, such as an idealized cross-linked rubber, can be represented by a spring element. As described below, combinations of these elements are used to model more complex fluids.

Many non-Newtonian fluids have both viscous and elastic properties and are hence called viscoelastic. The simplest representation of a viscoelastic fluid is a Maxwell fluid and is represented as a spring and damper in series (see Fig. 2.3).

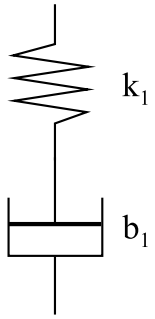

Figure 2.3: A Maxwell material model is represented as a spring and damper in series (after [52]).

A representative plot of the strain history of a Maxwell fluid during a creep-relaxation test is illustrated in Figure 2.4. Upon application of a shear stress, the fluid is immediately strained inversely proportional to the representative spring constant k_1 (see Fig. 2.3). During the period of time while the shear stress is held constant, the fluid maintains a constant shearing strain rate, $\dot{\gamma}$. This is seen in Fig. 2.4 as the linearly increasing strain on the left-hand side of the plot. The shear strain rate, $\dot{\gamma}$, is inversely proportional to the corresponding linear damping constant b_1 (see Fig. 2.3). After a period of time, t_0, the applied stress is removed and the fluid strain, γ rebounds suddenly as the potential energy stored in the elastic component is released. This is seen in the figure as the sudden drop in strain, γ at time t_0. The strain of the fluid, γ, then remains constant after the removal of applied stress.

Another simple material model is the Kelvin-Voigt model where a spring and damper are placed in parallel (see Fig. 2.5). Figure 2.6 shows the resulting strain versus time plot of a Kelvin-Voigt model subjected to a creep-relaxation test. There can be no sudden strain displacement in this case since the damper will not allow sudden displacement. The strain will increase logarith-

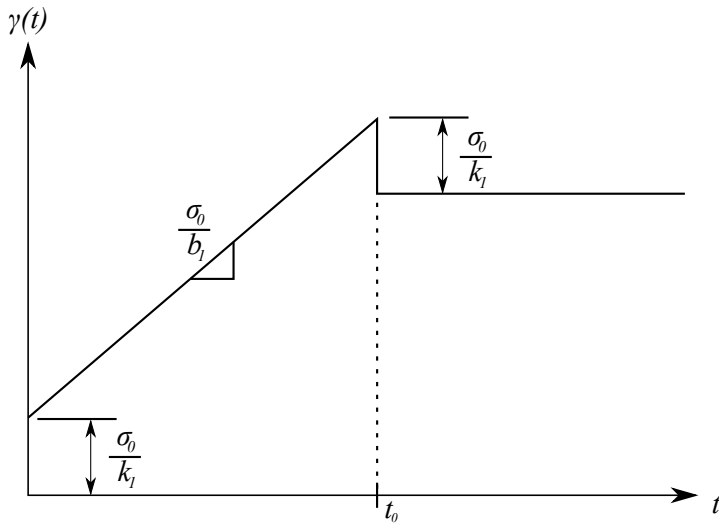

Figure 2.4: Maxwell model creep test (after [52]).

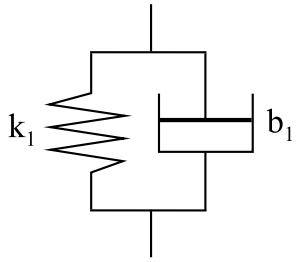

Figure 2.5: Kelvin-Voigt model.

mically till the stress in the spring element exactly equals the applied stress at which point the strain displacement will remain constant. When the stress is suddenly removed, the spring element dissipates its potential energy through the damper element in an exponential fashion. Kelvin-Voigt materials are typical of cross-linked solids, like rubber, for which there is no net flow of the material. The material's shear strain returns to the original state after removal of the applied stress as opposed to a fluid where there is a net positive strain, or net flow.

More generalized models of non-Newtonian fluids can be made by combining Maxwell and Kelvin-Voigt and/or other spring and damper elements in series and parallel. One such example is the Burgers model that incorporates the Maxwell and Kelvin-Voigt fluid models in series (see Fig. 2.7).

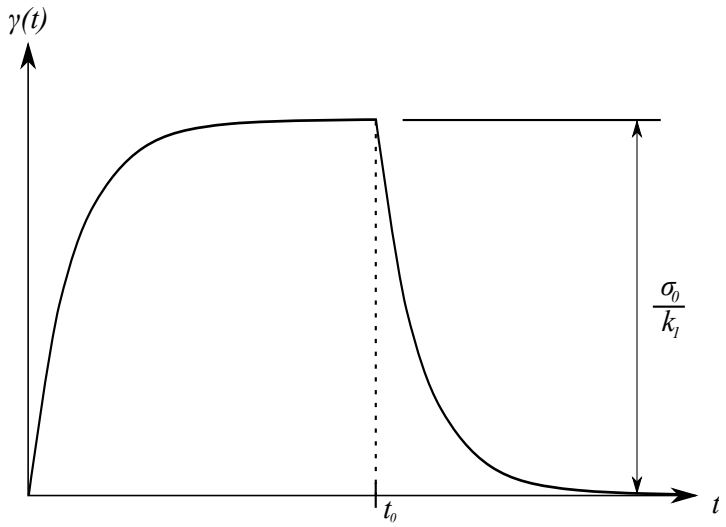

Figure 2.6: Kelvin-Voigt model creep test (after [52]).

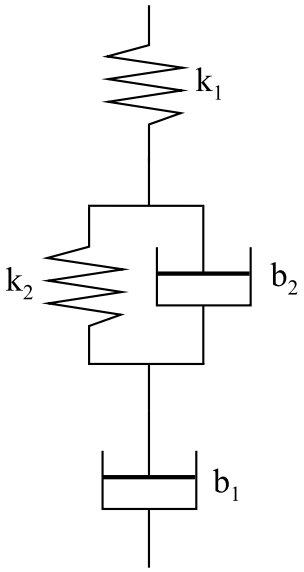

Figure 2.7: Burgers model.

Figure 2.8 shows the resulting strain history of a Burgers fluid subjected to a creep-relaxation test. One can observe the effects of both models immediately. There is a sudden strain upon application of the shear stress followed by a decay of strain rate to a constant rate over some initial period of time. Immediately following removal of the shear stress, there is a sudden retraction of strain followed by a slower decay of strain to some positive value as the fluid releases the energy

stored in the Kelvin-Voigt spring. Unlike the Kelvin-Voigt model alone, there is a net flow of a Burgers fluid as seen by the difference between the initial and final strains.

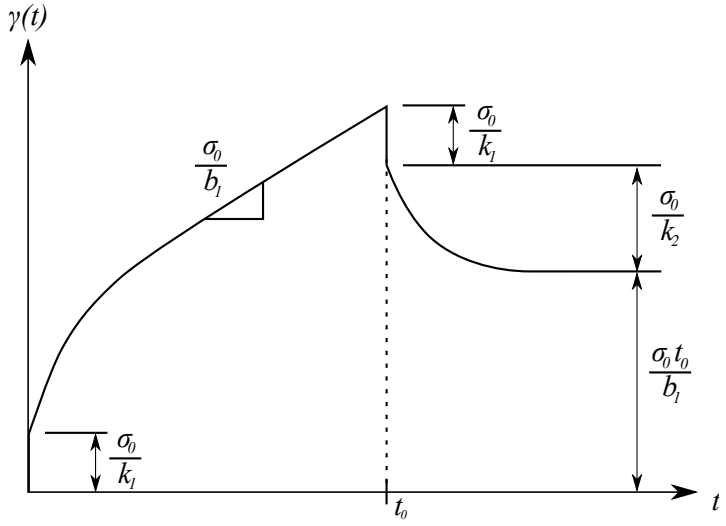

Figure 2.8: Burgers model creep test. (after [52])

The response of a dynamic system to an input depends on the frequency of the input. For example, a damper acts as a low-pass filter. At very low frequencies, the damper flows freely, barely resisting the input movement. At high frequencies the displacement is severely damped. Likewise, the response of a non-Newtonian fluid depends on the frequency of the shear stress to which it is subjected.

As a result of a fluid's frequency-dependent nature, certain approximations can be made based on the relative values of the components of a fluid model. For example, as either the Kelvin-Voigt spring constant, k_2, or damper constant, b_2, in a Burgers fluid are increased, the model approaches a Maxwell model approximation at high frequencies. Likewise, as the Maxwell fluid component values, k_1 and b_1 are increased, the fluid approaches a Kelvin-Voigt fluid model.

Rheological testing showed that the non-Newtonian fluids used for this research were fit well by a Burgers model. However, there was a large difference between the relaxation times of the damping components. The short relaxation time was on the order of a fraction of a second, whereas the long relaxation time was on the order of hundreds of seconds. Since the lowest frequencies

of testing were above 5 Hz, this disparity between damping modes permitted the fluids to be approximated as Maxwell fluids and therefore a Maxwell fluid model for squeeze flow was used.

2.2 Newtonian Squeeze-Flow

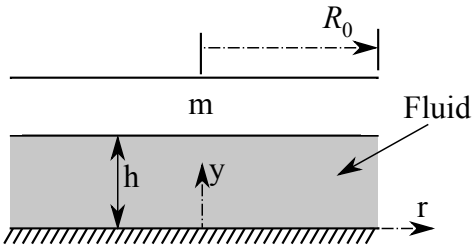

Figure 2.9: Dimensions and coordinate system for thin film squeeze-flow equation. Film thickness, h, is much less than the disk radius, R_0. Squeeze velocity is the rate of change of film thickness, $\dot{h}$, where the overdot denotes the temporal derivative.

The derivation for the pressure distribution in a Newtonian, laminar, thin-film squeeze-flow between parallel disks was given by Constantinescu [53]. The equation uses an approximate velocity profile across the thickness of the film (discussed below) that is valid when the wall shear stress is greater than zero (e.g., the flow is not separating at the walls), and friction stresses on the two surfaces are not directly influenced by inertia forces. According to this derivation, the pressure distribution P within a thin, cylindrical, Newtonian film between approaching/separating parallel disks is

$$P(r,t) = P_a - \frac{1}{2}\left[\frac{6\mu\dot{h}}{h^3}\left(1 - \frac{1+\frac{3\alpha}{2}}{12\mu}\rho h\dot{h}\right) + \frac{\rho\ddot{h}}{2h}\right]\left(R_0^2 - r^2\right), \tag{2.5}$$

where P_a is ambient pressure (surrounding the film), h is film thickness (see Fig. 2.9; over-dots denote derivative with respect to time), μ and ρ are fluid dynamic viscosity and density, respectively, R_0 is film radius, and α is a correction factor representing the velocity profile of the film. A value of $\alpha = 1$ corresponds to a constant velocity profile (e.g., slug flow), a value of 1.33 represents Couette flow, and a value of $\alpha = 1.54$, represents Poiseuille flow. Since the plates were only moving in the direction normal to the film, a value of $\alpha = 1.54$ was used (this is the same value used by

Constantinescu for parallel disk squeeze-flow). In the experiments described herein, the fluid entirely filled the gap between the disks and beyond as shown schematically in Fig. 2.10, so that the value used for R_0 was a constant and equal to the radius of the smaller upper disk. Surface tension effects only existed beyond the gap and were assumed negligible in comparison to the viscous and inertial forces due to the small film thicknesses (< 1000 μm).

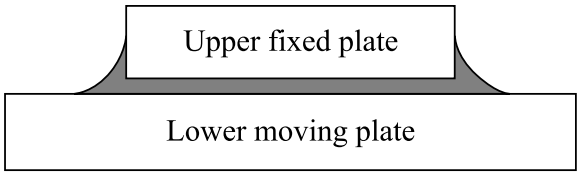

Figure 2.10: Fluid entirely fills the gap between plates and beyond perimeter of smaller, upper plate. There are no bubbles in the fluid.

Integrating Eq. 2.5 over the disk surface area and neglecting P_a (so that $P(r,t)$ is gauge pressure in the fluid) gives

$$F_y = \frac{\pi R_0^4}{4}\left[\frac{6\mu\dot{h}}{h^3}\left(1-\frac{1+\frac{3\alpha}{2}}{12\mu}\rho h\dot{h}\right)+\frac{\rho\ddot{h}}{2h}\right], \tag{2.6}$$

where F_y is the reactive force that the film exerts on the disks. Applying Newton's second law to a disk of mass m yields

$$m\ddot{h} = F_y - F, \tag{2.7}$$

where F is the sum of all other forces acting on the disk in the negative y-direction (squeezing direction). Solving Eq. 2.7 for acceleration, $\ddot{h}$, and using Eq. 2.6 gives

$$\ddot{h} = \frac{16h^3F + 2h\dot{h}^2\pi R_0^4\rho + 3\alpha h\dot{h}^2\pi R_0^4\rho - 24\dot{h}\mu\pi R_0^4}{2\dot{h}^2\left(\pi R_0^4\rho + 8hm\right)}. \tag{2.8}$$

Integrating Eq. 2.8 twice numerically gives the film thickness as a function of time. The initial conditions for h and $\dot{h}$ were the measured film thickness and rate of change of film thickness at the initial time.

In the case where the displacement is known *a priori* (e.g., prescribed displacement), the film force can be estimated directly using Eq. 2.6. Equation 2.6 is used to estimate the peak

force under oscillation, colliding, and separating conditions. The calculated peak force was then compared with the measured peak force to evaluate the accuracy of the equation in predicting the film force.

2.3 Non-Newtonian Squeeze-Flow (Maxwell Fluid)

A relation was derived by Hashimoto [54] that gives pressure as a function of radial coordinate of the squeezing flow of a viscoelastic fluid between parallel, axisymmetric, circular plates. The pressure function is

$$p(r) = \int_{r_a}^{r} \left(\frac{\partial p}{\partial r}\right) dr - j\frac{C_e \rho r_a^2 v_s^2}{8h^2}, \tag{2.9}$$

where $\frac{\partial p}{\partial r}$ is the pressure gradient in the radial direction (described below), r is the radial coordinate, C_e is the pressure loss coefficient (=2.0), ρ is the fluid density, r_a is the radius of the circular plate, v_s is squeeze velocity ($v_s = -\frac{\partial h}{\partial t}$), and h is the film thickness. The last term on the right hand side represents the entrance pressure drop due to inertia effects ($j = 0$ when the disks are approaching and $j = 1$ when the disks are separating).

The pressure gradient equation is

$$\frac{\partial p}{\partial r} = f - \frac{\rho}{h}\left\{\frac{r}{2}\frac{\partial v_s}{\partial t} + \frac{h^5}{120\mu^2}\left(\frac{G_1}{r} + 2\frac{\partial G_1}{\partial r}\right)G_1 + \frac{kh^5}{20\mu^2}\left(G_1 G_2 G_3 + fG_2\frac{\partial G_1}{\partial r} + fG_1\frac{\partial G_2}{\partial r}\right) + \frac{k^2h^5}{120\mu^2}\left(G_4 G_5 + f^2\frac{\partial G_5}{\partial r}\right)\right\}, \tag{2.10}$$

where G_1 through G_5 are defined as:

$$G_1 = f + a\frac{\partial f}{\partial t}, \tag{2.11a}$$

$$G_2 = b^2 + \frac{h^2}{21}f^2, \tag{2.11b}$$

$$G_3 = \frac{\partial f}{\partial r} + \frac{f}{r}, \tag{2.11c}$$

$$G_4 = \frac{f^2}{r} + 2f\frac{\partial f}{\partial r}, \tag{2.11d}$$

$$G_5 = \frac{h^4}{48}f^4 + b^2h^2f^2 + 9b^4, \tag{2.11e}$$

and f and b are the solutions of the following system of coupled differential equations:

$$\frac{\partial b}{\partial t} = \frac{1}{2}\frac{\partial h}{\partial t} f - \frac{1}{a}\left(b + k\frac{h^2}{4} f^2 b + k b^3\right), \tag{2.12}$$

$$\frac{\partial f}{\partial t} = -\frac{1}{a}\left(\frac{6\mu r v_s}{h^3} + f + \frac{3}{20} k h^2 f^3 + 3 k f b^2\right), \tag{2.13}$$

in which h is the film thickness, a is the relaxation time of the fluid, k is a non-Newtonian factor (described below), μ is the initial viscosity of the fluid (described below), r is the radial coordinate, and v_s is squeeze velocity ($v_s = -\frac{\partial h}{\partial t}$). According to Hashimoto, the initial conditions are as follows:

$$b(t = 0) = 0, f(t = 0) = 0. \tag{2.14}$$

Hashimoto used the following constitutive equation to model the fluid:

$$\mu \frac{\partial v_r}{\partial z} = \tau_{rz} + k\tau_{rz}^3 + a\frac{\partial \tau_{rz}}{\partial t}, \tag{2.15}$$

where μ is the initial viscosity of the fluid, v_r is the radial velocity of the fluid, τ_{rz} is the shear stress of the fluid, k is a nonlinear factor, and a is the relaxation time of the fluid.

Equation 2.15 is a linear combination of the power-law and the non-linear Maxwell fluid models. Letting both k and a equal zero results in the constitutive equation of a Newtonian fluid. The second term on the right hand side accounts for the pseudo-plastic and dilatant non-Newtonian effects (e.g., the power-law model, described below). A value of $k > 0$ corresponds to shear-thinning or pseudo-plastic behavior and $k < 0$ corresponds to shear-thickening or dilatant behavior. The third term on the right hand side accounts for the viscoelastic effects. The first and third terms together make up the Maxwell fluid model; setting $k = 0$ is equivalent to assuming a linear Maxwell fluid model such as that described earlier in this chapter.

A general form for a power-law model can be written as

$$\tau = C\dot{\gamma}^n \tag{2.16}$$

where C and n are material properties of the fluid found experimentally. Values of n greater than 1 indicate dilatant behavior, values less than 1 indicate pseudo-plastic behavior and $n = 1$ corresponds

to Newtonian fluids. The inverse of the power-law fluid model can be written as

$$\dot{\gamma} = \left(\frac{1}{C}\tau\right)^{1/n} \tag{2.17}$$

and substituting $K = 1/C$ and $p = 1/n$ it is rewritten as

$$\dot{\gamma} = K\tau^{p} \tag{2.18}$$

which has a similar form to the second term on the right hand side of Eq. 2.15. Specifying p =constant using only the power-law model would necessarily designate the behavior of the fluid (i.e., pseudo-plastic or dilatant). However, using a constant for the exponent of the non-linear term in Eq. 2.15 does not constrain the fluid to be shear-thinning or shear-thickening because there are other terms present. That is, pseudo-plastic, Newtonian, and dilatant behavior may still be represented by the complete constitutive equation 2.15 with a constant exponent on the second term whereas the the power-law model alone depends on the exponent to prescribe the shear-thinning or shear-thickening behavior. This completes the discussion of the constitutive equation.

Returning to the squeezing flow between parallel plates of a thin film, certain assumptions can be made. The flow is assumed to be axisymmetric with significant components in the radial direction only. It further assumes small variation of physical quantities in the film thickness direction (a thin-film approximation), that the flow is incompressible, and that there is no slip at the circular plate walls. Lastly, the inertia forces are assumed to be constant across the film thickness.

The solutions of the system of equations 2.12 and 2.13 with initial conditions from equation 2.14 were found numerically using the built-in MATLAB function ode45 which is a fourth-order, Runge-Kutta, adaptive solver. Equation 2.9 was evaluated using the built-in MATLAB numerical integration function trapz which uses the trapezoidal method to integrate numerically. The non-Newtonian squeeze-flow model was compared with the measured data from the oscillatory squeeze flow testing.

For both Newtonian and non-Newtonian fluids, the peak measured force was compared with peak calculated force (which was calculated based on the experimental conditions for each

test case) and the results are provided in Chapter 3. Fluid rheological properties were measured for both Newtonian and non-Newtonian fluids and are reported in Appendix A.

CHAPTER 3. SQUEEZE FLOW EXPERIMENTAL METHODS

Due to the inherent difficulty associated with the measurement of *in vivo* contact pressures between human vocal folds under a variety of fluid layer conditions, a model was needed that would permit the study of the potential effects of the liquid layer on voice operation. To develop such a model, the vocal fold vibration needed to be coupled with the effects of the liquid layer. Many existing vocal fold models, both computational and synthetic, presently exist; however, none include liquid layer models.

During phonation, the vocal folds collide repeatedly and the liquid layers on the opposing folds interact. The liquid layers collide and merge, the merged layer is squeezed and stretched and finally ruptures as the vocal folds separate during the opening phase of the glottal cycle. The behavior of the fluid film is considered to be similar to the squeezing flow of a liquid. Therefore, existing equations describing the squeezing flow of a fluid between parallel, axisymmetric disks were evaluated as a suitable liquid layer approximation.

The work described in this chapter details the experimental testing that was performed to validate these equations that was performed. The simultaneous measurements of force and film thickness were taken on a test setup created for this purpose and the results were compared with corresponding calculated values from the existing squeeze-flow equations for both Newtonian fluids and non-Newtonian, Maxwell fluids (see Sec. 2.2 and 2.3). Data collected consisted of measured film force, measured film thickness, fluid temperature, and the acceleration of the fixed and moving plates over time.

3.1 Equipment Description

The setup consisted of a test fixture clamped to the test stand platform of the test stand as shown in Fig. 3.1. Five masonry blocks were stacked on the lower plate of the test stand to reduce structural vibrations.

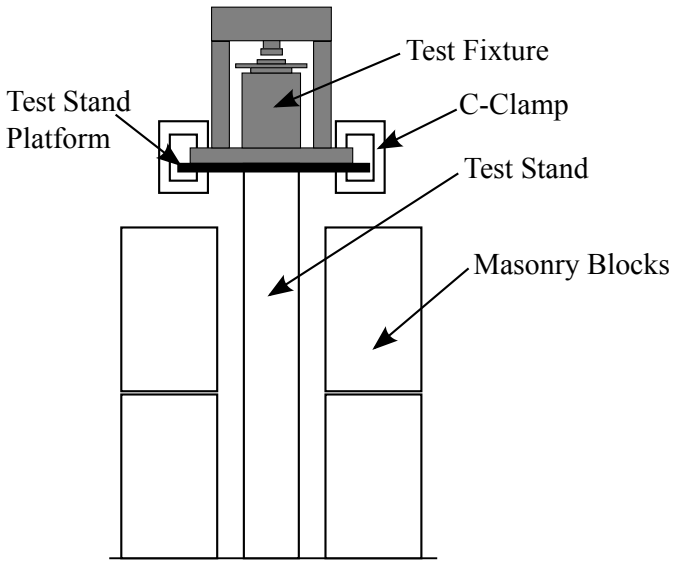

Figure 3.1: Test stand setup for oscillatory squeeze-flow measurements.

A schematic of the test fixture is shown in Fig. 3.2. The fixture had two rigid, parallel plates (one oscillating, one fixed) between which a test fluid could fill the gap for squeeze-flow testing. The instrumentation attached to the fixture enabled the simultaneous measurement of film thickness, total film force, and acceleration.

The fixture consisted of a 30.5x30.5x3.175 cm aluminum base plate, to which vertical steel columns were mounted to support a solid 5x5 cm steel beam. An electrodynamic shaker (Labworks, EET-126) was rigidly mounted to the base plate, centered between the vertical support columns with screws. An aluminum disk was rigidly attached to the moving armature of the shaker. A dynamic force gauge (PCB Electronics, 208C01, uncertainty of < 1% full-scale) was centrally mounted to the underside of the beam and a 2.5 cm diameter aluminum plate was rigidly attached to the underside of the force gauge. Two accelerometers were mounted to the fixture: one to the shaker disk and the other centrally located on top of the beam. A precision LVDT (Honeywell, S5, 0.25% full-scale non-linearity, $\pm 0.5 \mu$m repeatability) with a maximum uncertainty of $\pm 2.5 \mu$m was rigidly mounted to the side of the beam so that the armature would be in contact with the moving disk mounted to the shaker. A thermocouple (Omega, K-type, accuracy $\pm 2.2^{\circ}$C), wrapped in Teflon to electrically isolate the probe, was mounted inside of a hole drilled close to the lower surface of the upper, fixed plate for approximation of the fluid temperature.

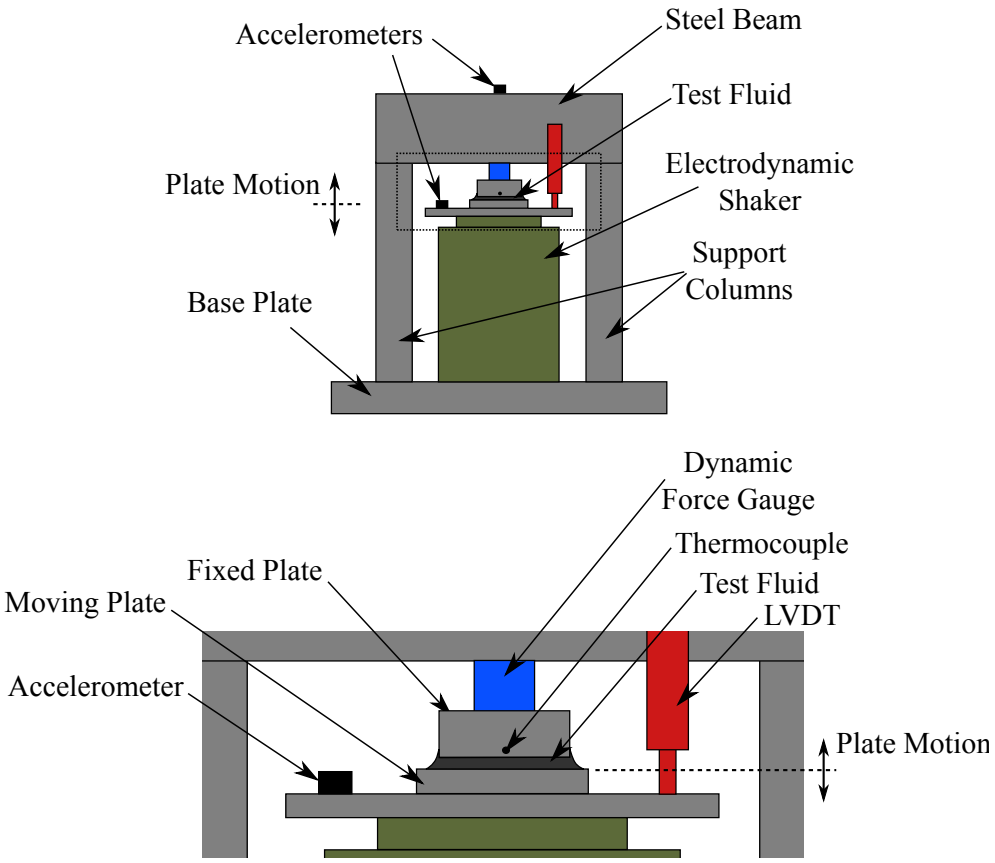

Figure 3.2: Test fixture schematic for oscillatory squeeze-flow testing.

A variety of sensors are available for the measurement of position and force. The test fixture required the measurement of film thickness on the order of 10 to 1000 μm with a spatial resolution of better than 10 μm. The force measurements needed to have an estimated peak maximum force capability of 45 N (tension/compression) and a resolution of better than 1 mN. Both sensors needed to have a temporal resolution of at least 1250 Hz, but ideally above 5000 Hz. Additional requirements included mounting location, consideration of interference from other sensors and fixture parts physically, electrically, and magnetically, sensitivity to vibration, linearity, range, and the effect of liquid on the sensors performance and accuracy.

Several sensors were evaluated for their effectiveness for the given application. Position sensors considered include: laser range finders, ultrasonic transducers, optical methods (such as high-speed imaging), eddy-current sensors, capacitive sensors, and linear variable differential transformers (LVDTs). Sensors considered for the measurement of force include: piezoelectric pressure transducers, strain-gauge type sensors (such as load cells), and piezoelectric dynamic

force gages. The only sensors that adequately met the specified requirements were the precision LVDT for film thickness and the piezoelectric dynamic force gauge for force. Other related studies with similar setups have used the same or very similar sensors [55–58].

A block diagram of the instrumentation setup is shown Fig. 3.3. All analog output and input functions were performed by a LabVIEW application in conjunction with National Instruments DAQ boards. Analog inputs were sampled simultaneously on the 8-channel PXI-4472 at 5 kHz. Measurements were acquired from the LVDT, force gauge, accelerometers, thermocouple, and the amplified voltage input from the power amplifier to the shaker. An analog output from the PXI-6221 was DC-coupled to the voltage input of the power amplifier to enable use of a DC offset to control the mean plate gap distance. A demodulator (Honeywell DLD-CH) was used for the excitation input voltage to and the conditioning of the output signal from the LVDT (Honeywell S5).

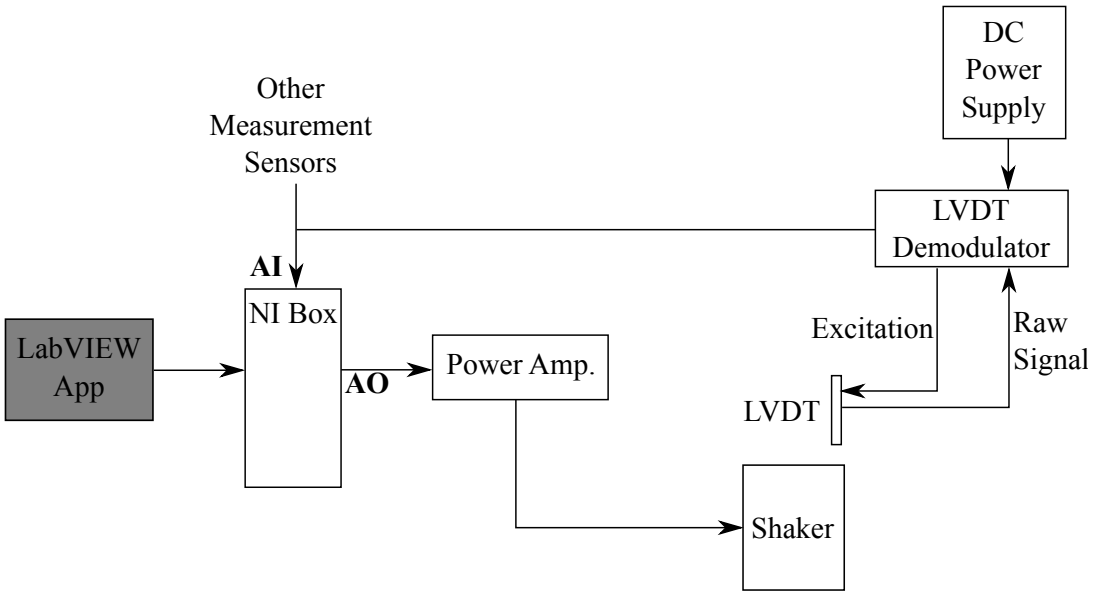

Figure 3.3: Instrument setup schematic.

The LabVIEW application allowed the user to enter the parameters to control the output signal and sensor calibration parameters. The generated output sine wave was calculated based on the user's specification of frequency, amplitude, and DC offset.

3.2 Testing Procedure

Two kinds of testing were performed: oscillatory squeeze flow, and colliding/separating flow. Under oscillatory conditions, the moving plate attached to the electrodynamic shaker was displaced sinusoidally and normal to the plate's surface. Under colliding/separating conditions, a step input was used to displace the moving plate. The step input was setup to transition between two different film thickness. The fluid was squeezed under colliding conditions and stretched under separating conditions.

For both oscillatory and colliding/separating flow conditions, each testing period consisted of calibration, application of fluid, mean gap initialization, and the repeated input of testing condition parameters and subsequent recording of measurements to a file.

The LVDT zero gap distance was calibrated prior to taking measurements on the test fixture. This was done by setting the voltage of the DC offset and increasing the gain of the power-amplifier just beyond where the plates were observed to have contact.

The DC offset was set so that the gap was large enough for fluid to be placed at the center of the lower plate. After depositing the fluid, the gap was gradually decreased by modifying the DC offset until the desired mean film thickness was achieved. Sufficient fluid was used so that the fluid completely wetted the entire gap and beyond the perimeter of the smaller diameter upper plate, and without bubbles, as shown schematically in Fig. 3.4.

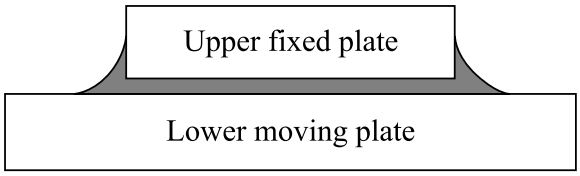

Figure 3.4: Fluid entirely fills the gap between plates and beyond perimeter of smaller, upper plate. There are no bubbles in the fluid. Typical film thicknesses were 30-1000 μm (see Appendix B for tables of test conditions including mean film thicknesses).

3.2.1 Oscillatory Squeeze Flow

The frequency and amplitude of the displacement waveform were specified in the LabVIEW application to drive the shaker. Voltage amplitude and DC offset were adjusted until the

desired mean film thickness and amplitude of oscillation reported by the LVDT measurement were achieved. It typically took some time (10-30 sec) for the mean film thickness and amplitude of oscillation to reach steady-state. After steady-state readings were achieved, one second (5000 samples) of data was recorded to a file. Successive trials were then performed by varying the voltage amplitude and DC offset parameters.

After the completion of a set of trials, the upper fixed plate was removed from the force gauge, the remaining fluid was removed, the surfaces were cleaned with isopropyl alcohol to remove any residue, the clean upper plate was reattached, and the zero gap was recalibrated prior to the next set of trials.

3.2.2 Colliding/Separating Flow

Colliding and separating flow measurements were taken by setting two DC voltages corresponding to two film thicknesses and switching between them while recording data (i.e., a square wave input). One voltage corresponded to a small gap or thin film, and the other to a large gap or thick film. All other testing procedures were identical to those described above.

3.3 Analysis

3.3.1 Oscillatory Squeeze Flow

Data previously written to files by LabVIEW were imported into MATLAB for data analysis. The first ten periods (first through tenth zero-crossing positive, defined in the next paragraph) of the measured data was extracted for analysis. In the low frequency cases where there were less than ten periods recorded, the entire data set was used. A corresponding analytical solution for force in terms of film thickness (Eq. 2.6) was calculated from this subset of measured data. Measurements were taken on both the measured and calculated data and compared for correlation. Measurements included frequency of oscillation, mean film thickness, peak film thickness, peak force, and phase lag between film thickness and force.

The frequency of the film thickness waveform was calculated by averaging the time difference between adjacent zero-crossing positives (defined below) and taking the inverse of the average

period for the subset of recorded data. The time at which the instantaneous value of a waveform transitions from a negative to a positive value is called a zero-crossing positive. Zero-crossing positives could also be described as the roots of the waveform which have positive slopes. The direction of the slope (e.g., positive or negative) is not so important as the fact that the same point in the cycle is located. Hence, two adjacent zero-crossing positives mark the start of two adjacent cycles. The zero-crossing positives were found by normalizing the waveform, setting thresholds of ±15% of the peak amplitude, extracting the portion of data between the thresholds, and with a generally positive slope, fitting a line to the data and finding the root of the fitted line. An example of this method is illustrated in Fig. 3.5.

A phase lag or time delay, here denoted as δ, exists between the film thickness waveform and the force waveform. This phase lag was measured by taking the difference between the zero-crossing positive of the film thickness and zero-crossing positive of the force immediately following. An example of this is shown in Fig. 3.6.

The ratio of peak calculated force to peak measured force, F_c/F, was also used to compare different data sets. Figure 3.7 shows a typical example of these results.

As described in Sec. 2.2, the squeeze-film force was to be calculated from film thickness and its first and second temporal derivatives. The numerical differentiation of the raw noisy film thickness waveform resulted in an extremely noisy force calculation. Therefore, the measured film thickness was fit with a sine curve. The amplitude, mean value, frequency, and phase of the sine curve fit were used to estimate the derivatives of the film thickness. In practice, the film thickness waveforms were fit very well by a sine curve.

The viscosities of the Newtonian fluids used in this study were relatively sensitive to temperature changes (see Sec. 2.1). To improve the accuracy of the force calculations, the viscosity was estimated using the measured temperature and a curve-fit of measured viscosity vs. temperature data (see Appendix A).

The constant radius of the upper fixed plate (0.0127 m) and the velocity profile correction factor α=1.54 were used in the force calculation.

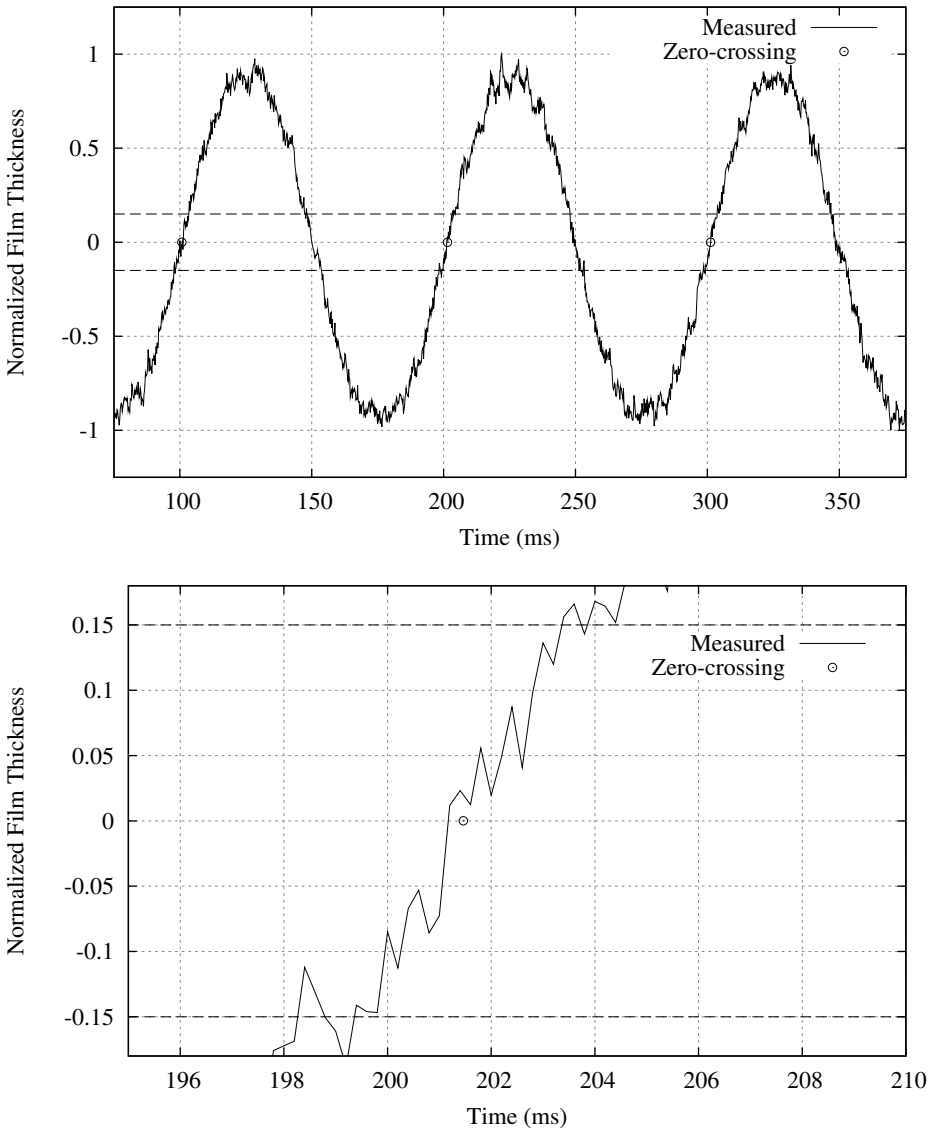

Figure 3.5: Typical zero-crossing positive of noisy measured data. The top plot shows typical data subset of four periods. The bottom plot shows a magnified section of the second zero-crossing positive from the top plot.

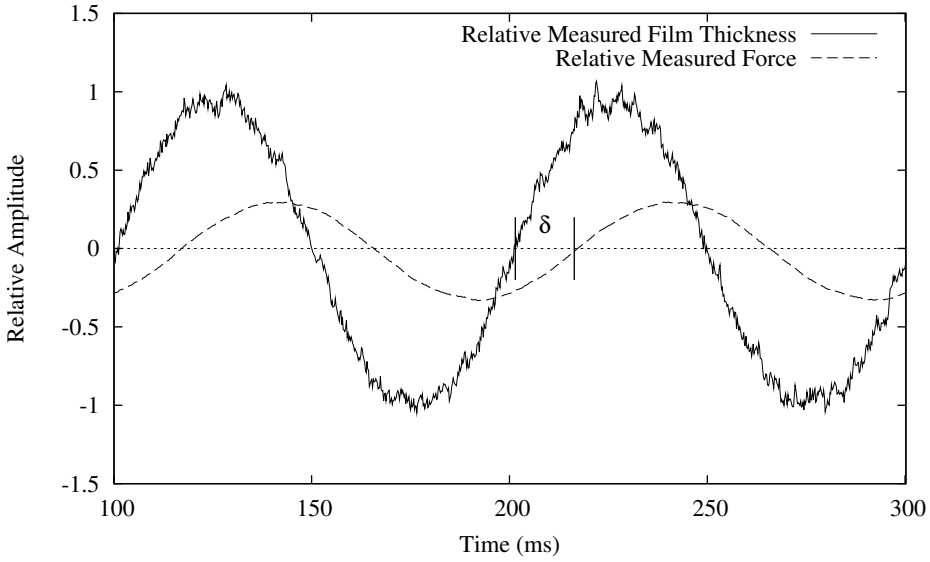

Figure 3.6: Typical phase lag measurement.

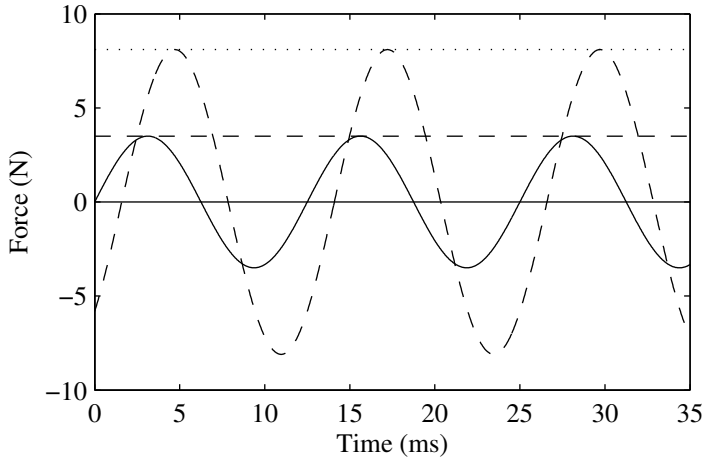

Figure 3.7: Typical peak calculated force, F_c, and peak measured force, F measurements. The solid waveform represents the measured force data, the dashed waveform represents the calculated force from the sine-wave curve-fit of film thickness, the dashed straight line is the peak measured force, and the dotted straight line is the peak calculated force.

3.3.2 Colliding/Separating Flow

Figure 3.8 shows an example of the typical measurements taken of colliding followed by separating flow. The data in the plot shown are normalized by dividing by the maximum absolute value of each trace so that the data vary from -1 to 1 and centered vertically at $y = 0$ to align the signals in time. Measurements include voltage input to the electrodynamic shaker, film thickness, h, velocity of the moving plate ($\dot{h}$, rate of change of film thickness), and measured force. The voltage input to the electrodynamic shaker transitions as a square-wave from low to high at t = 967.2 sec. During the first portion of the cycle (prior to $t = 967.2$ sec) the plates are approaching and the flow is squeezing. After the transition at $t = 967.2$ sec, the plates are separating. Peak force magnitudes, F_{pk}, are seen at the time of transition. Positive force magnitudes are compressive forces, negative magnitudes are tensile forces. Film thickness transitions logarithmically between states.

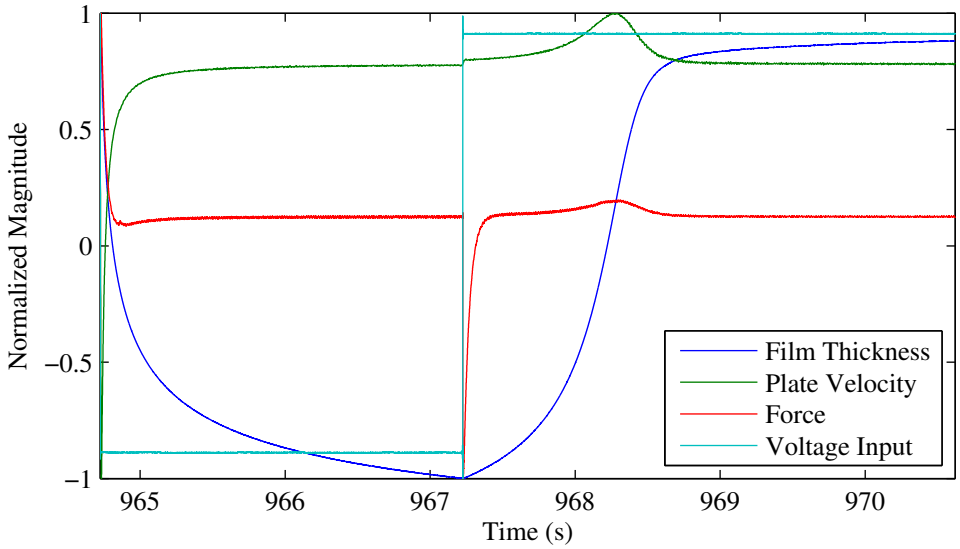

Figure 3.8: Typical collision/separation cycle. All measurements are normalized by dividing by the maximum absolute value of each trace (so that they vary from -1 to 1) and centered at $y = 0$. Measurements shown are voltage input to the electrodynamic shaker, film thickness, h, velocity of the moving plate ($\dot{h}$, rate of change of film thickness), and measured force vs. time.

Figures 3.9 and 3.10 show only the colliding and separating portions, respectively, of a cycle. The initial velocity of the moving plate, v_0, (which is equal to the rate of change of the

film thickness $\dot{h}$) is measured by taking the numerical derivative of measured film thickness and fitting a line through the first several data points. Peak velocity, v_{pk}, is found for each portion of a cycle by taking the absolute magnitude of velocity during the colliding and separating portions of each cycle. Thus, a peak velocity is found for collision and a separate peak velocity for separation. The time is measured between transition and peak velocity and is reported as t_{velpk} in the tables of data given in Tables B.7 through B.12. Initial film thickness, h_0, is taken to be the film thickness immediately preceding transition.

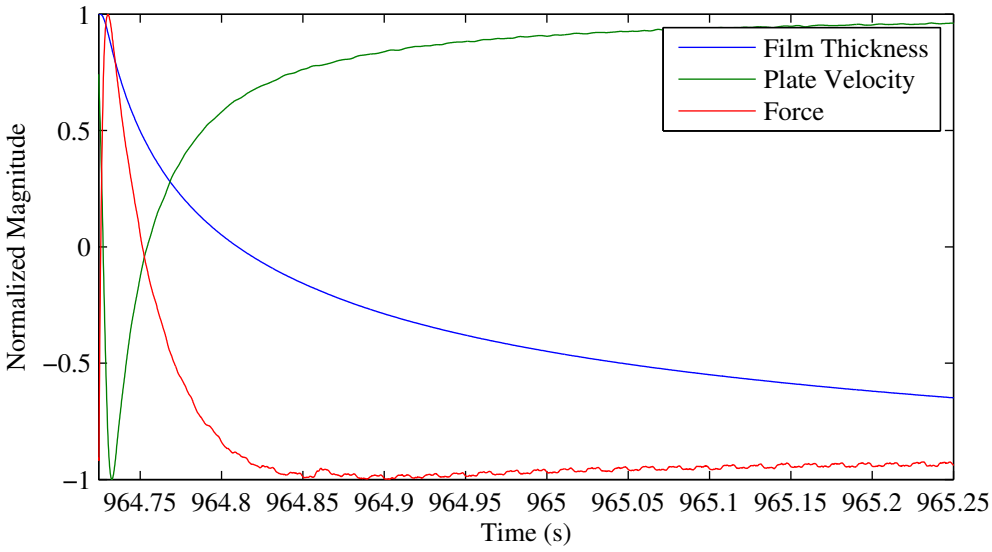

Figure 3.9: Typical normalized collision measurements vs. time. Measurements were normalized by dividing by maximum, absolute value for each corresponding trace. Measurements include plate velocity ($\dot{h}$, rate of change of film thickness), film thickness, and force.

3.4 Results and Discussion

3.4.1 Newtonian Fluids - Oscillatory Squeeze Flow

Three Newtonian fluids were tested: (1) 90% wt glycerin-distilled water mixture, (2) olive oil, and (3) distilled water. Figure 3.11 shows the ratios of the peak calculated force to the peak measured force, F_c/F, for the oil data with error bars indicating uncertainty which is further discussed in Appendix G. Figure 3.11a shows F_c/F for all of the acquired oil data. The horizontal

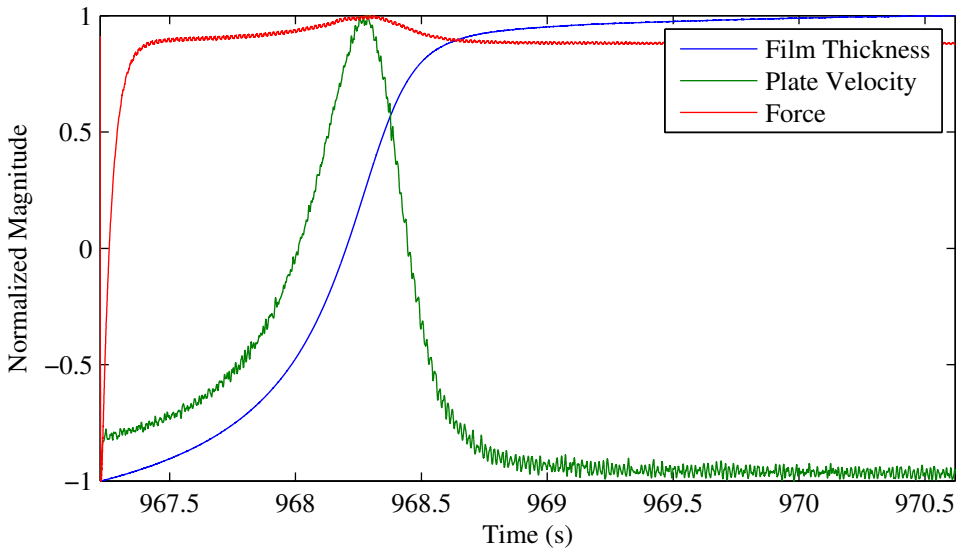

Figure 3.10: Typical normalized separation measurements vs. time. Measurements were normalized by dividing by maximum, absolute value for each corresponding trace. Measurements include plate velocity ($\dot{h}$, rate of change of film thickness), film thickness, and force.

dashed line denotes the expected value of the data points (i.e., where the calculated and measured forces are equal). As can be seen in the figure, a departure from the expected results occurs for films with thickness less than about 100 μm and increases in magnitude as the film thickness decreases.

Figure 3.11b shows only the oil data where the film thickness was less than 150 μm. The calculated force over-predicts the measured force by a factor of up to 20 for very thin films (around 40 μm). When the film thickness is greater than about 80 μm, the calculated force is still over-predicted, but by less than a factor of 3. While this results in much better agreement between the measured and calculated force, the error is still too large to draw strong conclusions regarding the force that may be exerted by the liquid layer on a human vocal fold.

Figure 3.11c shows only the oil data points for mean film thicknesses greater than 80 μm. The calculated force is up to 3 times larger than the measured force for thinner films, but the two forces become closer as the film thickness increases. For film thickness of 500 μm, the peak calculated force is ±25% of the peak measured force.

Figure 3.12 shows F_c/F for all of the glycerin data. There were eleven cases where the mean film thickness was less than 100 μm. For these thin-film cases, the range of frequencies

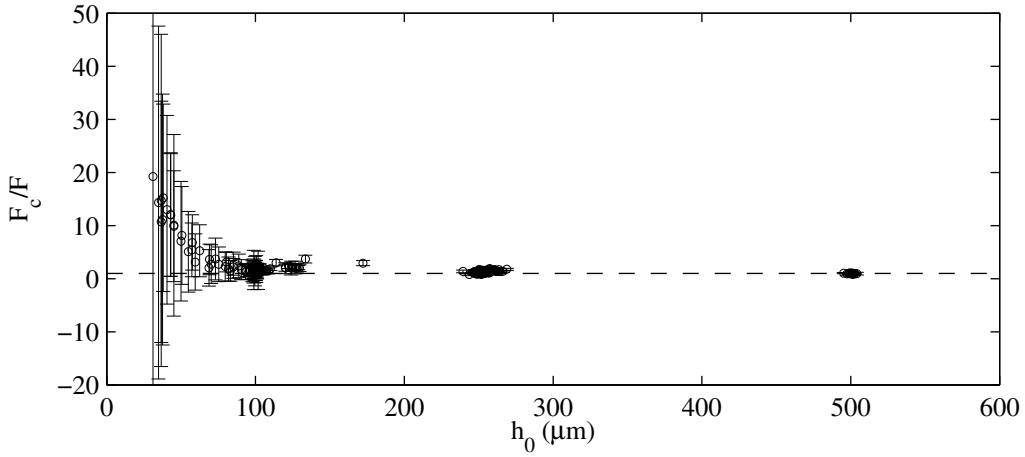

(a)

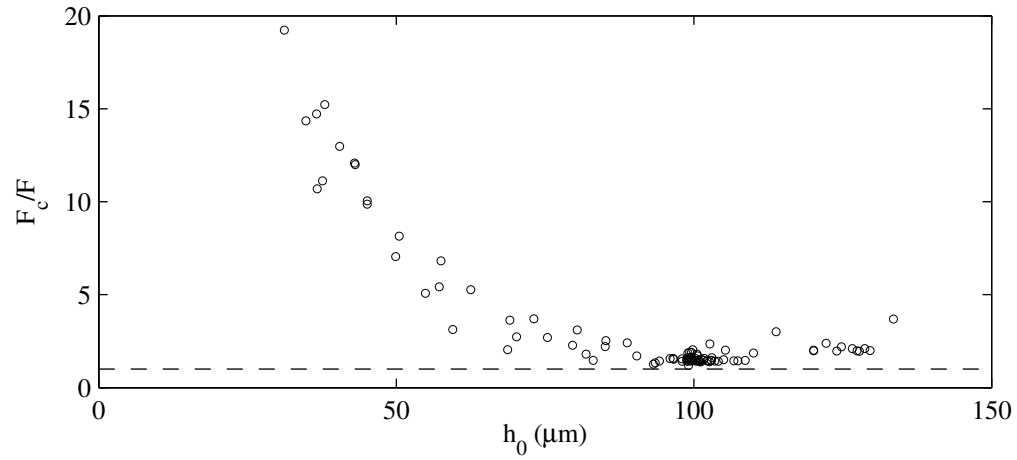

(b)

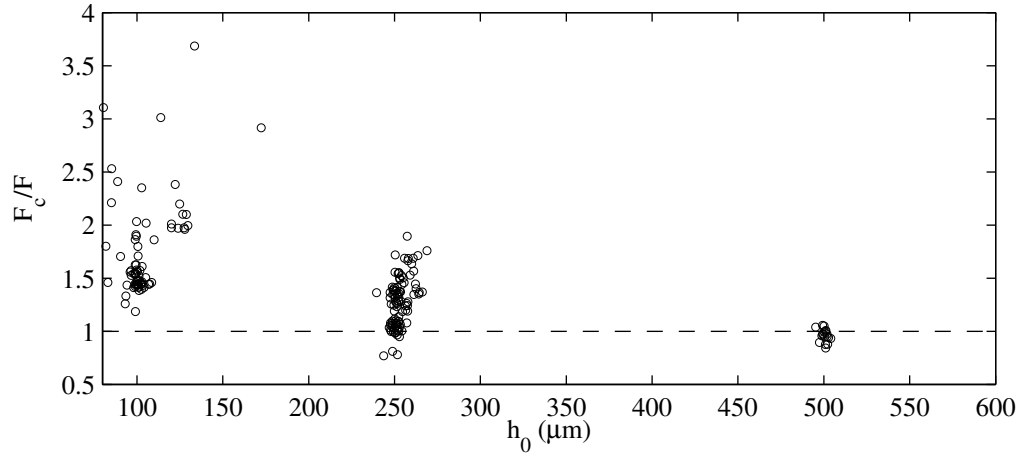

(c)

Figure 3.11: (a) All oil data, (b) All oil data up to 150 μm mean film thickness, (c) All oil data above 80 μm mean film thickness. Error bars indicate uncertainty (see Appendix G).

Table 3.1: Two olive oil data sets compared in order to illustrate the repeatability of the measurements.

Data Set #	Freq. (Hz)	h_0 (μm)	h_{pk} (μm)	F_{pk} (N)	Temp (°C)	μ (Pa·s)	SSE
46	70.0	96.6	5.4	13.041	25.3	0.061	6.53E-11
47	70.0	96.0	5.5	13.380	25.1	0.061	1.80E-10

varied from 20 to 100 Hz, the amplitude fractions (displacement amplitude divided by mean film thickness) varied between 1 and 2%. For the thicker films (> 100 μm), the frequencies varied from 20 to 120 Hz and the amplitude fractions varied between 0.7% and 8.4%. A much better agreement is seen between the calculated and measured force data for glycerin than for oil. Even for thinner films (mean film thickness near 80 μm), the calculated force is less than 2.5 times that of the measured force. As with the oil case, the over-prediction of force decreases with increasing film thickness.

Figure 3.13 shows F_c/F for all of the water data. Again, a similar trend of decreasing F_c/F is seen as film thickness increases. However, in this case, the calculated force is always larger than the measured force. It should be noted that the range of mean film thickness over which the data was collected varies somewhat between the different fluids. This is because the force required to achieve the desired displacement amplitude is substantially higher for higher viscosity fluids. The range of fluid viscosities of the test fluids varied by two orders of magnitude.

The variance in F_c/F in Figs. 3.11-3.13 is primarily a result of changes in F_c. However, under different testing conditions (e.g., changes in film thickness, amplitude of displacement, frequency, and fluid), the peak measured force, F, also changes. The repeatability of the testing was observed to be good. As an example, the two cases shown in Table 3.1 can be compared (see Appendix B). As shown, there is less than 2% change in the mean film thickness, h_0, displacement amplitude, h_{pk}, and oscillatory frequency. There is a correspondingly small change in peak measured force of 2.6%. This example illustrates the typical results for all cases. Therefore, the variance in F_c/F were not attributed to discrepancies in repeatability of the testing.

Figure 3.14 shows the phase delay in degrees between the measured and calculated force data for oil. It can be seen that the majority of the data falls near a curve that initially decreases, reaches a minimum near a frequency of 20-30 Hz, and then generally increases up to 130 Hz.

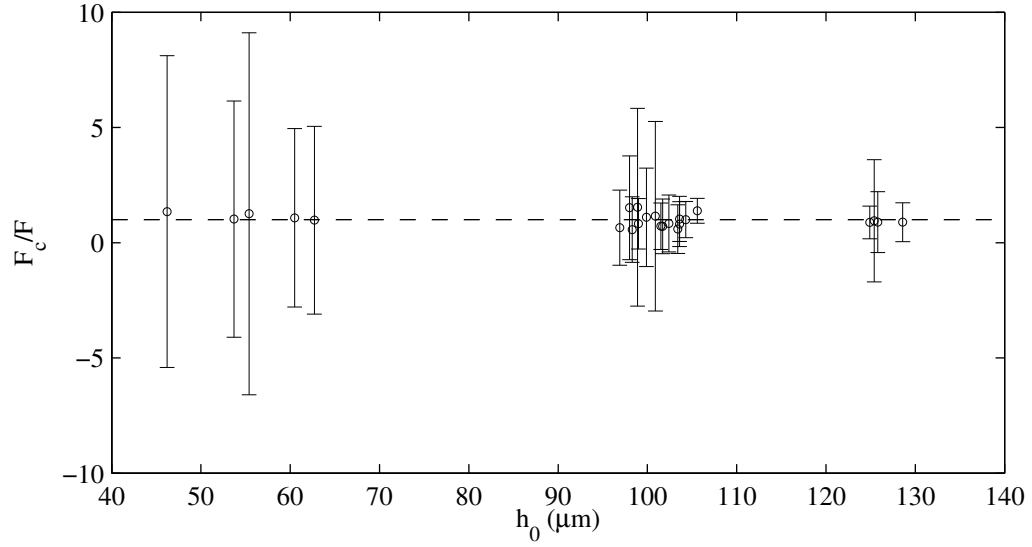

(a)

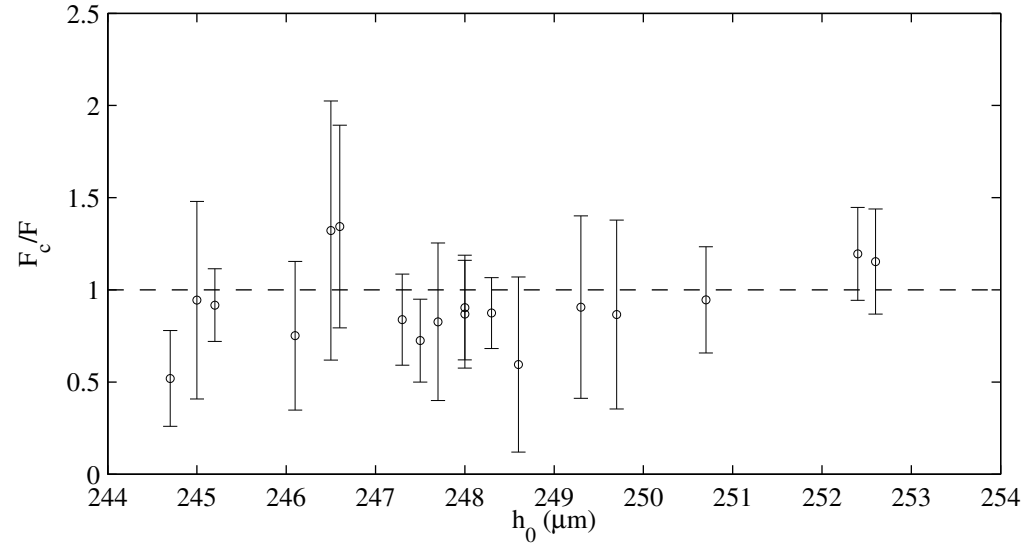

(b)

Figure 3.12: Plot of ratio of peak shows calculated force to peak measured force, F_c/F, for glycerin data. All data obtained is shows, but is separated into two plots above based on mean film thickness. Plot (a) shows data for film thicknesses between 40 and 140 μm and (b) shows data for film thicknesses between 244 and 254 μm.

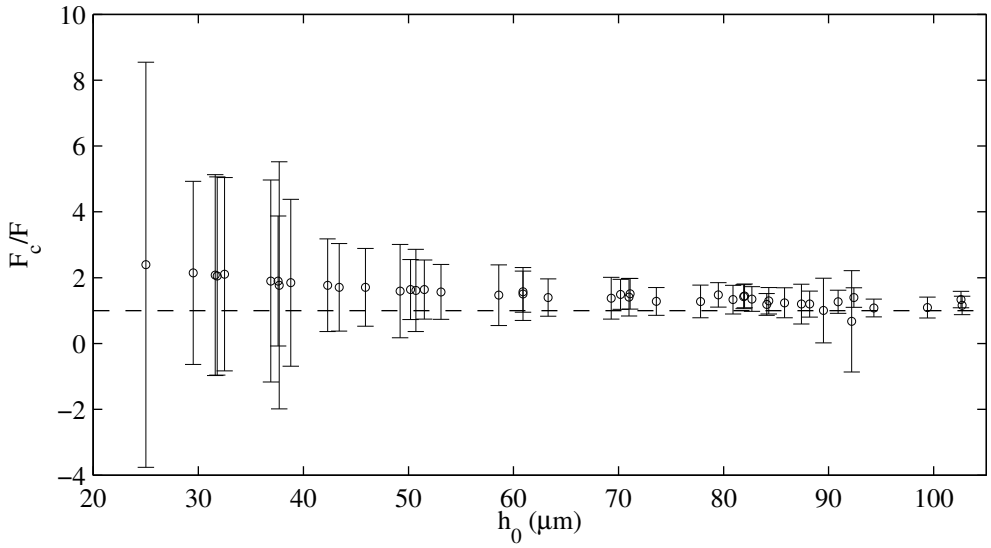

Figure 3.13: Plot of ratio of peak calculated force to peak measured force, F_c/F, for water data.

Many of the data points do tend to cluster near the upper border of the higher frequency data which indicates a trend of increasing phase delay with increasing frequency above 40 Hz. However, the variance in the data increases at the higher frequencies (above 60 Hz), making it difficult to find a significant trend in the data.

The source of the large variance in the phase difference between the measured and calculated force waveforms is unclear. The variance increases as frequency increases, which suggests an amplification of a temporal uncertainty. It was thought to be the result of a time delay or slow response time of one or more sensors (e.g., LVDT and/or force gauge), the signal amplifiers, or data acquisition devices. However, documentation from the manufacturers for each product verifies that the time delays from the devices are at least an order of magnitude smaller than what would cause the observed variance.

Another suspected source of the variance that was considered was error associated with the method used to locate zero-crossing positives described previously. However, based on simulated data tests with normally distributed noise of up to 20% signal amplitude (are least 4 times that of the measured data), the uncertainty in phase was less than 0.2% of the period.

One possible source of the error is the angular deflection of the moving plate attached to the armature of the electrodynamic shaker. The peak measured forces were greater than 8 Newtons in the majority of cases which exhibit the large variance and the frequency of oscillation was

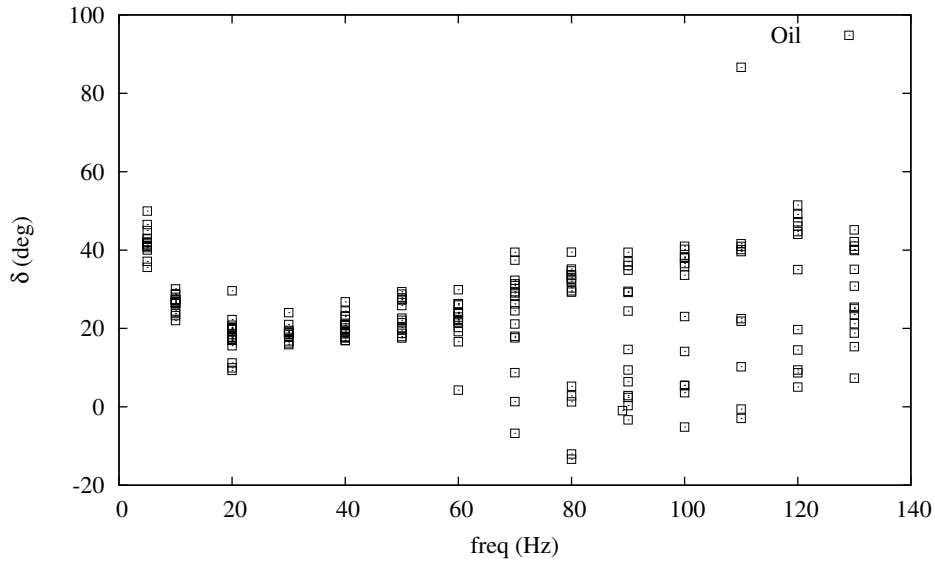

Figure 3.14: Phase difference between peak measured force and peak calculated force for oil data.

above 60 Hz. Larger peak forces on the moving plate would cause larger angular deflection of the moving plate. If the armature is rocking during oscillation, there could be a change in the phase difference between the measure film thickness and the measured force. Since the calculated force is determined from the measured film thickness data, the phase difference between the calculated force (based on measured film thickness) and measured film thickness would be different than the phase difference between the measured force and the measured film thickness. This could give rise to erratic phase differences between the measured and calculated force.

Figure 3.15 shows the phase difference, in degrees, for the glycerin data. With the exception of a few data points, the phase difference is always positive and appears to increase at an increasing rate as oscillatory frequency increases. In general, the magnitude of the phase difference is larger for glycerin over all frequencies than for oil. The largest phase difference is close to 150 degrees whereas the maximum for oil is less than 60 degrees (except in one case at 110 Hz).

Figure 3.16 shows the phase difference in degrees for the water data. Again the phase difference increases with increasing frequency. At 20 Hz, the phase difference clusters around 20 degrees so that a slight curvature in the trend is noticeable similar to the oil case. The phase difference appears to increase (perhaps linearly) beyond 40 Hz.

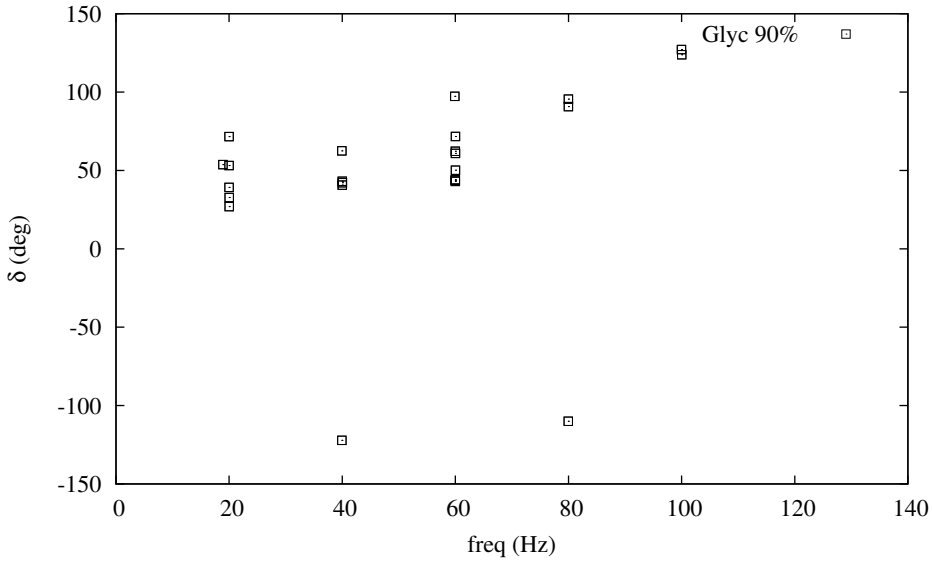

Figure 3.15: Phase difference between measured force and calculated force for 90%-wt glycerin data. Negative values indicate a phase lead as opposed to a lag between measured and calculated force.

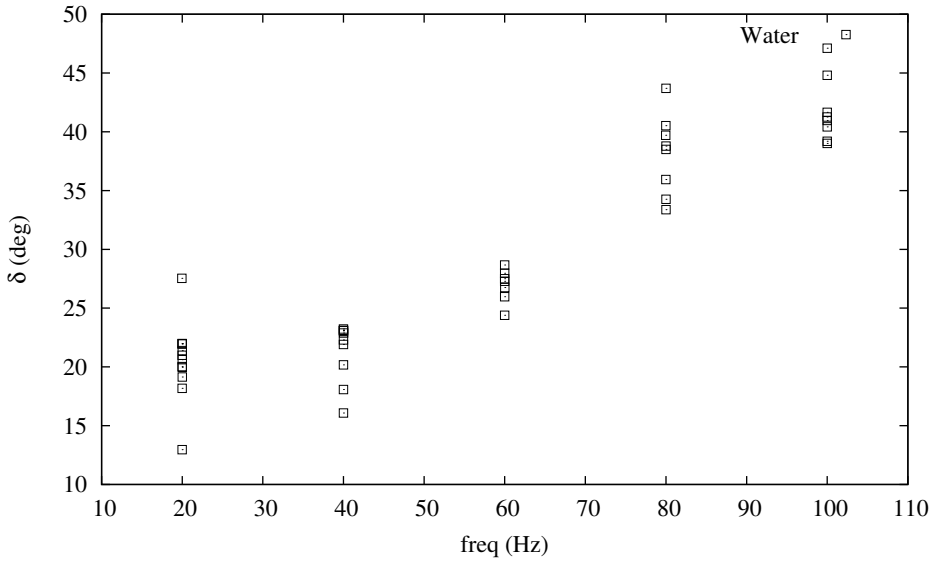

Figure 3.16: Phase difference between measured force and calculated force for water data.

One might consider fitting a curve to the phase data shown in Figs. 3.14-3.16, however, the variance in the data make the correlation poor at higher frequencies so that the meaningfulness of an empirical relation is diminished.

3.4.2 Newtonian Fluids - Colliding/Separating Flow

Figure 3.17 shows F_c/F, the ratio of peak calculated force to peak measured force, for the Newtonian fluids (water, glycerin, and oil) in colliding and separating conditions. The calculated peak force for oil and glycerin is within ±20% of the measured value for the vast majority of the data. However, the measured peak force for water spreads from half to double the measured value. For all fluids, the calculated peak force is within ±50%, even for very thin films (< 100μm).

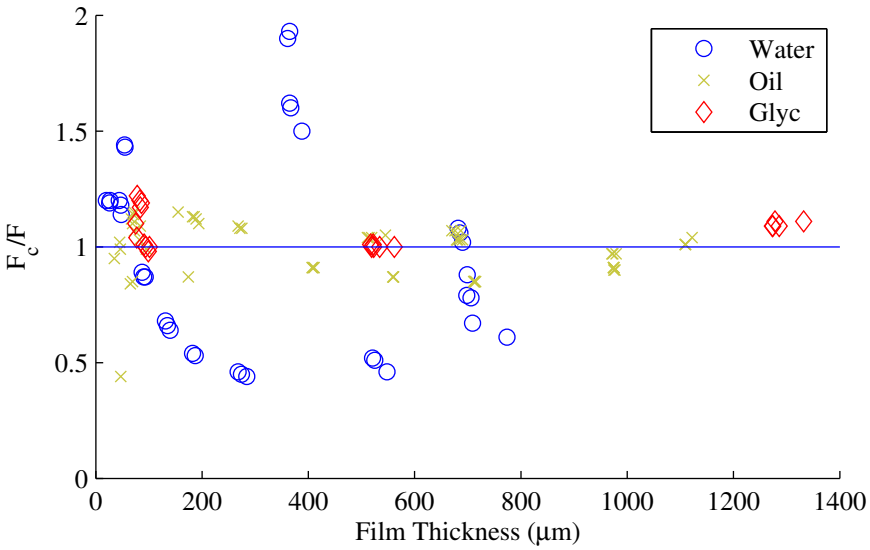

Figure 3.17: F_c/F ratio for Newtonian collision/separation peak force measurements.

In order to further summarize the peak measured force data and identify meaningful trends, the data were non-dimensionalized. The non-dimensional groups were based on the parameters in

the Newtonian squeeze-flow equation (see Eq. 2.6) and are as follows:

$$\tilde{R} = R_0/h_0 \tag{3.1}$$

$$Re = \frac{\rho v_0 h_0}{\mu} \tag{3.2}$$

$$\tilde{a} = \frac{h_0 a_0}{v_0^2} \tag{3.3}$$

$$\tilde{F} = \frac{F_{pk}}{\rho v_0^2 h_0^2} \tag{3.4}$$

where R_0 is the radius of the smaller upper plate, h_0 is the initial film thickness, Re is the Reynolds number, ρ is fluid density, v_0 is the initial velocity of the plates (i.e., just after transition), μ is fluid viscosity, $\tilde{a}$ is the non-dimensional acceleration, a_0 is the initial acceleration of the plates (i.e., just after transition), $\tilde{F}$ is the non-dimensional peak force, and F_{pk} is the peak measured force.

Figure 3.18 is a plot of the natural logarithm of the non-dimensional force vs. the natural logarithm of the Reynolds number. The geometry, namely R_0, was the same for all tests and the magnitude of acceleration was so small that its effects were expected to be negligible. Therefore, only non-dimensional force and Reynolds number trends are shown here.

The data for each fluid is shown with a linear fit on the log-log plot. The coefficients of the fit-lines are given in Table 3.2. As can be seen, there is good agreement between the linear fit and the dimensionless data for each fluid. It is interesting to note that each fluid is grouped on a different fit line. There is a small difference between the data taken for oil and glycerin and a larger difference for water. This may indicate that a family of non-dimensional curves exists which describes the colliding/separating flow regime.

Table 3.2: Non-dimensional Newtonian fluid line fit coefficients ($f(x) = Ax + B$ where x is $\log(Re)$).

	A	B
Water	2.425	8.369
Oil	-2.128	4.741
Glyc	-2.069	4.548

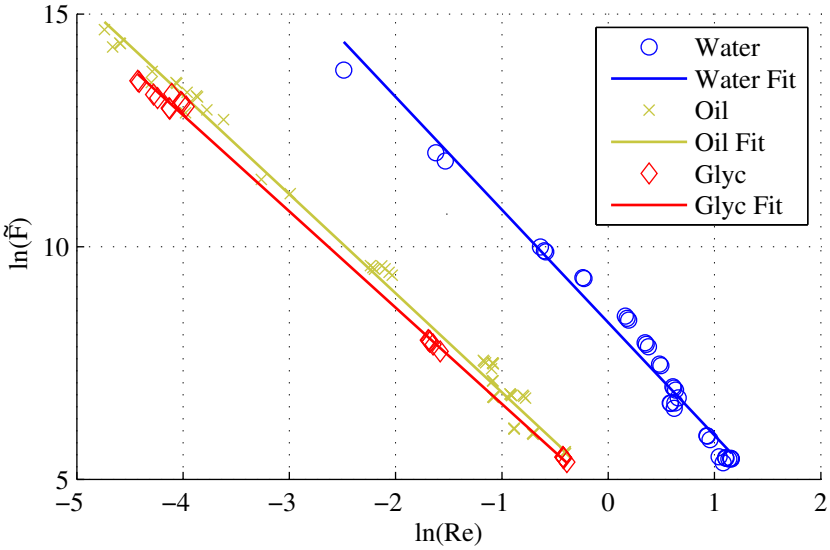

Figure 3.18: Plot of natural logarithm of non-dimensionalized peak force vs. natural logarithm of Reynolds number for colliding/separating flow. A linear fit line identifies the set of cases for each fluid. The fit lines for the oil and glycerin data are almost identical while the water data is much different.

3.4.3 Non-Newtonian - Oscillatory Squeeze Flow

Two non-Newtonian fluids were tested in oscillating conditions. Each was a different mixture, by weight, of xanthan gum and distilled water. The mixtures by weight percent were 0.5%, 1.0%, and 1.5% xanthan gum for XG1, XG2, and XG3 respectively. The elastic modulus and the loss modulus were measured before and after testing. Results of the rheological testing are summarized in AppendixA.

A comparison was made between the experimental data and the calculated results of the squeeze flow equation (Eq. 2.9) for Maxwell fluids described in Ch. 2. Since the parameters k and a in the constitutive Eq. 2.15 do not relate directly to standard rheological properties such as G' and G'', it is necessary to either: (1) optimize the analytical solution to match the measured data by varying the rheological parameters in the constitutive equation and compare the parameters, or (2) attempt a best fit between the constitutive equation and a variety of rheological measurements. Both methods were used and the results are described below.

An optimization was performed between the results of Eq. 2.9 and the measured squeeze flow data. The relaxation time, a, (see Eq. 2.15) was found by minimizing the error between the

calculated and measured film thickness waveforms. Since a is a fluid property, it is expected to be constant for all test cases for a given Maxwell fluid. Figures 3.19, 3.20, and 3.21 show the results of the optimization. Four plots are shown in each figure comparing a with the frequency of oscillation, the amplitude of oscillation, the mean film thickness, and the amplitude fraction. No correlation between a and any of the latter three parameters is seen. There is a slight "inverted parabolic" correlation between frequency and a for XG2 and XG3. No other significant correlations could be found.

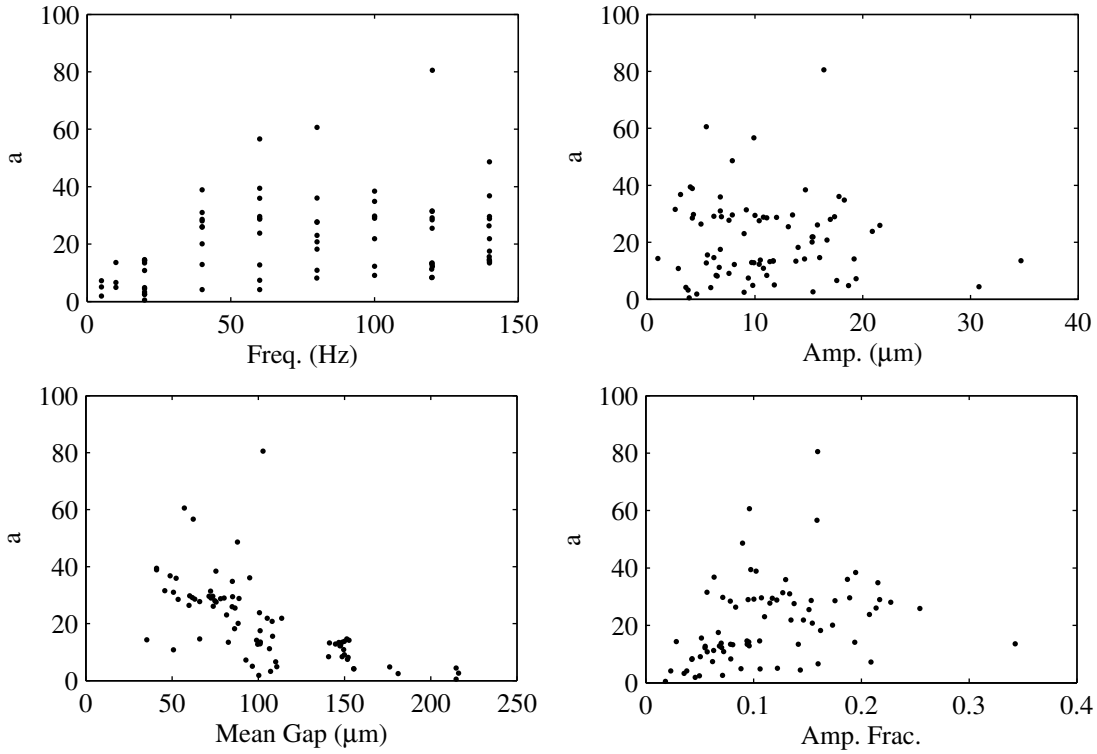

Figure 3.19: Comparison of a with other parameters for XG1 fluid.

While the slight correlation between frequency and a may seem interesting initially, the excitement of this finding is moderated by the fact that a in Eq. 2.15 is a constant according to the derivation and should be independent of frequency. This correlation may be incidental, or it may indicate the heritage of the discrepancy in the present mathematical model. Regardless of the source of the discrepancy, it must be concluded that this Maxwell model, as it is, does not

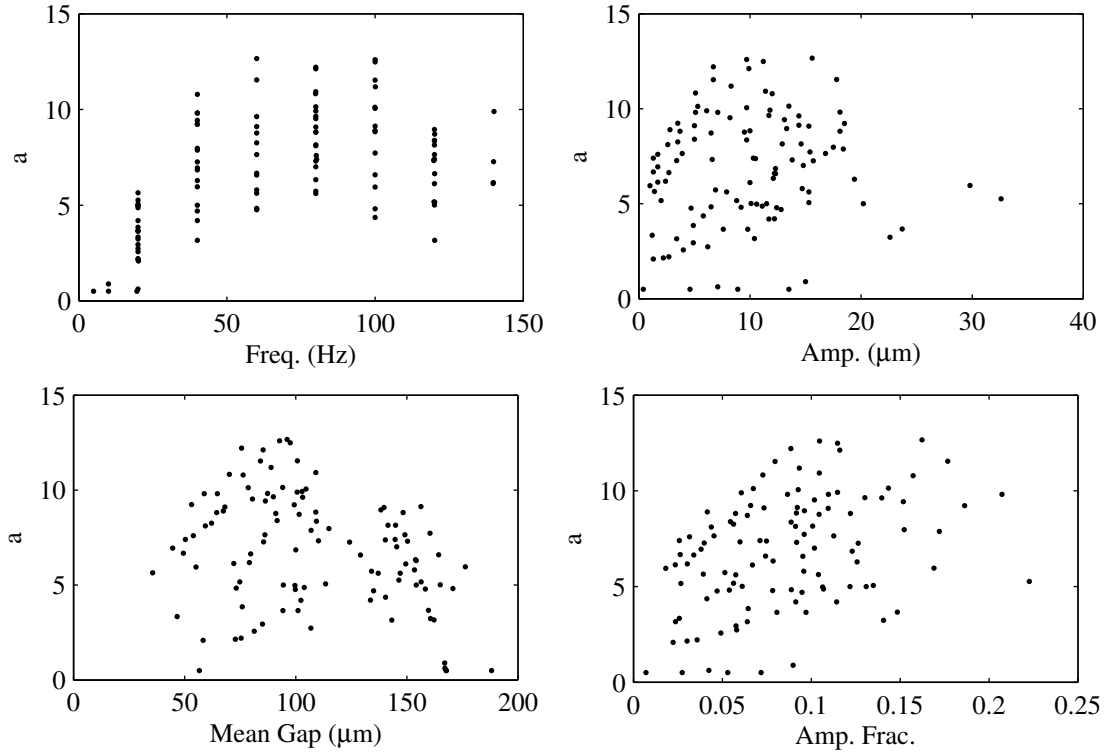

Figure 3.20: Comparison of *a* with other parameters for XG2 fluid.

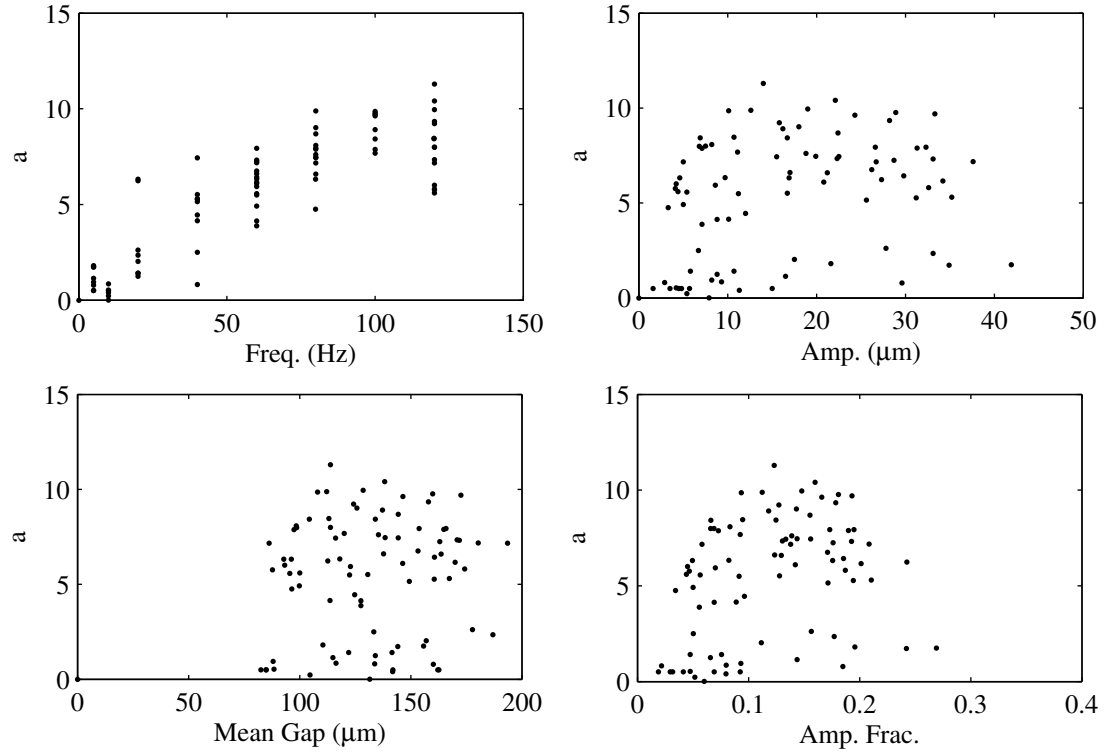

Figure 3.21: Comparison of *a* with other parameters for XG3 fluid.

accurately predict the film force of the xanthan gum mixtures under the oscillatory conditions to which it was subjected during this testing.

3.5 Conclusions

3.5.1 Newtonian

In summary, there are a few noteworthy aspects of the Newtonian data. First, the calculated force almost always overestimates the measured force, but the ratio of calculated to measured force, F_c/F, decreases generally as film thickness increases. Second, the phase difference between the measured force and the calculated force waveforms decreases to a minimum around 20-30 Hz and then increases above around 40 Hz. Third, the phase difference tends to increase with increasing viscosity (e.g., water, oil, glycerin).

Although intriguing, the phase difference does not have a direct effect on the forces that may be developed on the vocal folds during phonation. As such, the results are reported, but not discussed any further.

The discrepancy between the measured and calculated force is quite significant. The difference could potentially be attributed to the following sources: (1) the derivation of the equation is invalid, (2) the implementation of the analytical solution has an error, (3) there was error in the experimental measurements, and/or (4) one or more of the assumptions made in the derivation were violated in the experimental conditions. It was assumed that Eq. 2.5 was valid and correct according to its assumptions. The derivation was published in a reputable, peer-reviewed journal many years ago and no later papers were found that overturned the original derivation. Therefore, no indication could be found that suggests the derivation is in error for the applicable assumptions. Furthermore, at the time of its publication, Eq. 2.5 was found to be in good agreement with then-existing experimental data published separately by others [59]. Those experimental measurements consisted of the central pressure of a fluid film in oscillatory squeezing conditions over a range of frequencies, amplitudes, and film thicknesses that were comparable to the research described in this thesis. The experimental data also confirmed the accuracy of using $\alpha = 1.54$ for oscillatory squeezing flow conditions.

To verify that the equation was implemented correctly, a short MATLAB code is included in Appendix E detailing the implementation and the output from the code are given below. Figure 3.22 shows the calculated film force which was created from the code using Eq. 2.6. As shown

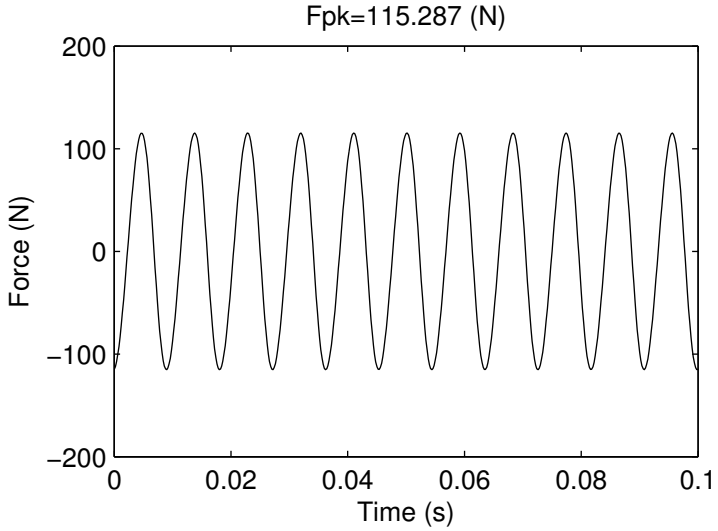

Figure 3.22: Plot produced by film force code showing calculated force.

in Fig. 3.22, the peak calculated force is over 115 N which is greater than ten times the peak force measured for this case (see Table B.2, data set #63). Several cases calculated and measured cases were compared with similar results. Therefore, it was concluded that the implementation of the equation matches the derivation described in Ch. 2.2.

Several tests were performed to verify that the sensors were calibrated, functioning properly, and that minimal interference was occurring. All testing indicated that the sensors were indeed calibrated and functioning properly during experimental testing. A summary of the tests performed is given in Appendix D.

A discussion of the validity of the assumptions inherent within Eq. 2.6 for the experimental testing follows. The equation is valid for laminar flow of an incompressible, Newtonian fluid confined between flat, parallel, circular plates of a fixed wetted diameter with motions normal to the plate surface. The three fluids tested (e.g., 90% wt glycerin-distilled water mixture, olive oil, and distilled water) are all incompressible, Newtonian fluids. As described earlier in this chapter, the geometry of the setup consisted of parallel circular plates in which the fluid completely filled

the gap between the circular disks. The upper was slightly smaller than the lower plate so that some fluid filled a small region beyond edge of the upper plate and maintained full wetting of the upper plate diameter. The edge effects were assumed to be negligible in comparison to the forces developed in the fluid within the gap. The upper and lower plates were measured to have a flatness of less than 13μm (< 0.0005 in) which is between 33% and 16% of the mean film thickness as it varies from 40μm to 80μm respectively. Some of the error may be attributed to the flatness of the plates.

Further assumptions include an approximate velocity profile of the fluid in the fluid gap which is approximated by the mean velocity profile, and the limitation that $V_f > -V_p/2$, where V_f is the mean velocity of the fluid in the radial direction and V_p is the relative velocity of one of the plates in the radial direction. For the research described in this thesis, $V_p = 0$ always, since the plate motion was only in the direction normal to the plate surface which implies the reduced assumption $V_f > 0$. This means that the equation is valid during the portion of the cycle in which the plates are approaching (i.e., squeezing flows), but is not generally valid for cases where the plates are moving away from each other and the film thickness is increasing. This assumption is of course violated during about half of each oscillating cycle. This indicates that the peak calculated force during separating flow may not be accurate.

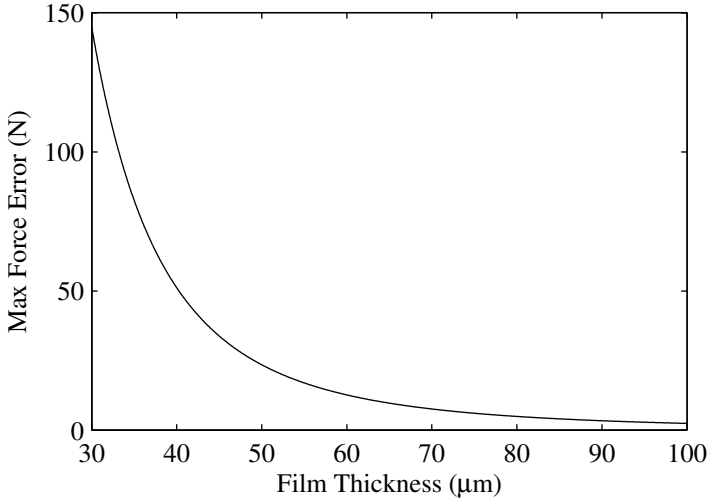

Figure 3.23: Propagated uncertainty in calculated force from uncertainty in temperature and film thickness (see Appendix G for further explanation).

The majority of the error in the calculation of force from Eq. 2.6 can be attributed to the uncertainty inherent in the measurement of fluid temperature and film thickness. As described in Appendix A, the viscosity of the fluid is estimated from the measured temperature. The thermocouple used to measure temperature had an uncertainty of ±2.2°C. Furthermore, the film thickness sensor (a precision LVDT), had an maximum non-linearity of ±0.25% full-scale which corresponds to an uncertainty of ±2.5μm. The combined uncertainty from temperature and film thickness increases as film thickness decreases. A plot of the propagated uncertainty is shown in Figure 3.23. Derivation of the uncertainty can be found in Appendix G.

Another observation regarding error in peak calculated force is that the values are always larger than the measured force. This would suggest a bias of some sort in addition to random uncertainty error. As discussed previously in this chapter, angular displacement or rocking of the moving plate could explain this bias. The fact that the calculated force is always larger than the measured force suggests that the measured amplitude of displacement is larger than the true displacement amplitude (neglecting other sources of error). Furthermore, the physical location of the LVDT is about twice the radius of the smaller plate away from the center of the fluid film, thus, angular displacements of the moving plate could cause larger error in the measured film thickness than if the LVDT was located closer to the film's center. If the moving plate was rocking during oscillation, the displacement amplitude would always be larger than the true value. An angular displacement of just ±0.0023 degrees would cause an increase of 1 μm in the displacement amplitude. The nature of this error always results in an increased displacement amplitude. Therefore, it is concluded that this is a likely cause of the bias. Furthermore, within measurement uncertainty, Eq. 2.6 was found to agree with the measured data.

In order to evaluate the potential that the fluid layer has to influence voice operation, the Newtonian squeeze-flow equation (Eq. 2.6) was used to estimate the timescale on which a thin film of fluid can deform while being squeezed. It is reasonable to conclude that if the time it takes to squeeze a thin-film of fluid by an appreciable amount (63%) is on the same order as the time period that the vocal folds are in contact (e.g., colliding or separating), then the fluid may have the potential to influence voice operation. If on the other hand, the timescale is much longer or shorter than the duration of time the vocal folds are in contact (e.g., colliding or separating), then it is less likely the fluid will have the potential to influence voice operation.

During vocal fold vibration, if one-quarter of a vibratory cycle is the portion in which the fluid film is being squeezed, then the timescales for average male and female human voice (130-240 Hz) correspond to 1.0 to 2.0 ms. Figure 3.24 shows the timescales of squeezing flow for a range of fluid viscosities and initial film thicknesses. The timescales were measured by solving Eq. 2.8 with an initial squeezing velocity of 0.5 m/s, and measuring the time to reduce by 63.2% of the original film thickness. This is analogous to the definition of a time-constant for a function that follows a logarithmically decaying curve.

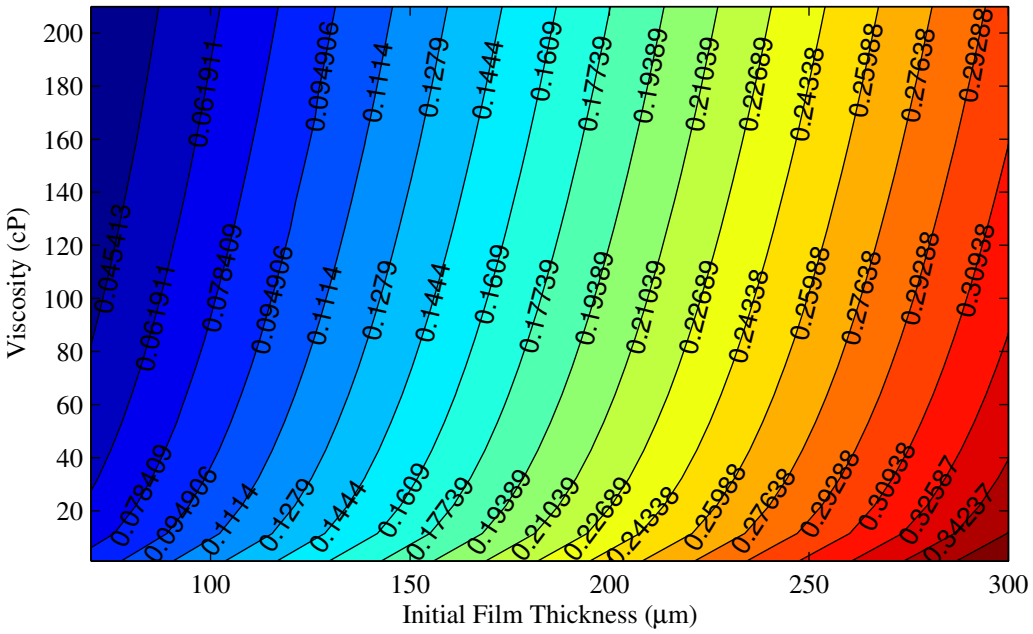

Figure 3.24: Contour plot showing timescales of squeezing flow in ms for ranges of viscosity and initial film thickness.

The calculated timescales for the range of viscosities and initial film thicknesses are within an order of magnitude of the timescales for average human voice. This suggests that the fluid film covering the human vocal folds may deform on a timescale similar to that of the contact times of normal human phonation. If this is the case, the fluid may have the potential to affect vocal fold operation by cushioning the impact of opposing vocal folds during collision by squeezing and viscously dissipating the impact or deforming during separation and locally amplifying tissue

stresses during separation. This suggests that further investigation of the fluid layer is worthwhile in that it may contribute to voice operation or the development of disorders.

The experimental measurements presented in this chapter regarding Newtonian squeeze-flow were used to validate the Newtonian squeeze-flow equation for its use as a liquid layer model to be incorporated into a numerical model of vocal fold vibration. The next chapter describes the implementation of the liquid layer model on a lumped parameter model.

3.5.2 Non-Newtonian

Figure 3.25 shows a comparison between the shear stress vs. shear rate curve obtained through measurement and that obtained from a best-fit of the constitutive equation (Eq. 2.15) during a series of peak hold tests. A peak hold test is performed by holding the shear stress constant and recording the shear rate during a period of time. Peak hold testing can be used to measure the time-dependence of viscosity of a fluid. As can be seen in the figure, the correlation between the constitutive equation and the measured data is poor. The general trend across shear stress is approximated, but change in shear rate over time is not captured.

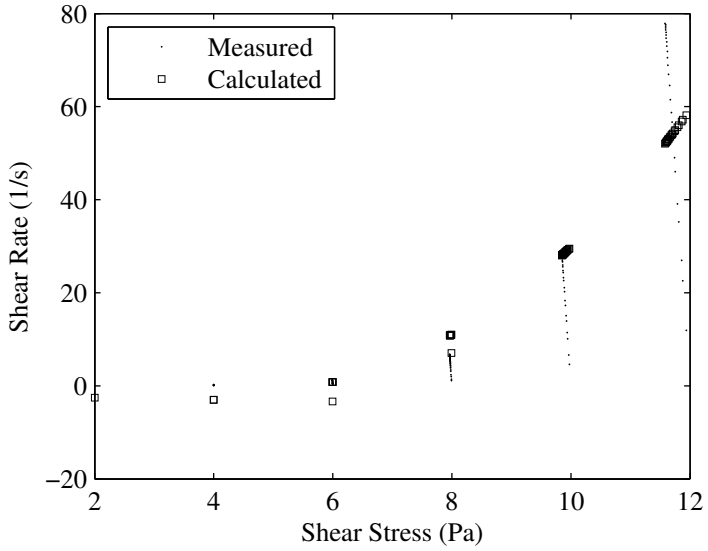

Figure 3.25: Comparison of best-fit constitutive equation with measured rheology data during peak hold testing at different shear stresses.

Figure 3.26 shows a comparison between the measured data and a best-fit of Eq. 2.15 for a test in which shear stress was increased linearly from 0.1 Pa to 12.0 Pa over 60 seconds. The error in the calculated shear rate is over 100% for shear stresses above 8 Pa and up to 12 times the measured value at shear stresses below 8 Pa. These two examples clearly demonstrate that the constitutive equation used for non-Newtonian squeeze-flow does not accurately model the xanthan gum mixture used in testing. The xanthan gum mixture was specifically chosen after comparing the measured rheological data of a variety of non-Newtonian fluid mixtures (e.g., tragacanth gum, guar gum, locust bean gum, xanthan gum, and others) with published data regarding the rheological properties of human mucus. Xanthan gum was the only fluid that correlated with the published data provided in [44]. Therefore, the notion of using another non-Newtonian fluid whose rheological data correlates better with the equation would not meet the original purpose of this research project.

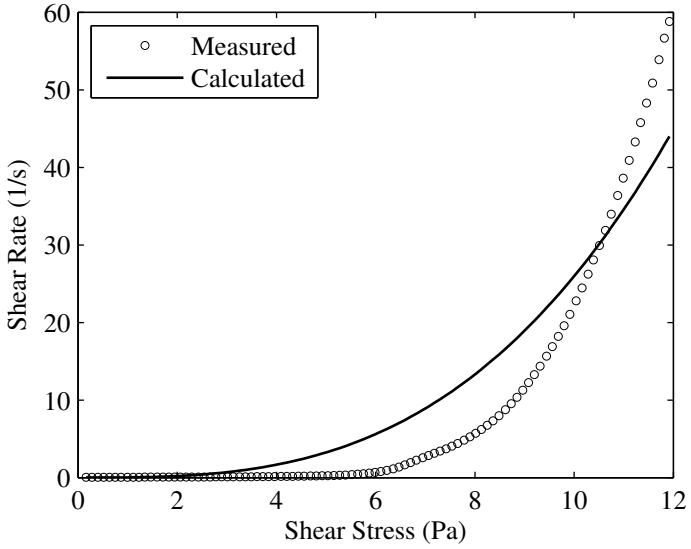

Figure 3.26: Comparison of best-fit constitutive equation with measured rheology data during linear ramp of shear stress.

Another approach might be to adjust the constitutive equation so that it matches the fluid properties of the specified fluid. This is not an simple task as the math is far from trivial and developing such an equation would likely be a sizable project in and of itself. A search was made in the literature to find a suitable model. There are very few analytical equations describing squeeze flow of non-Newtonian fluids between parallel plates altogether. Of those found none could be expected

to provide better results than those presented herein. Therefore, the accurate analytical modeling of parallel plate squeeze flow of the xanthan gum mixtures used for the research described in this thesis is dependent upon a suitable constitutive equation.

Another method of analysis could be to develop a finite element model using the measured rheological data for the fluid model in the computational simulation. Fluid models used in finite element simulations also depend on constitutive models. However, the constitutive models used for finite element simulations can be more elaborate since their solutions are found numerically. To this end, the measurements taken during this research were summarized in Appendix B.

CHAPTER 4. LUMPED PARAMETER MODEL

4.1 Introduction

The Newtonian squeeze-flow Eq. 2.8, which was experimentally validated in the previous chapter, was incorporated into an existing lumped parameter model, often referred to as the two-mass model, in order to explore the influence of a liquid layer on vocal fold vibration. The two-mass model of vocal fold vibration was created in 1972 by Ishizaka and Flanagan [46] and has since been used extensively in the voice community. Many papers have been published which report results of small modifications or additions to the original two-mass model [60–63]. It is understood, however, that the two-mass model does not have the high-order precision afforded by far more complex models such as continuum models. Nevertheless, it does serve to approximate the fundamental self-oscillatory dynamics of voice and as such is used herein as a preliminary indication of the potential effects of a fluid layer on vocal dynamics.

Figure 4.1 shows a diagram of the two-mass model. The model is assumed to be symmetric about the mid-plane. Having two masses provides a mechanism whereby the superior and inferior tissues of the vocal folds can displace out of phase one with another. This has been acknowledged in voice research as an essential element in vocal fold dynamics. It is primarily this feature which enables the vocal folds to self-oscillate.

The two masses are attached to the lateral wall of the larynx via a spring and damper. Shearing stresses within the vocal fold tissues are modeled by a spring connecting the two masses. Collision is modeled by a spring which becomes active when one of the masses passes through the mid-plane. This spring represents the effect of the elastic deformation of vocal fold tissues during collision. The air pressure from lungs to mouth is modeled by an equivalent electric circuit.

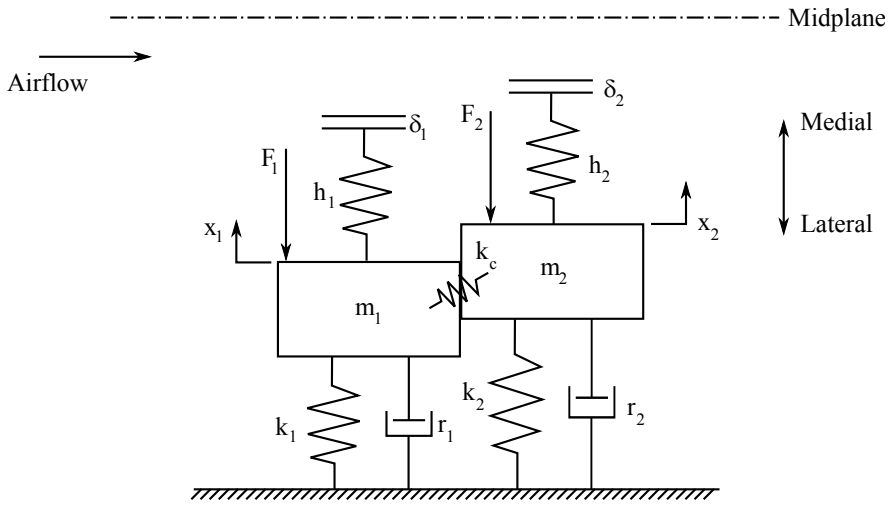

Figure 4.1: Two-mass model with the addition of fluid films of thicknesses δ_1 and δ_2.

4.2 Implementation

Equation 2.8 was incorporated into the original two-mass model by adding fluid films of thicknesses δ_1 and δ_2 on the medial end of springs h_1 and h_2. Stretching and rupture effects of the films were neglected.

The original equations of motion for the masses are:

$$F_1 = m_1 \frac{d^2x_1}{dt^2} + r_1 \frac{dx_1}{dt} + s_1 x_1 + k_c (x_1 - x_2) \tag{4.1}$$

$$F_2 = m_2 \frac{d^2x_2}{dt^2} + r_2 \frac{dx_2}{dt} + s_2 x_2 + k_c (x_2 - x_1) \tag{4.2}$$

where F_i (i = 1, 2, denoting masses 1 and 2, respectively) are the aerodynamic forces (air pressure through glottis calculated from Bernoulli) due to glottal airflow, m_i are masses representing vocal fold tissue, r_i are damping coefficients, s_i are functions representing tissue deformation-related stiffness (the sum of h_i and k_i, discussed below), and k_c is the spring constant accounting for shearing stresses of the vocal fold tissue between the masses.

The tissue deformation terms s_i are:

$$s_i(x_i) = k_i(x_i + \eta_{ki} x_i^3) + h_i \left\{ \left(x_i + \frac{A_{g0i}}{2l_g} \right) + \eta_{hi} \left(x_i + \frac{A_{g0i}}{2l_g} \right)^3 \right\} \text{ for } x_i \le -\frac{A_{g0i}}{2l_g}, \tag{4.3}$$

where k_i and η_{ki} are the linear and non-linear spring constants accounting for the restoring force due to vocal fold tension, h_i and η_{hi} are the linear and non-linear spring constants accounting for tissue deformation, A_{g0i} denote initial (resting) glottal areas, l_g is the glottis length, and $\left(x_i + A_{g0i}/(2l_g)\right)$ represents the displacement from equilibrium used to calculate the value of the tissue deformation. This displacement term was modified to include the fluid layer by adding its thickness:

$$\left(x_i + \frac{A_{g0i}}{2l_g} + \delta_i\right), \tag{4.4}$$

where δ_i is the current film thickness for the ith mass, obtained as follows.

During the closed phase of the glottal cycle and while the tissue deformation spring was in compression, the deformation of the fluid layer was estimated using Eq. 2.8. It was approximated as a quasi-one-dimensional fluid film, bounded by a plane of symmetry on the medial side and on the lateral side to the medial end of the tissue deformation spring, s_i. Thus, the medial plane of the film in the two-mass model is a plane of symmetry corresponding to the mid-plane $(y = h/2)$ of the film in Fig. **??**. The surfaces of the two-mass model are rectangular whereas the squeeze flow equation was derived for axisymmetric geometry. The assumption is that the contact area of the vocal fold tissues are likely to be somewhat elliptical which is reasonably approximated by an axisymmetric geometry. The film area was equal to the exposed surface area of the masses. The medial end of the spring was assumed to exert a uniform force on the moving (lateral) boundary of the fluid film, equal to the force in the spring.

Each film's thickness was calculated at each time step by (1) calculating the force in the spring, (2) applying the spring force as a quasi-steady, uniform force to the film surface, and (3) updating the film thickness and its derivatives. The spring force was calculated (as usual) based on the relative displacement of the spring endpoints from the previous time step. The force in the spring was applied uniformly to the lateral (moving) film surface and was assumed to be constant during the entire time step. The resulting change in film thickness and film surface velocity (h and its temporal derivative) were calculated by integrating Eq. 2.8 numerically. The changes in film thickness and surface velocity were added to the existing values to obtain new thickness and velocity. The presence of the film allowed the medial end of the tissue deformation spring to expand as the fluid was squeezed, reducing the compressive force in the spring. Physically, this

represents a relaxation of the compressive stress in the vocal fold tissue which is interpreted as a dissipation of potential energy stored in the tissue during collision.

The resulting glottal area, flow rate, and mouth pressure vs. time data were compared for three different cases: 1) no fluid layer, 2) thin fluid layer (10 μm), 3) thick fluid layer (100 μm). The fluid layer was assumed to have the same properties as distilled water. The spectra of the mouth pressure waveform data were also compared.

4.3 Results

The results of applying the Newtonian fluid model during collision of the two-mass model are shown in Fig. 4.2. These suggest that the effect of the fluid layer on the dynamics of the vocal folds may not be insignificant. The fundamental frequency, f_0, decreased with increasing film thickness. The calculated f_0 were 167.5 Hz, 166.1 Hz, and 158.3 Hz for the original, 10 μm, and 100 μm cases, respectively, representing decreases in f_0 of 0.8% for the 10 μm case and 5.5% for the 100 μm case. In addition, the glottal flow rate waveform was increasingly different for increasing film thickness. The peak glottal flow rate was reduced from 0.655 m^3/s for the original model to 0.642 m^3/s and 0.582 m^3/s with the application of the fluid model for the 10 μm and 100 μm films, respectively. This corresponds to a reduction in flow rate of 2.1% and 11.2% for the 10 μm and 100 μm cases, respectively.

Another noteworthy feature of Fig. 4.2 is that the maximum glottal area is proportionally smaller for the thin and thick film cases than the original model.

The Fourier transform of the mouth pressure waveform was taken for the different film thicknesses; the envelopes of the resulting amplitude spectra are shown in Fig. 4.3. There are increasingly noticeable differences between the spectra for increasing film thickness. The formants are similar but the relative magnitudes differ which suggests that the fluid layer may also influence sound quality of speech.

4.4 Conclusions

The results show that the frequency spectrum of the voice may be affected by the fluid layer thickness. Further investigation using a higher-order computational physical model is necessary

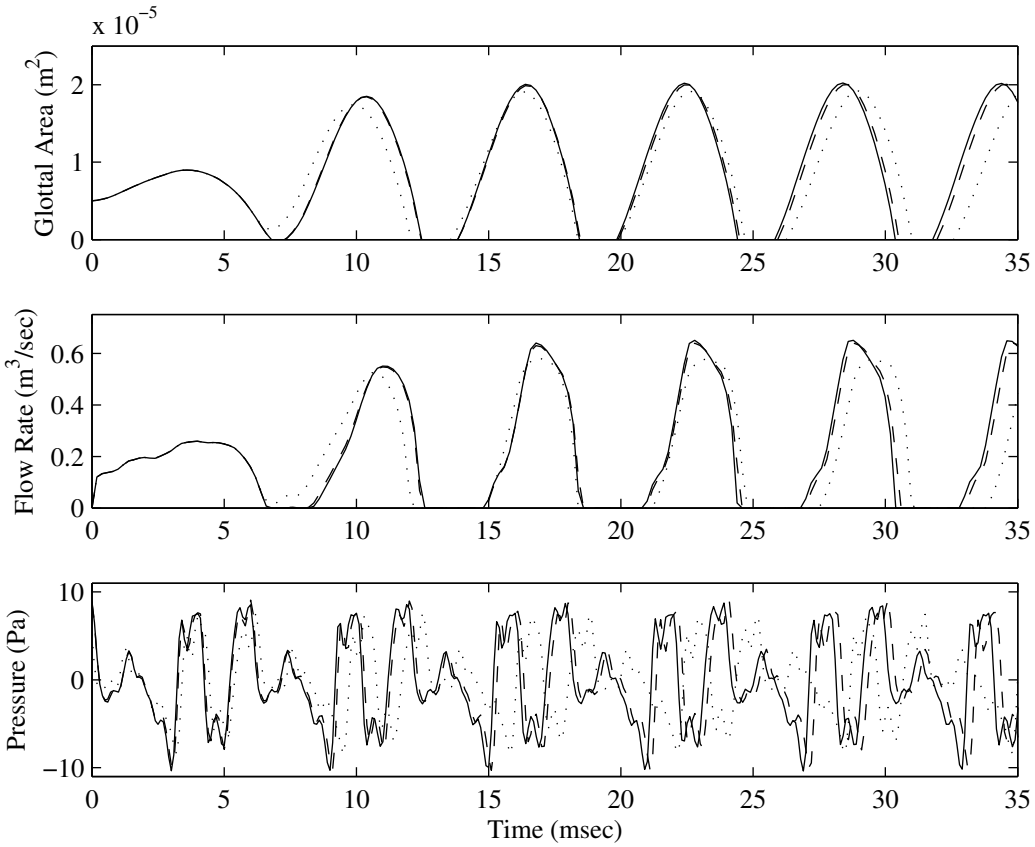

Figure 4.2: Effect of Newtonian fluid layer model ($\rho = 999\ kg/m^3$, $\mu = 0.0001\ Pa \cdot s$) on two-mass model response: (—) no film, (- -) 10 μm film, (···) 100 μm film.

to clarify how the liquid layer affects the frequency spectrum. Nevertheless, on this preliminary model, which incorporates a liquid layer, fundamental frequency was observed to decrease by 0.8% and 5.5% for the 10 μm and 100 μm film cases, respectively, as compared to the no-film case. Peak glottal flow rate was observed to decrease by 2.1% and 11.2% for the 10 μm and 100 μm film cases, respectively. Thus, these preliminary findings indicate that changing the fluid layer thickness may influence voice quality. Additional investigation is required to further substantiate this effect.

The model described in this chapter deals only with the effects of squeezing a Newtonian fluid. The results show that if the film thickness is very small (e.g., the 10 μm case) the changes in the model dynamics are correspondingly small and thus may be neglected. Therefore, it is likely that the thin Newtonian "sol" layer, which has a thickness reported around 6 μm, has little

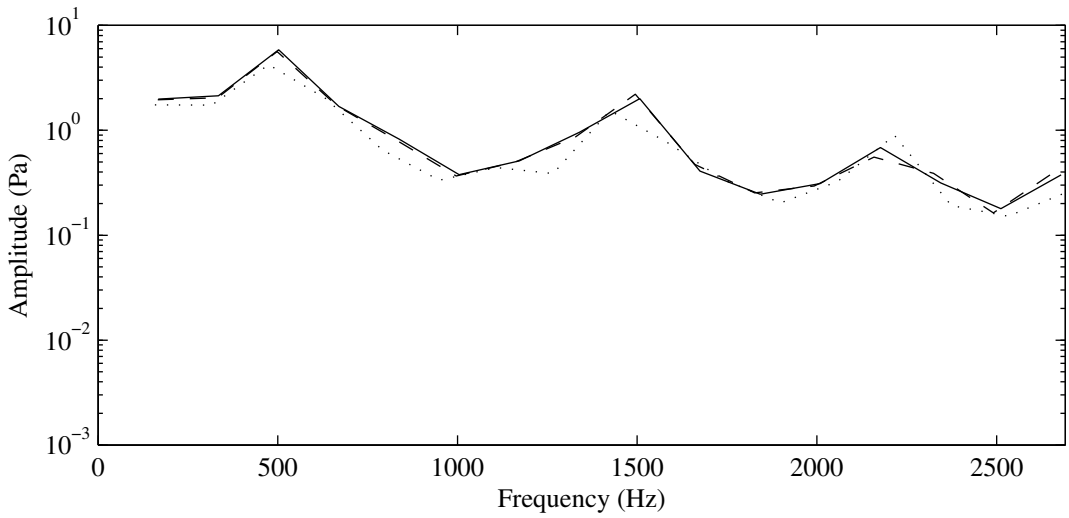

Figure 4.3: Envelopes of amplitude spectra of the mouth pressure predicted using two-mass model. (—) no film, f_0 = 167.5 Hz, (- -) 10 μm film, f_0 = 166.1 Hz, (···) 100 μm film, f_0 = 157.9 Hz.

effect on the mechanics of vocal fold vibration and may be neglected during collision of the vocal folds in general. However, the much thicker non-Newtonian mucus layer (around 100 μm) may significantly affect vocal fold oscillations.

Further investigation is required in order to determine and apply the effects of the fluid layer during the opening phase of the glottal cycle to a reduced-order model. Attention must be given to incorporate the mucosal wave motion of the vocal folds during separation as well as the more complex geometry of the fluid layer during vibration (e.g., through finite element modeling).

Due to the inherent limitations of the lumped parameter approximation described in this chapter, a more realistic model was needed to further investigate the potential effects of a liquid layer on vocal fold operation. While more complex computational models are well suited to parameterized studies, they lack the natural realistic effects that experimental models can provide. Furthermore, since a non-Newtonian model does not presently exist which can be used to model the mucus found on human vocal folds, a synthetic model with the application of a liquid layer was best suited for further investigation.

CHAPTER 5. PHYSICAL MODEL TESTING

5.1 Experimental Setup

As indicated in the introduction of this thesis, synthetic models of vocal fold vibration have been used extensively to study voice production. Synthetic models naturally exhibit certain realistic vocal fold behaviors that are hard to reproduce numerically or computationally, such as three-dimensional effects, non-linear material properties, and turbulence. While elaborate computational models may closely approximating certain aspects of true vocal fold function, physical models offer a more comprehensive testing ground for voice research. For the study of the effects of the liquid layer on voice production, a synthetic, silicone vocal fold model was selected over a more advanced numerical model due to its low cost and potential to yield results more quickly that numerical models. Furthermore, the results from the synthetic model were expected to be more accurate than what could be obtained from a computational model.

A hemilarynx (half larynx) model test setup was constructed that enabled the contact force of a single vibrating synthetic vocal fold to be measured. The test setup was constructed so that the model could be tested with and without the application of fluid to the surface of the model during vibration. An illustration of the setup is shown in Fig. 5.1. The setup consisted of an air supply which directed air through a set of valves to a plenum and then to a mounting plate where the synthetic hemilarynx vocal fold model was mounted. The setup enabled the simultaneous recording of dynamic force, subglottal pressure, radiated sound, and high-speed images of model motion.

The synthetic vocal fold model mounting assembly consisted of two acrylic blocks (see Fig 5.2): a vocal fold mounting block and a force gauge mounting block. The setup was very similar to that described in [51] in which synthetic vocal fold models were mounted in a rectangular cutout of a similar vocal fold mounting block. A force gauge spacer was mounted in a rectangular cutout of the force gauge mounting block. There was a 0.005 inch gap between the force gauge

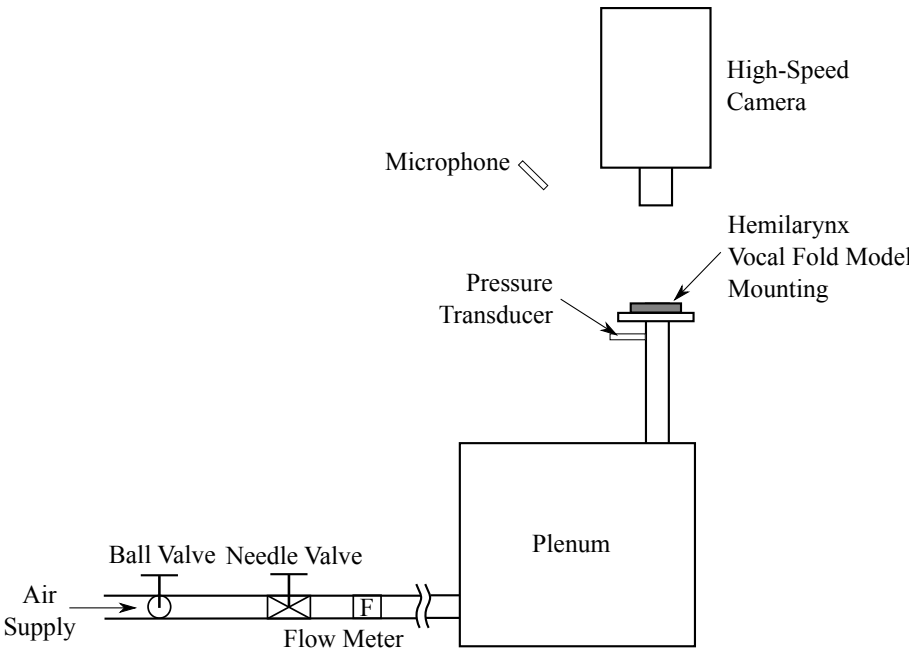

Figure 5.1: Illustration of synthetic vocal fold model test setup.

spacer and the opposing surfaces of the mounting block (see Fig.5.3). The vocal fold mounting block and the force gauge mounting block were bolted together along with intervening gasket material to seal the interface beyond the force gauge spacer, so as not to be between the silicone vocal fold model and the force gauge spacer which could interfere with accurate force measurements. A 0.005 inch gap also existed between the bottom of the force gauge spacer and the mounting plate beneath so that it would not be in contact with any other surface (0.005 inch gap; see Fig 5.3).

The force gauge was made of two pieces: a body and a faceplate (see Fig. 5.4). The faceplate was designed to allow liquid to diffuse evenly through its outer surface where the synthetic vocal fold model would come into contact during testing. The body was a rectangular piece of aluminum with a pocket for a fluid, holes for faceplate attachment screws, and a barbed fitting to attach a small, flexible fluid supply hose. A threaded hole on the back side of the body was used to attach the force gauge. The faceplate was made of aluminum with threaded holes to receive the attachment screws and a stepped cutout where a porous foam material could be mounted, through which the liquid diffused evenly. The porous foam insert was glued into the aluminum faceplate to seal the edges.

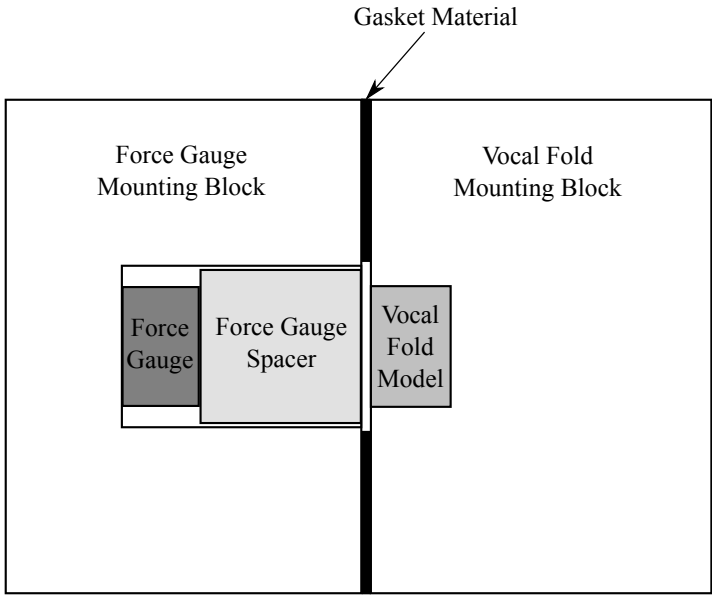

Figure 5.2: Synthetic vocal fold mounting assembly. The flow is normal to the page.

The porous foam insert (GenPore, www.genpore.com, Reading, PA) was cut from a sheet of 1/4" thick open cell polyethylene foam with a pore size of 50 μm. It was coated with a hydrophilic coating by the manufacturer to reduce surface tension effects and permit water-based fluids to flow more easily through it. Preliminary testing showed that all of the test fluids diffused evenly through the foam in the force gauge spacer assembly. Relatively low pressures were needed to cause fluid flow. It was observed that less than 1 inH_20 (about 250 Pa) was needed for water to flow through the faceplate. Pressures for relatively high flow rates (greater than 10 cc/hr) of all test fluids were developed with no leakage of the fluid between the faceplate and the body.

A plastic plate with a 2.54 cm hole was placed between the acrylic mounting blocks and the aluminum mounting plate, with a thin rubber gasket between the aluminum and plastic plate, sealing the gap (see Fig. 5.3). The surfaces of the mounting blocks and the plastic plate were flat and smooth so that the contact was airtight. The vocal fold mounting blocks were then bolted to the aluminum plate over the plastic plate and rubber gasket. An airtight seal was achieved everywhere in the vocal fold mounting except beneath the synthetic vocal fold, as desired, and negligible leakage through the 0.005 inch gaps near the force gauge spacer. The gaps between the force gauge spacer and its surroundings permitted the block to be suspended from the force gauge so that vocal fold contact forces would be transmitted completely, and solely, to the force gauge.

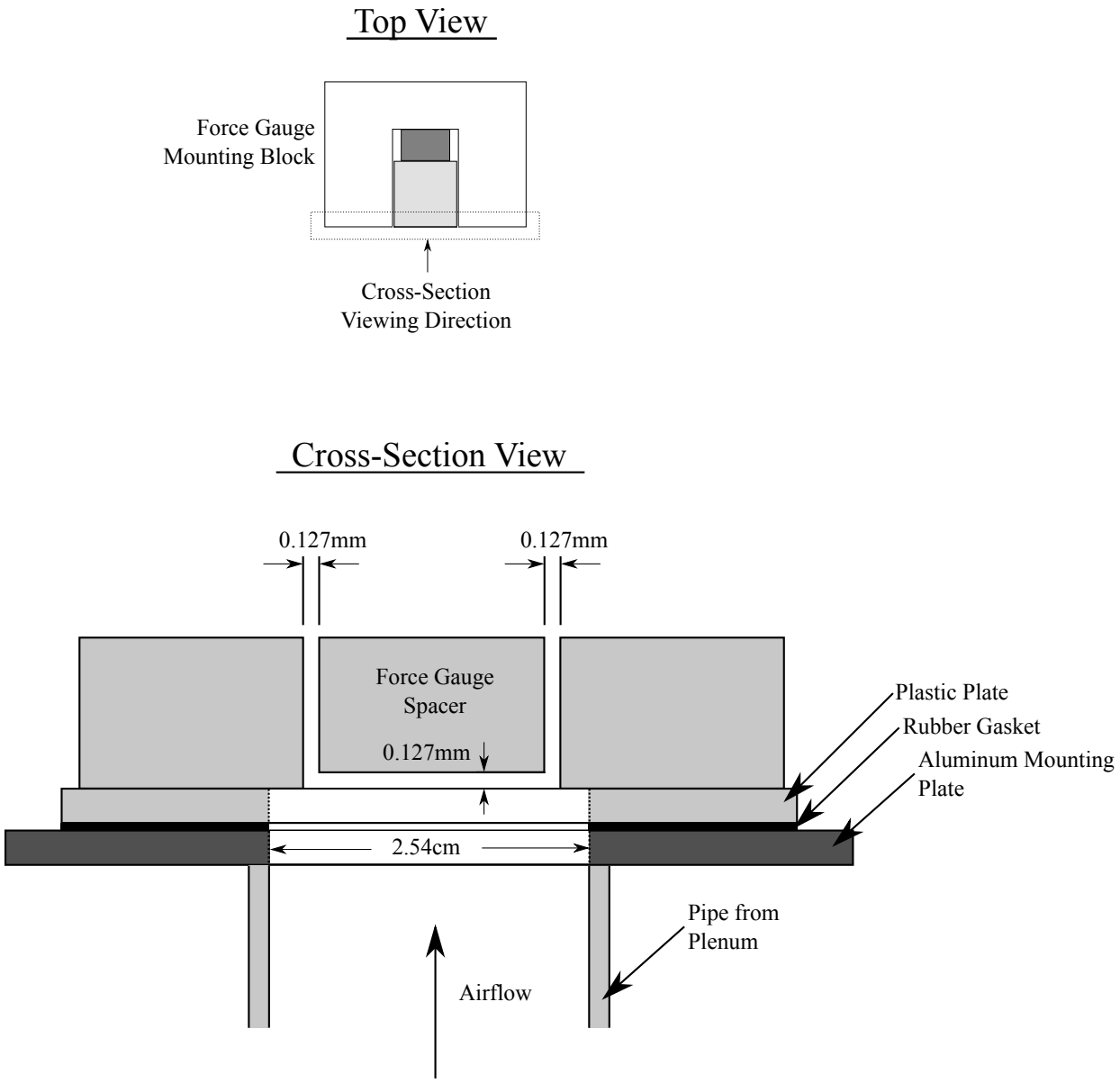

Figure 5.3: View of force gauge spacer showing exaggerated gaps between spacer block and surrounding mounting block.

Simultaneous recording of contact force, subglottal pressure, radiated sound, and high speed images were taken during testing (see Appendix H for sensor specifications and uncertainty). Contact force was measured using the same dynamic force gauge as used previously in this study (see Ch. 3). Subglottal pressure was measured using an Omega PX138 pressure transducer. Radiated sound pressure was recorded using Larson Davis 2520 1/4" free-field high-fidelity microphones with a Larson Davis 2221 pre-amplifier. All data (except for the high speed images)

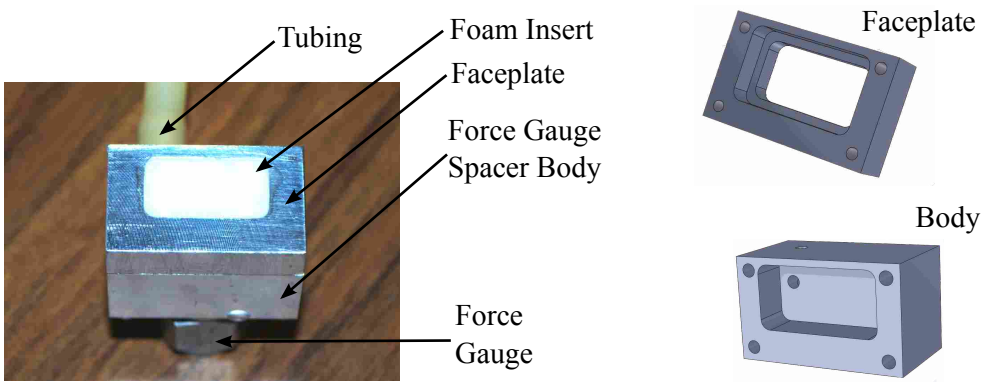

Figure 5.4: Force gauge spacer assembly. The porous foam insert where the vocal fold model comes into contact with the spacer block can be seen in this view. In the background the force gauge and tubing are also visible.

were recorded for five seconds at 40 kHz. Images measuring 256x880 pixels were acquired at 6000 frames per second, yielding approximately 48 frames per oscillatory cycle of the vocal fold model and a resolution of 47.6 pixels per millimeter (21.0 μm per pixel). All images were acquired with the same lighting and camera settings so that the image quality (e.g., brightness and contrast) were consistent between data sets.

5.2 Testing

Appendix I gives a summary of the 126 test runs that were made in this study, listed in the order in which they were taken. Each of five different fluids (3 Newtonian: oil, water, and glycerin; 2 non-Newtonian: XG1 and XG2 which were two different mixtures of xanthan gum in distilled water) were tested twice in random order. The xanthan gum mixtures were not measured precisely for the weight percent of xanthan gum, but the weight percent was close to 1% and the rheological parameters G', and G'' are reported in Appendix A. Each fluid was tested twice in order to observe the repeatability of the measurements. For each case, dry or wet, six mean subglottal pressures were tested in random order. A dry test was run between each wet case to minimize the error associated with long-term effects. Thus, each wet case was compared with the dry case just before and just after it. Separate faceplates were used for each case (6 faceplates: 5 wet, 1 dry). Between each recording group, a baseline recording of all sensors was made with the airflow

off. A calibration target was recorded with the high-speed camera to ensure accurate distance measurements throughout testing.

For each group, dry or wet, the appropriate faceplate was attached to the force gauge spacer. A syringe pump (Model BSP 99, Braintree Scientific Inc., Braintree, MA) was set to have a flow rate of 1.45 cc/hr, turned on and allowed to flow for a period of time until the fluid was flowing evenly and continuously through the faceplate. Figure 5.5 shows an example of steady fluid flowing through the faceplate. The fluid can be seen flowing upward as "fingers." Also for each group, the subglottal air pressure was repeatedly raised and lowered to determine phonation onset and offset pressures. This was done multiple times to ensure accurate readings. The glottal airflow rate, room temperature, and onset/offset phonation threshold pressures were recorded. The mean subglottal pressure was adjusted for the first trial, the camera and LabVIEW box were set to record and then, under steady conditions, triggered to record simultaneously with the use of a waveform-generated TTL pulse. The airflow was adjusted for the next pressure and the data recorded as before.

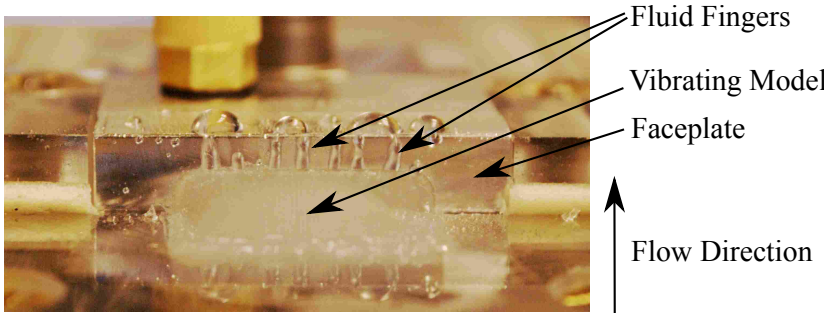

Figure 5.5: View of steady fluid flow. The fluid "fingers" are the result of the fluid being blown upward by the glottal airflow as it flows through the foam insert.

After data for all of the pressures were obtained for a given group, the airflow and the syringe pump were turned off, the faceplate was removed and wrapped in plastic wrap to prevent drying, and the force gauge spacer was removed, cleaned, and dried prior to its next use. The synthetic vocal fold model was carefully cleaned with a cotton swab that had been dipped in ethyl alcohol, and then dried with a dry cotton swab using care not to damage the model or its attachment to the mounting blocks.

Preliminary testing revealed that the liquid flow rate during vibration had no effect on the measured output variables. Flow rates of 1.45, 2.89, 5.80, and 11.60 cc/hr were tested, showing no significant effects for a given fluid. Therefore, a single flow rate of 1.45 cc/hr was chosen for further testing.

Figure 5.6 shows a sequence of high speed images in which the vocal fold model made contact with the surface of the faceplate. At t = 3.333 ms there is closure across the entire surface. This sequence corresponds to the dry case with a mean subglottal pressure of 1.9 kPa.

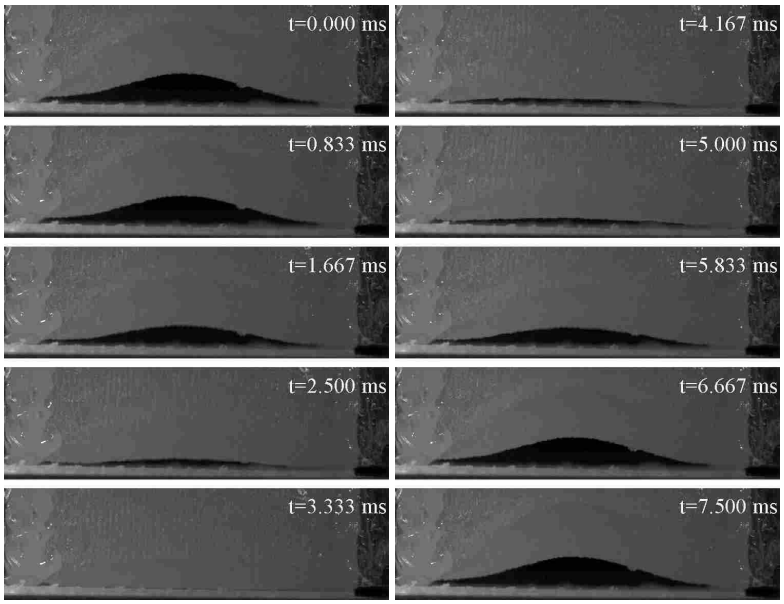

Figure 5.6: Sequence of images showing good contact with surface.

Figure 5.7 shows an example where poor contact is made between the vocal fold model and the hemilarynx surface. A small gap (approximately 100 μm) remains between the model and the surface at maximum closure (t = 2.5 ms). This sequence corresponds to the oil case with a mean subglottal pressure of 1.5 kPa.

Figure 5.8 shows a sequence of high speed images where there is evidence of the presence of fluid at the central medial (bottom-center in the image) edge of the model. There are two drops of fluid that are whipped back and forth and almost stick to the faceplate surface (seen at t = 2.000 ms to t = 2.666 ms, indicated at t = 2.500 ms). At t = 0.000 ms, there is a drop of fluid that is seen on the right hand side of the images and remains visible in many of the images in this sequence.

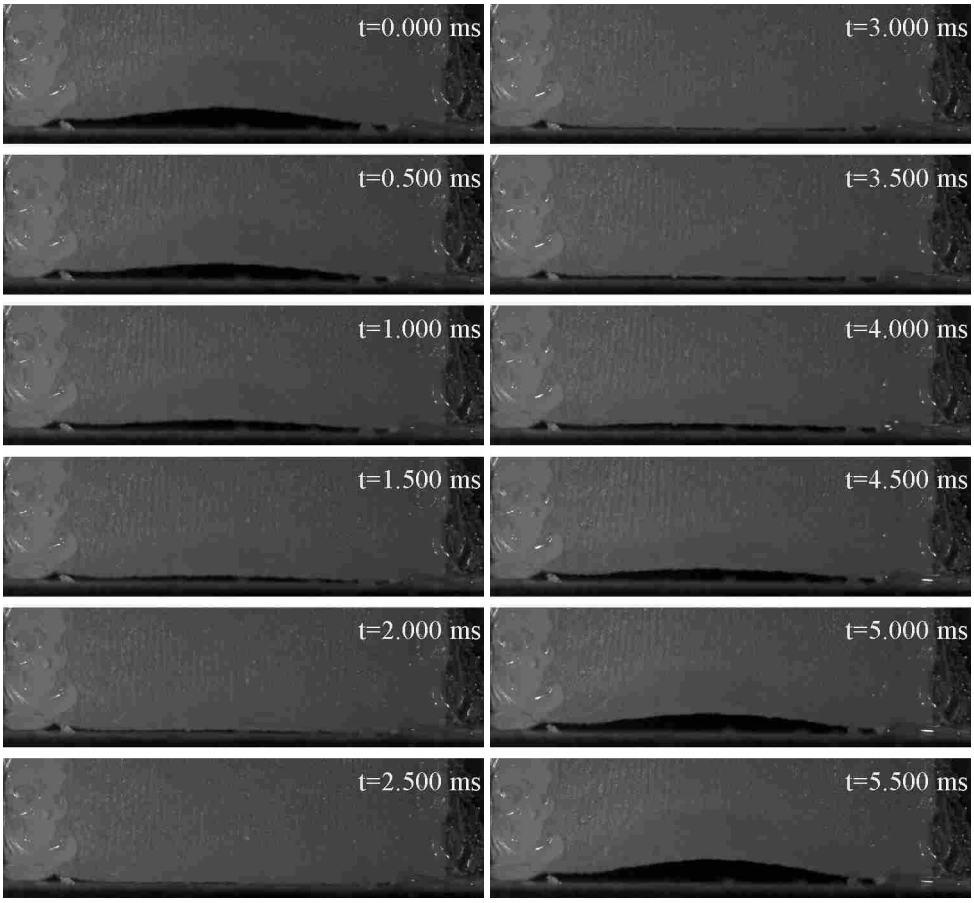

Figure 5.7: Example of poor contact. A gap (approximately 100 μm) can be seen between vocal fold and hemilarynx surface at maximum closure (t = 2.5 ms).

Fluid aggregation can be seen in the lower right hand corner of the images which is near the fixed border of the silicone vocal fold model. This sequence of images illustrates the presence of fluid between the model and the faceplate during vibration.

5.3 Analysis

The distance between the medial edges of the models at the widest point of the glottal opening is called the glottal width. From the high-speed image data, the half-glottal width was measured from the force gauge spacer to the medial edge of the vocal fold as shown in Figure 5.9.

The glottal area is the smallest cross-sectional area of the glottis. Figure 5.10 shows an example of the measured glottal area from a high speed image. The glottal area is highlighted. The glottal area was automatically tracked through the sequence of high speed images using custom

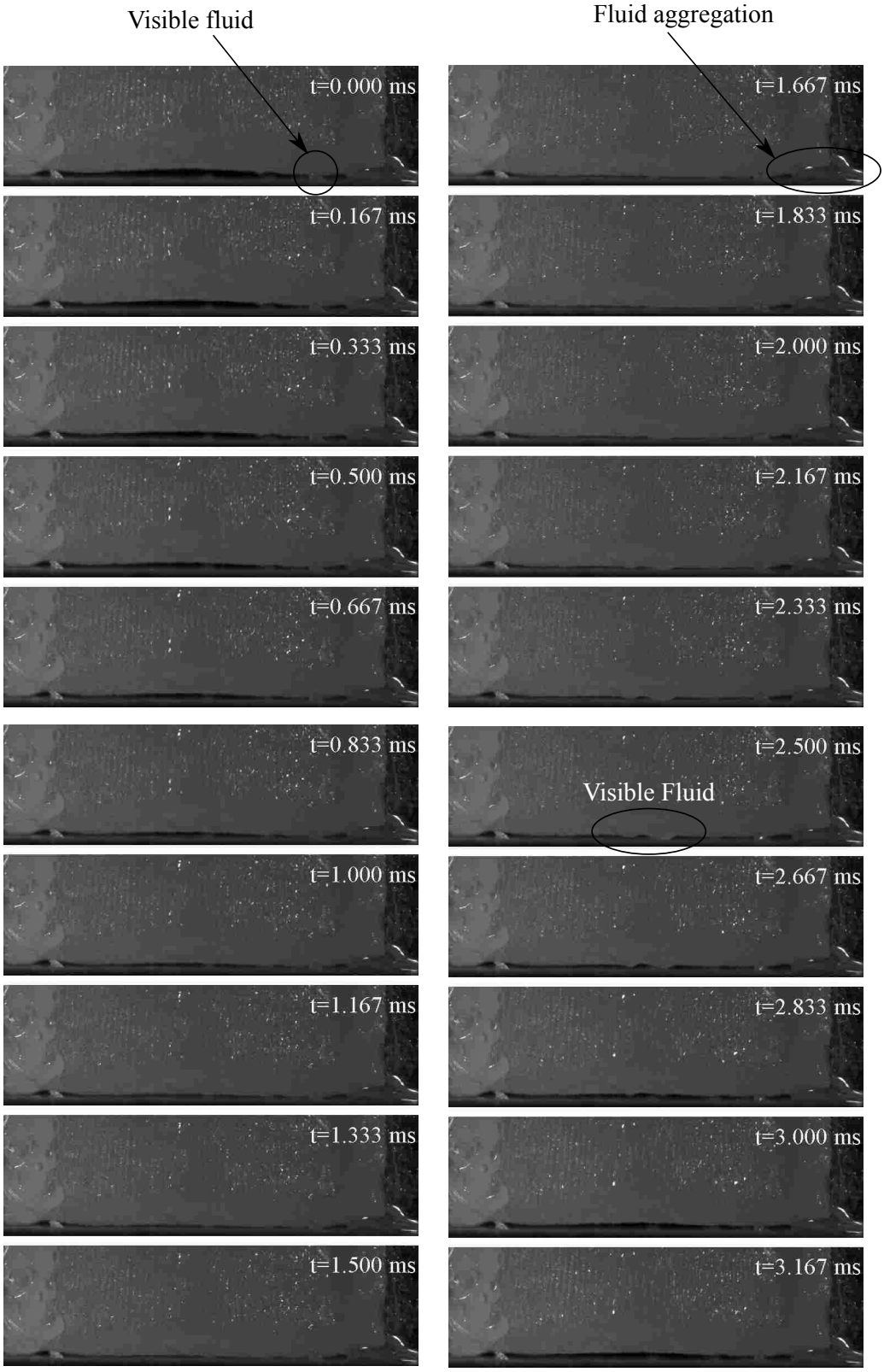

Figure 5.8: Sequence of images showing fluid at central medial edge of the model.

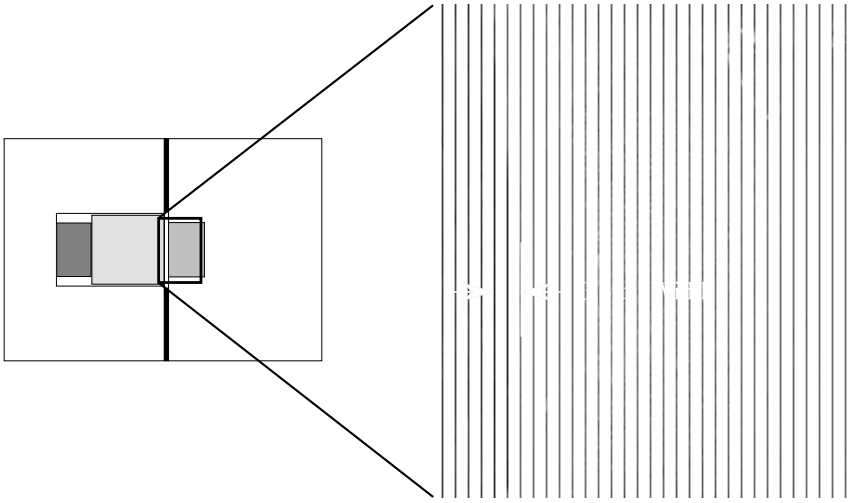

Figure 5.9: Glottal width measurement.

MATLAB subroutines. Since the lighting and camera settings were the same for all data sets, the image quality between the different data sets was virtually the same. Therefore, the same pixel intensity threshold value was used for all images. On some images there are obstructions or occlusions such as the presence of fluid which affect the glottal area measurement. These were observed to account for less than 10% of the maximum glottal area or ±1.3 μm in most cases. Additionally, the intensity of the edge of the vocal fold model changed throughout the cycle affecting the boundary of the glottal area. The region where this occurs is approximately 4 to 8 pixels wide in most cases and it affects about 60% of the perimeter which equates to an area of approximately 0.5 mm^2 or 4% error in the glottal area measurement. The image resolution was measured using calibration targets to be 21.1 μm per pixel with an uncertainty of ±0.14 μm or less than 0.7%. The combined uncertainty in the measurement of glottal area is estimated to be about 14.7% of the maximum glottal area or about ±1.9 mm^2.

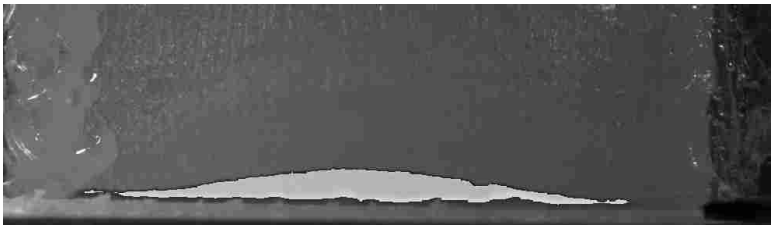

Figure 5.10: Example of glottal area measurement. The glottal area is highlighted.

5.4 Results and Discussion

Figures 5.11 and 5.12 show the measured peak-to-peak force for each fluid and set. In all plots, the solid line is the wet case for the indicated fluid, the dashed and dotted lines indicate the peak-to-peak forces from the dry cases just before and after the wet case, respectively. Most cases show very little change in peak-to-peak force from the dry cases to the wet case and very little change between the dry cases before and after. Figure 5.11d shows an exception to this as the dry case just before is significantly higher than the case with glycerin or the dry case after. This is assumed to be an anomaly due to an unknown error in the experimental measurements for that case.

Figures 5.11e and 5.11f both show that the peak-to-peak force for olive oil decreased between 12-27% from the dry cases before and after. Figures 5.12b and 5.12d show a decrease of about 10% in force for XG1 and XG2, whereas, the previous XG1 and XG2 cases (see Figs. 5.12a and 5.12c) show a smaller drop of about 5-7% in force. Also, peak-to-peak force between dry cases increases from 5-7% in Figs. 5.12a and 5.12c which were from a group of data taken previously to 10-13% in Figs. 5.12b and 5.12d. This could be the result of some minor changes in the model during testing.

Figures 5.13 and 5.14 show the glottal airflow rate for each fluid case. There is almost no change in flowrate for water or glycerin. There is a significant increase of about 10-20 standard cubic feet per hour (SCFH) which corresponds to a 20-40% increase for olive oil, XG1, and XG2. The increased airflow is attributed to the difference in location of the permeable foam inserts in the faceplates. The faceplates used for water, glycerin, and the dry cases had a foam insert that protruded approximately 0.35 mm beyond the aluminum faceplate surface whereas the olive oil, XG1, and XG2 faceplates were almost perfectly flush. This protrusion decreased the glottal area and for a given subglottal pressure, also decreased the airflow rate.

Figure 5.15 shows the difference between the faceplates where the foam insert protruded slightly and a case where the foam insert was flush with the faceplate surface. The solid green line indicates the surface of the foam insert. Both images were taken for cases with the same mean subglottal pressure at the peak glottal opening. The glottal width and area for case (b) is 23% larger than for case (a), presumably due to the location of the foam insert. The higher flow rates were observed for the olive oil, XG1, and XG2 cases. This is attributed to the foam insert being

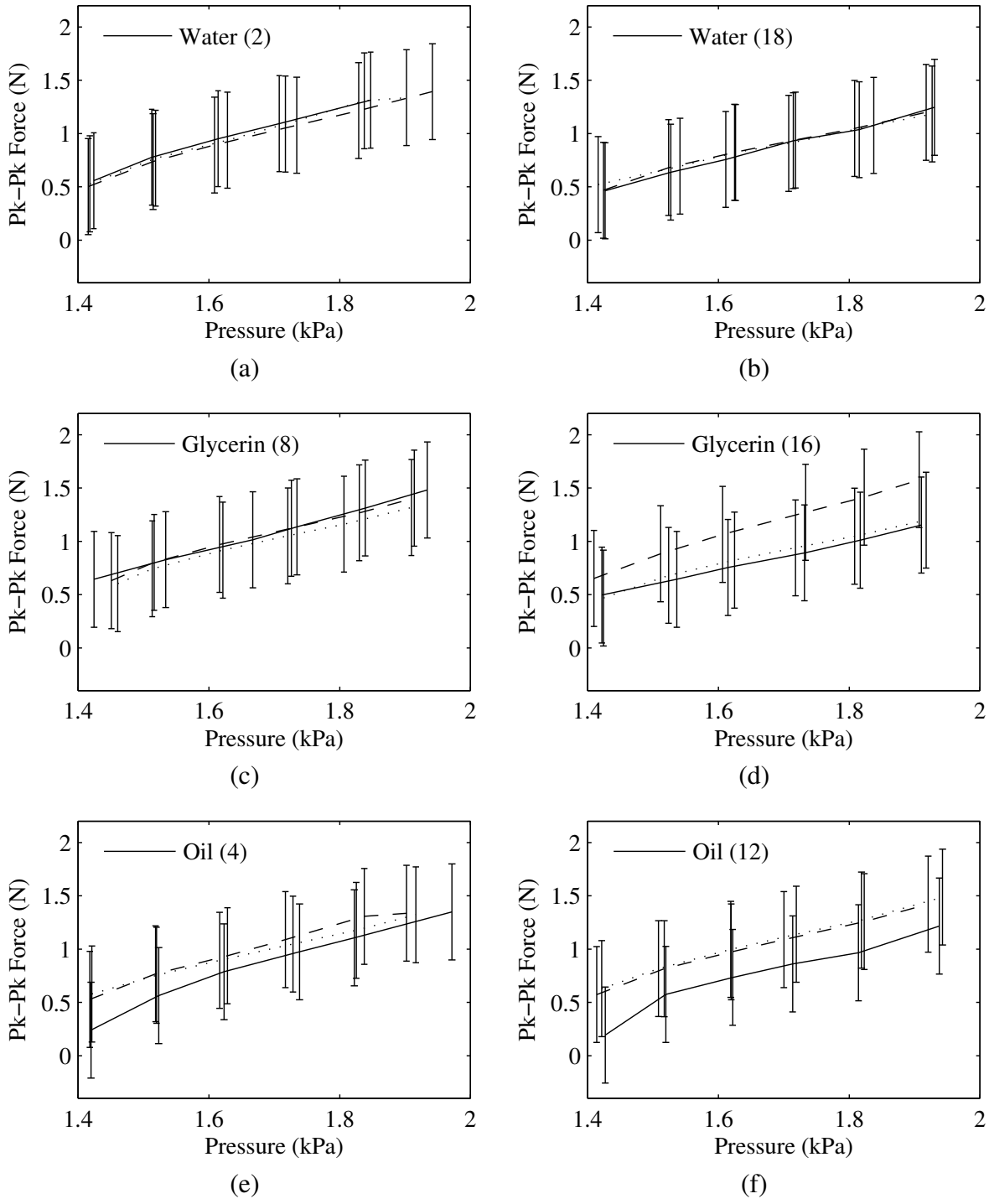

Figure 5.11: Peak-to-peak force vs. mean subglottal pressure for water, glycerin, a oil; (—) fluid case, (- -) dry before, (···) dry after. The number in parenthesis in the legend after the fluid name is the test case number which corresponds to the data given in Appendix B.

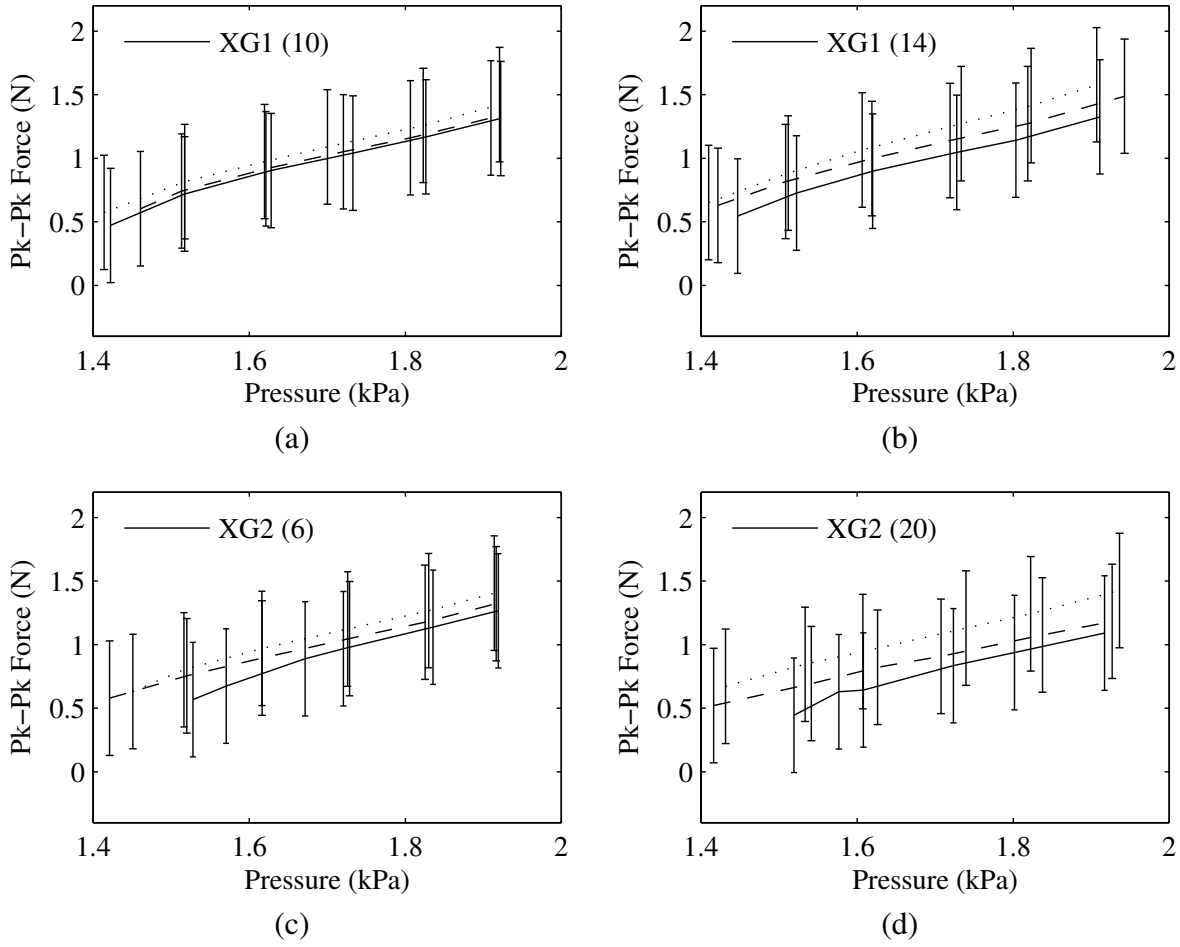

Figure 5.12: Peak-to-peak force vs. mean subglottal pressure for XG1 and XG2; (—) fluid case, (- -) dry before, (···) dry after. The number in parenthesis in the legend after the fluid name is the test case number which corresponds to the data given in Appendix B.

flush with the faceplate for these cases. For the other fluid cases, the foam insert protruded beyond the edge of the faceplate leaving a glottal area that was reduced by 37% and consequently a lower flow rate at a given subglottal pressure. It is unclear whether the change in airflow rate is mostly attributable to the location of the foam insert (protruding or flush) or the fluid.

Figures 5.16 and 5.17 show the measured fundamental frequencies, F_0, for each fluid and each set. The largest differences in fundamental frequency are seen for olive oil, but it is only a difference of less than 3 Hz or 2.4%, which is a relatively small change in voice pitch. In addition, these changes in frequency are seen for the three fluids for which the faceplates have foam inserts

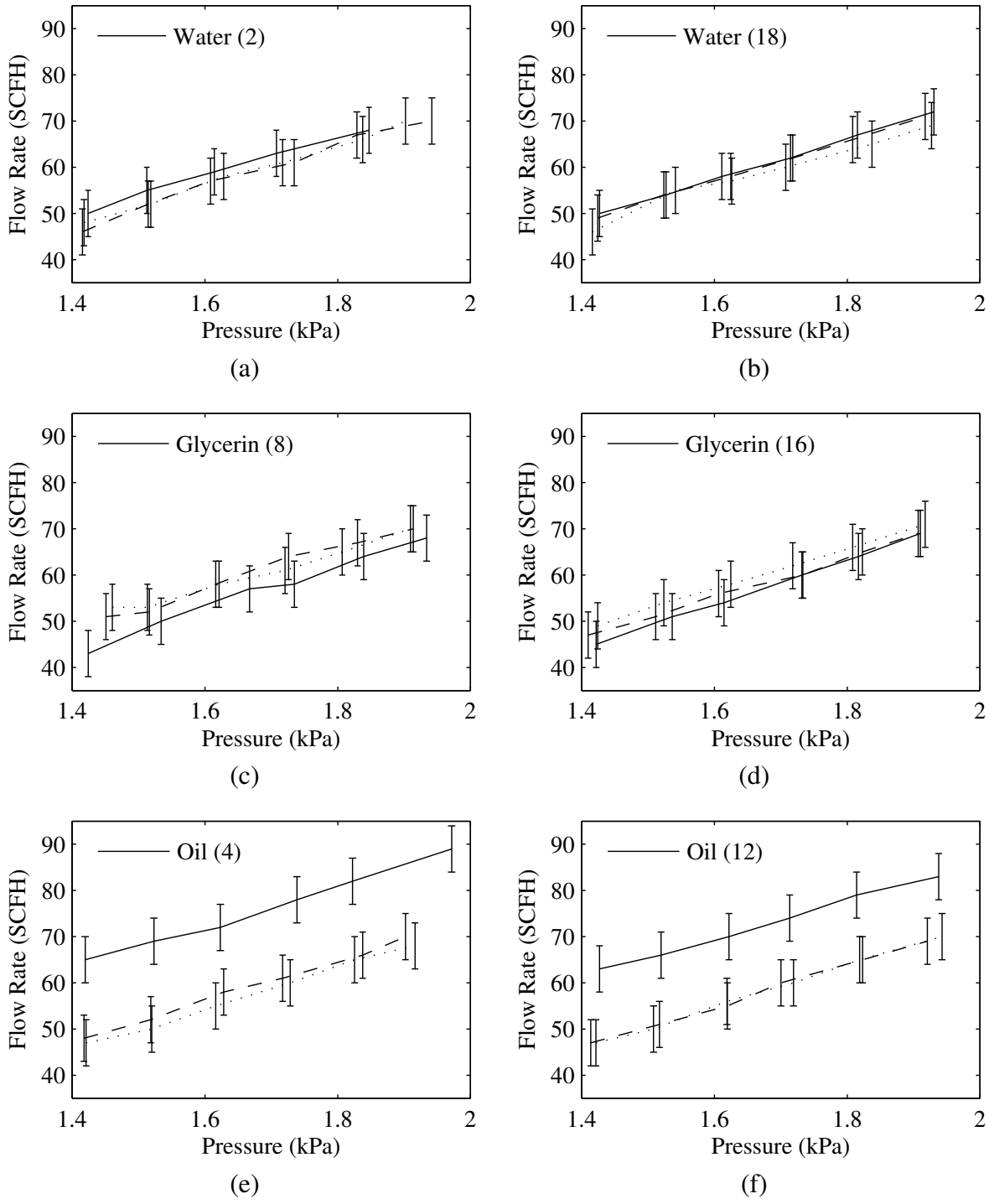

Figure 5.13: Air flow rate vs. mean subglottal pressure for water, glycerin, and oil; (—) fluid case, (- -) dry before, (···) dry after. The number in parenthesis in the legend after the fluid name is the test case number which corresponds to the data given in Appendix B.

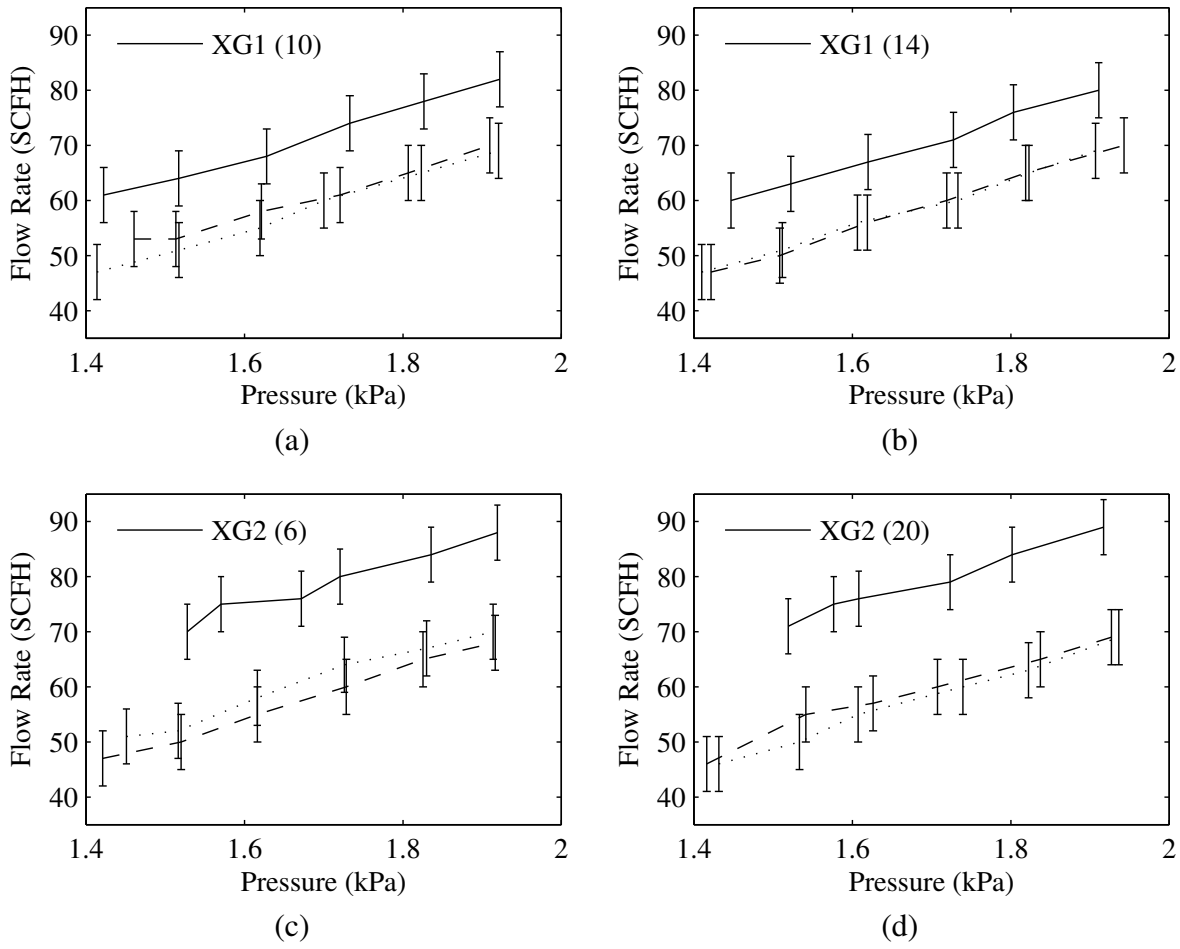

Figure 5.14: Air flow rate vs. mean subglottal pressure for water, glycerin, and oil; (- -) dry before, (···) dry after. The number in parenthesis in the legend after the fluid name is the test case number.

that are almost flush with its surface (olive oil, XG1, and XG2). These differences in frequency are attributed to the location of the foam inserts in the faceplates as well.

Figures 5.18-5.21 show the ratios of amplitudes of the first and second harmonics to the amplitude of the fundamental frequency taken from the microphone acoustic data. The first harmonic ratio is reduced by less than 12% for pressures above 1.6 kPa in almost every case (except oil where it decreases by up to 15%). All other first harmonic ratios show less than 5% change from the dry case. The second harmonic ratio is up to 36% higher for oil and XG2. There is a smaller increase of less than 10% for XG1. All other fluids show no significant change for the second harmonic ratio.

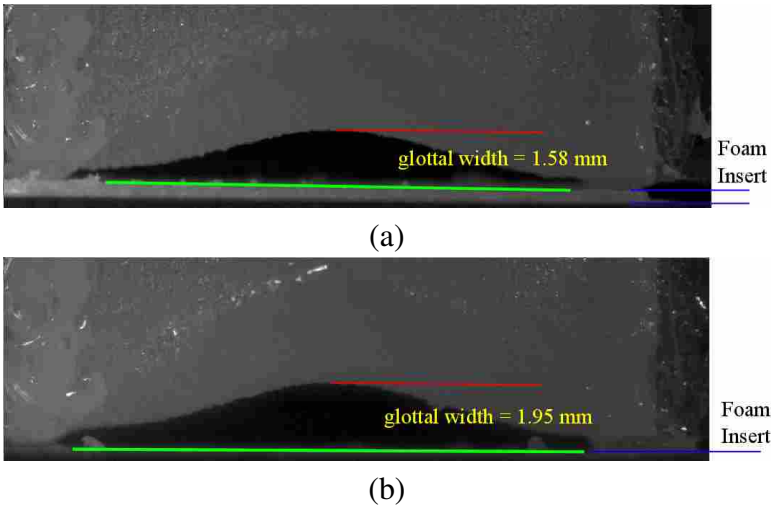

Figure 5.15: Comparison of the locations of foam inserts for different faceplates. The solid green line indicates the location of the surface of the foam insert with which the vocal fold model comes into contact during phonation. a) shows the case where the foam protrudes about 0.35 mm beyond the surface of the faceplate, b) shows the case where the foam is flush with the rest of the faceplate surface.

Figures 5.22 and 5.23 show the glottal widths for each fluid and each set. There is virtually no change for water or glycerin and only a small increase in glottal width for olive oil, XG1, and XG2. The changes are small and on the order of 0.35 mm – which further corroborates that the changes are rightfully attributed to the location of the porous foam inserts within the faceplates.

The glottal areas were tracked through the high speed image sequences, normalized in time and amplitude, and plotted together for all cases in Fig. 5.26. As can be seen, the general shape of the waveform varies little between cases. There is a spread in the width of the waveform during the closing phase of the cycle. There is also a characteristic bump that occurs during the opening phase (t = 0.7 to 1.0 sec). This bump occurs at subglottal pressures above about 1.7 kPa. This stagnation of increasing area occurs as a result of the rotational momentum of the vocal fold. At lower pressure, the vocal fold simply moves back and forth, but at higher pressures the medial edge of the vocal fold rotates as well. During this rotation, the glottal area increases much more slowly than before. This feature is equally manifest in wet and dry cases alike and is not a characteristic result of the presence of a fluid.

Based on these findings it was concluded that the fluid had little if any effect on the operation of the synthetic vocal fold model. To further verify this conclusion, a burst of high rate fluid

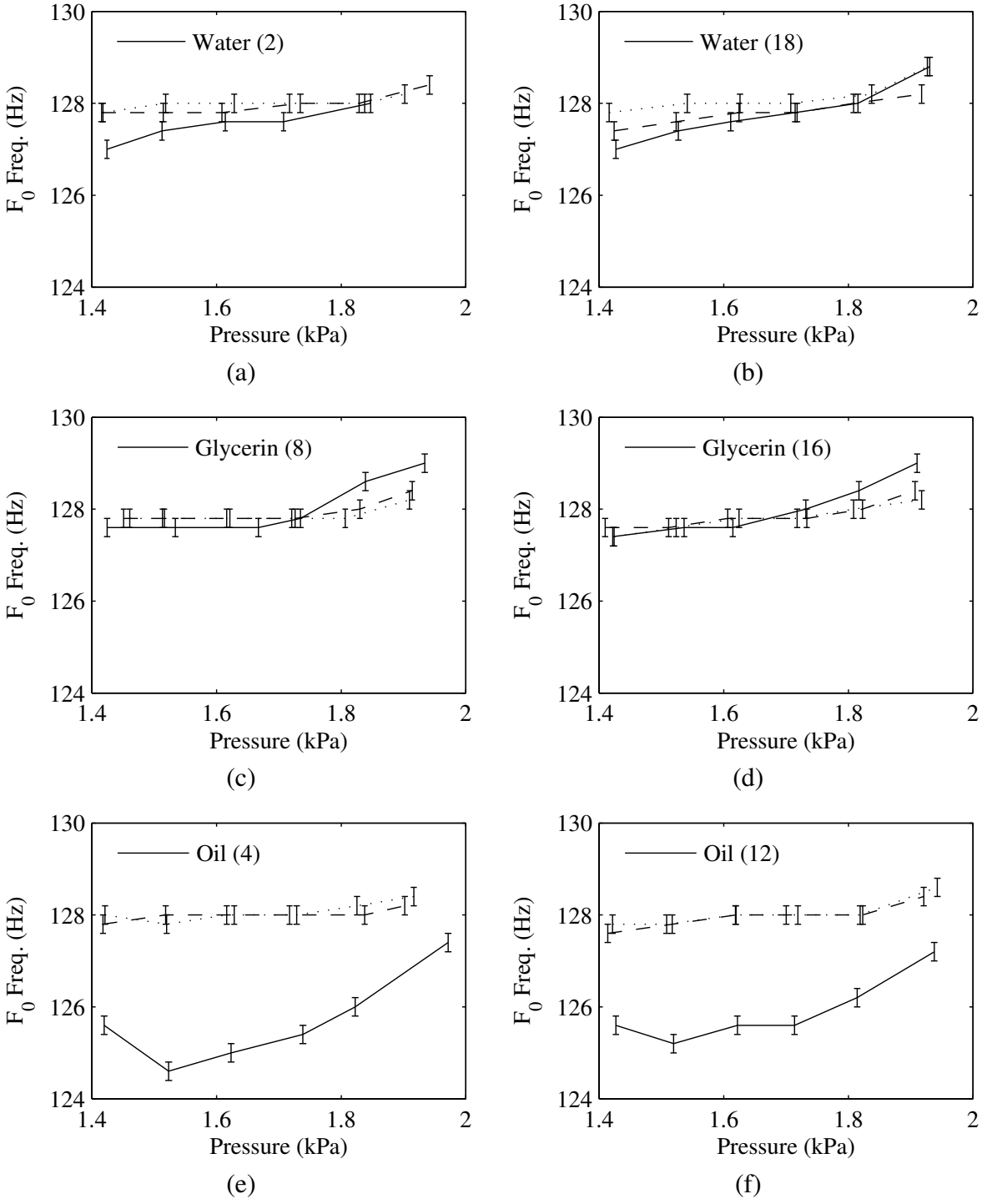

Figure 5.16: Fundamental frequency, F_0, vs. mean subglottal pressure for water, glycerin, and oil; (—) fluid case, (- -) dry before, (···) dry after. The number in parenthesis in the legend after the fluid name is the test case number which corresponds to the data given in Appendix B.

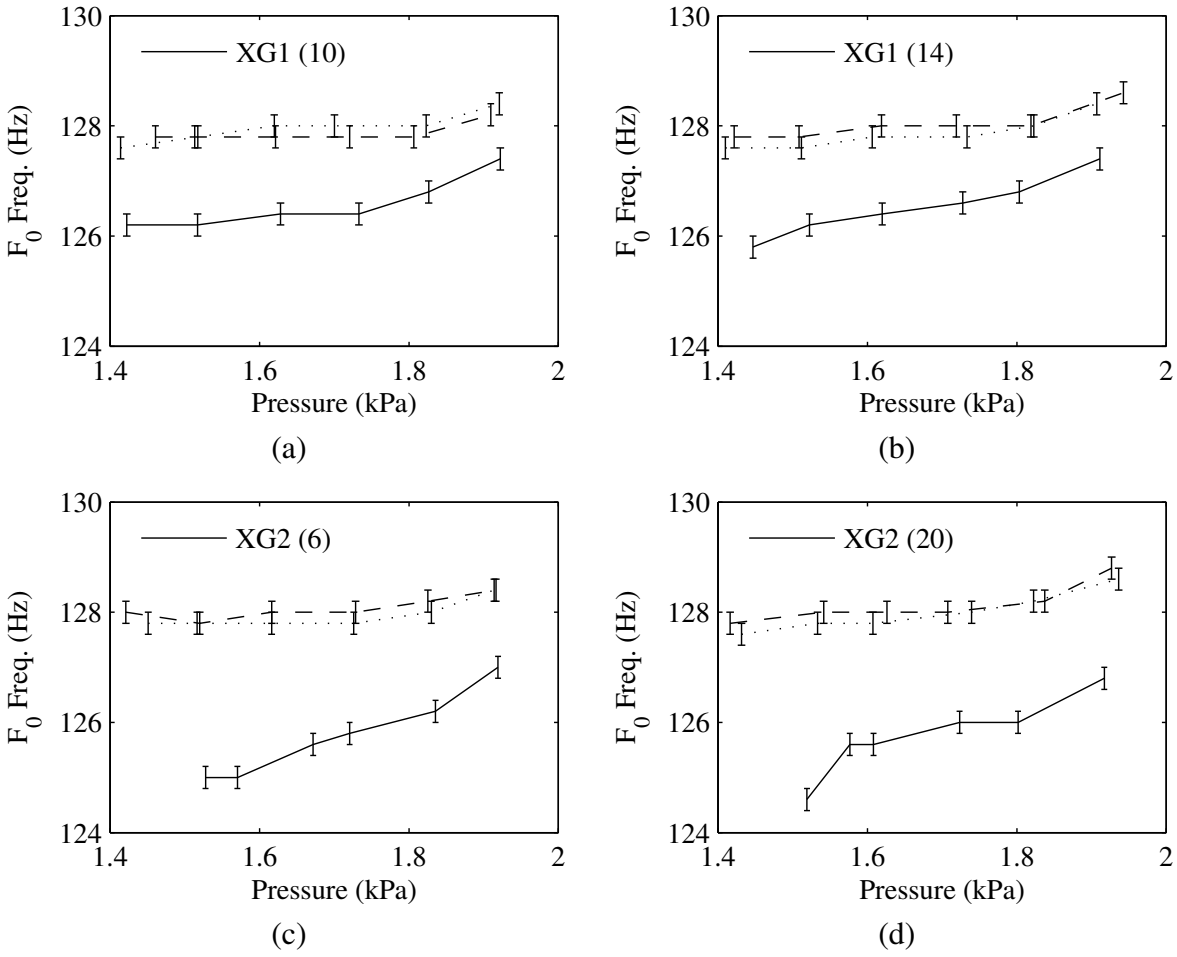

Figure 5.17: Fundamental frequency, F_0, vs. mean subglottal pressure for XG1 and XG2; (—) fluid case, (- -) dry before, (···) dry after. The number in parenthesis in the legend after the fluid name is the test case number which corresponds to the data given in Appendix B.

flow through the faceplate was made during vibration with the different fluids and the real-time measurements of mean subglottal pressure, peak-to-peak force and fundamental frequency were monitored. Just after the surge of fluid occurred, a rise in mean subglottal pressure and peak-to-peak force was observed that decayed relatively slowly, over the course of a few seconds. The buildup of fluid in the contact area of the faceplate also diminished over the course of a few seconds and correlated with the decreasing mean subglottal pressure and peak-to-peak force. Peak-to-peak force is proportional to mean subglottal pressure. The rise in peak-to-peak force during the surge of fluid flow was the same as would have been observed for the corresponding increased mean

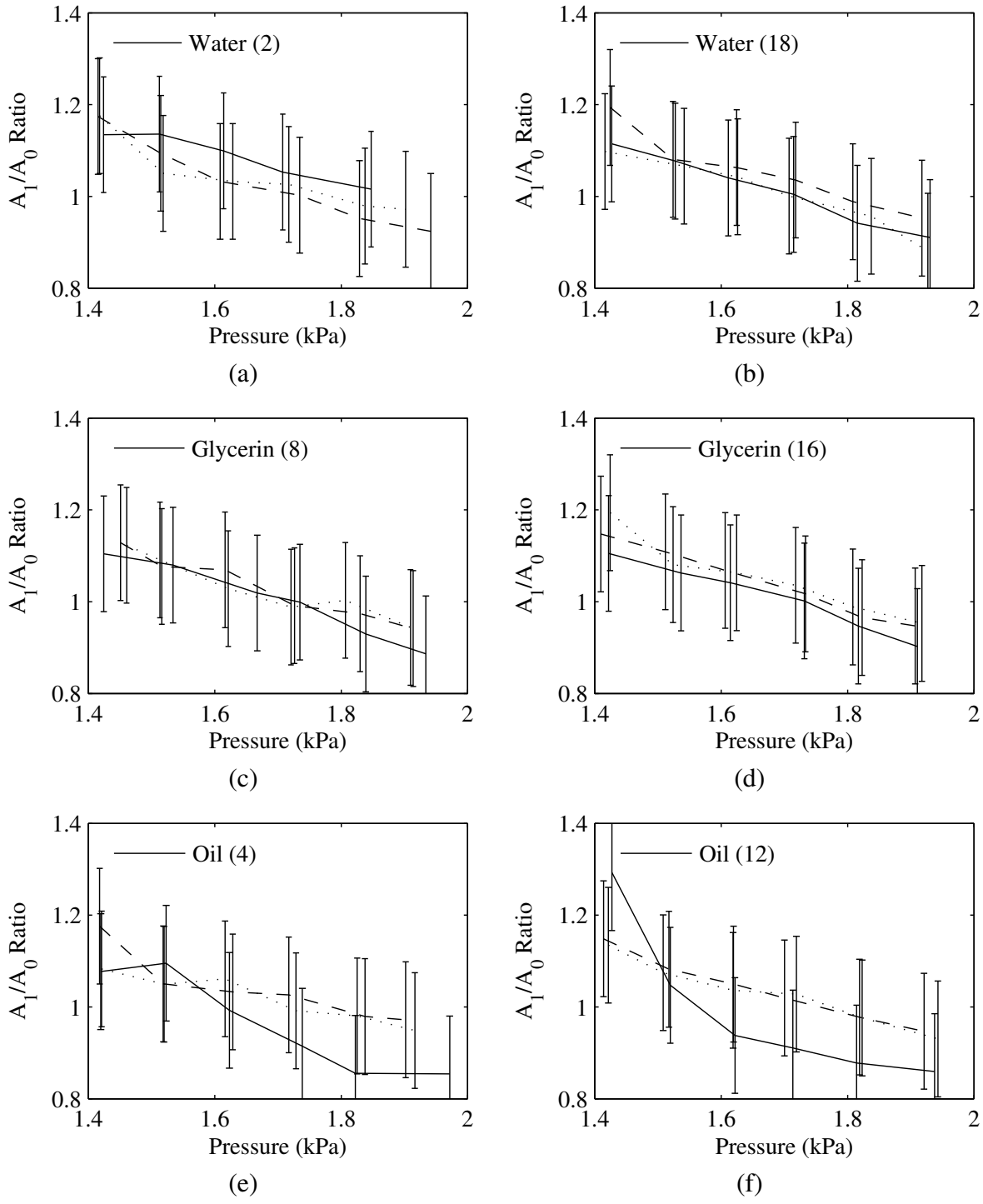

Figure 5.18: Ratio of first harmonic amplitude (dB) to fundamental frequency amplitude (dB) vs. mean subglottal pressure for water, glycerin, and oil; (—) fluid case, (- -) dry before, (···) dry after. The number in parenthesis in the legend after the fluid name is the test case number which corresponds to the data given in Appendix B.

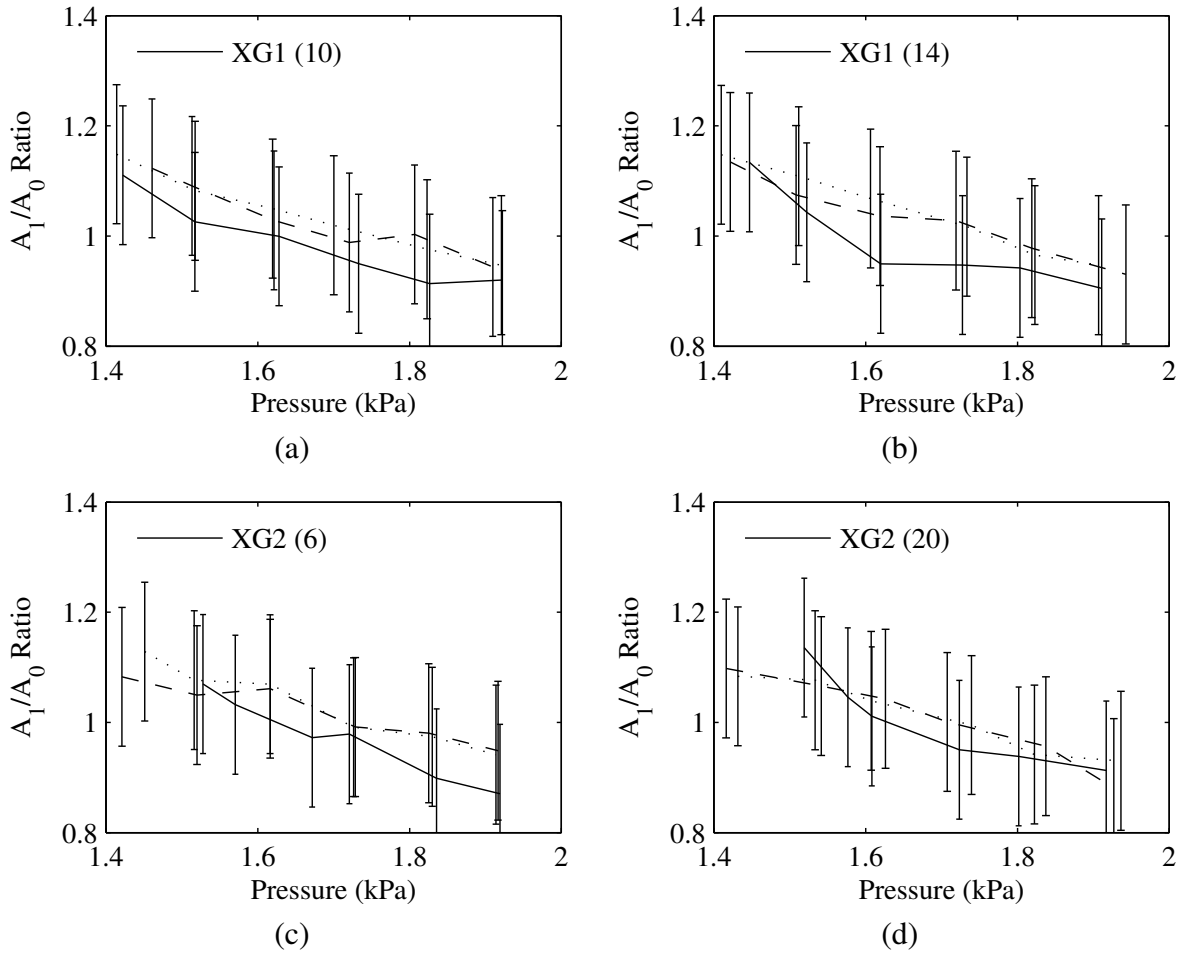

Figure 5.19: Ratio of first harmonic amplitude (dB) to fundamental frequency amplitude (dB) vs. mean subglottal pressure for XG1 and XG2; (—) fluid case, (- -) dry before, (···) dry after. The number in parenthesis in the legend after the fluid name is the test case number which corresponds to the data given in Appendix B.

subglottal pressure. In other words, the increase in peak-to-peak force was entirely attributable to the increase in mean subglottal pressure.

The increase in mean subglottal pressure is simply the result of a sudden reduction in glottal area due to the presence of a mass of fluid. As the fluid was blown upward by the airflow and cleared out of the glottis, the glottal area increased back to what it had been before the burst of fluid and the mean subglottal pressure and peak-to-peak force returned to their steady values that existed prior to the burst of fluid.

Table 5.1 summarizes the mean onset and offset pressures for each fluid. The onset/offset pressures for all wet cases except glycerin increase by 2 to 14%. An increase in phonation thresh-

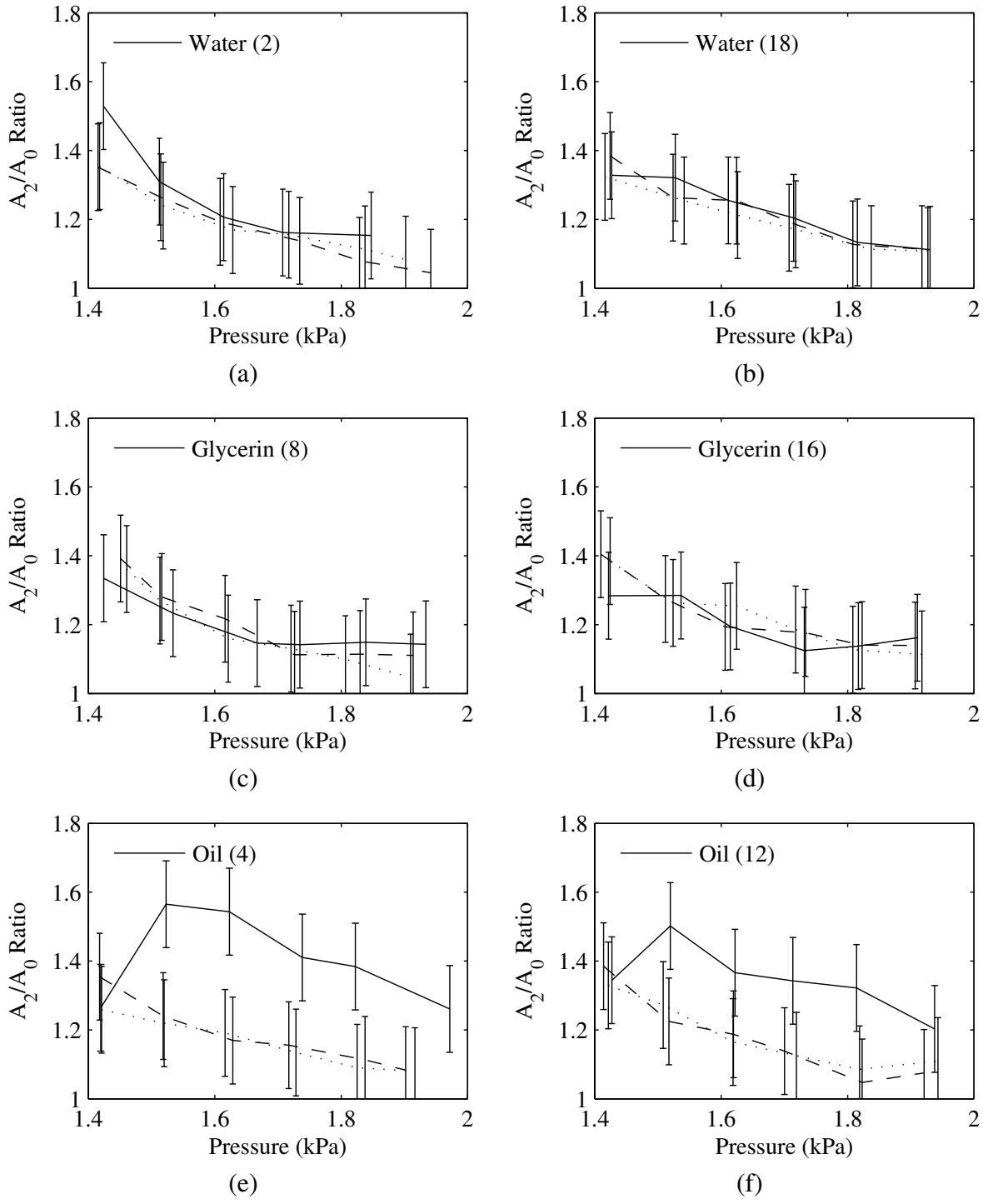

Figure 5.20: Ratio of second harmonic amplitude (dB) to fundamental frequency amplitude (dB) vs. mean subglottal pressure for water, glycerin, and water; (—) fluid case, (- -) dry before, (···) dry after. The number in parenthesis in the legend after the fluid name is the test case number which corresponds to the data given in Appendix B.

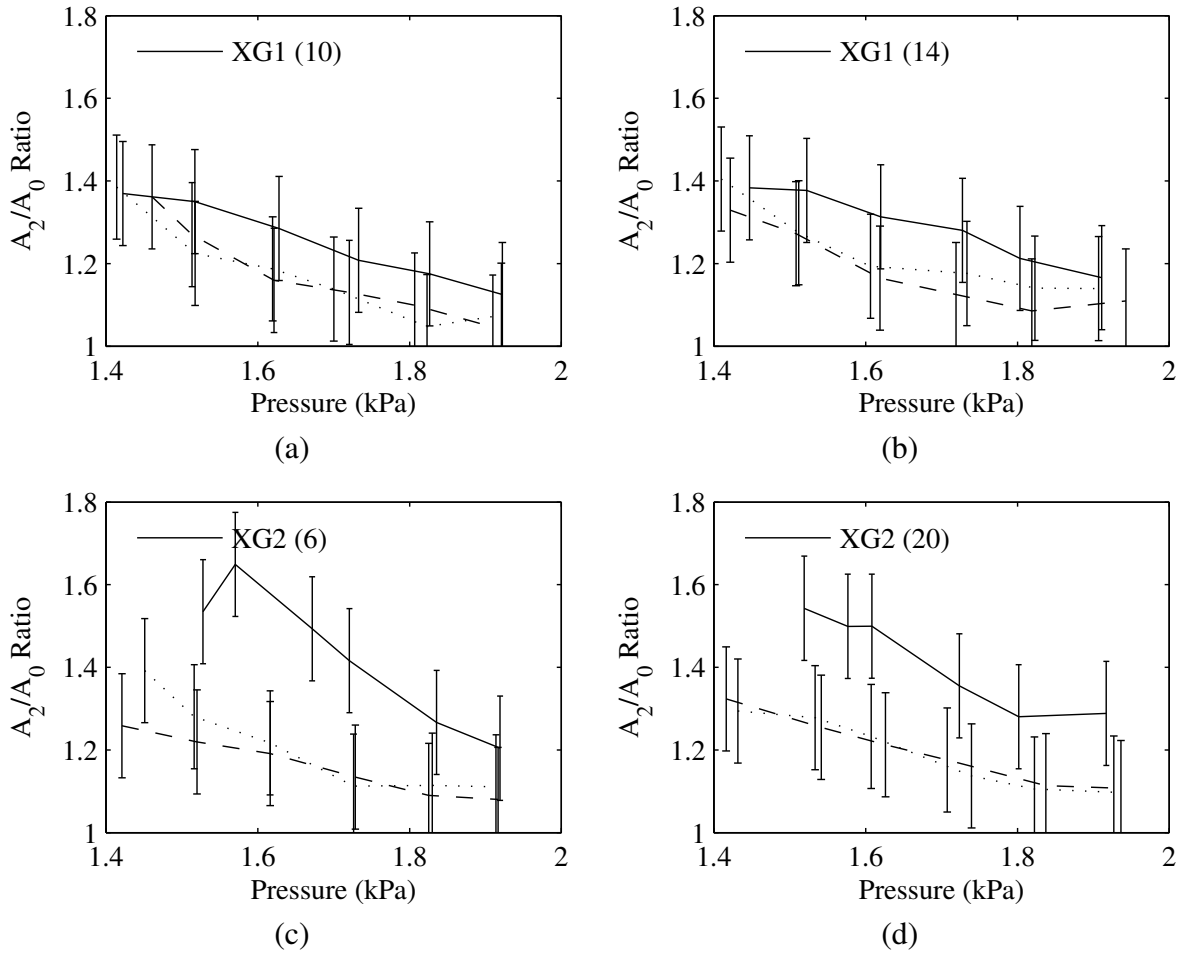

Figure 5.21: Ratio of second harmonic amplitude (dB) to fundamental frequency amplitude (dB) vs. mean subglottal pressure for XG1 and XG2; (—) fluid case, (- -) dry before, (···) dry after. The number in parenthesis in the legend after the fluid name is the test case number which corresponds to the data given in Appendix B.

old pressure results in increased vocal effort. The changes are consistent for each fluid between fluid tests. The most notable change is for XG2 where the onset and offset pressures increased by up to 13.6%, from 1.3 kPa to 1.5 kPa. This is a significant change in phonation threshold pressure. Threshold pressures also increased by 6% for oil. The increase for water and XG1 are comparable. Another noteworthy feature is that the application of glycerin reduced phonation threshold pressure. The significance of this finding is somewhat magnified when considering the anecdotal use of honey for voice therapy. [64] Knowledge of these changes in phonation threshold pressure could lead to improved voice care.

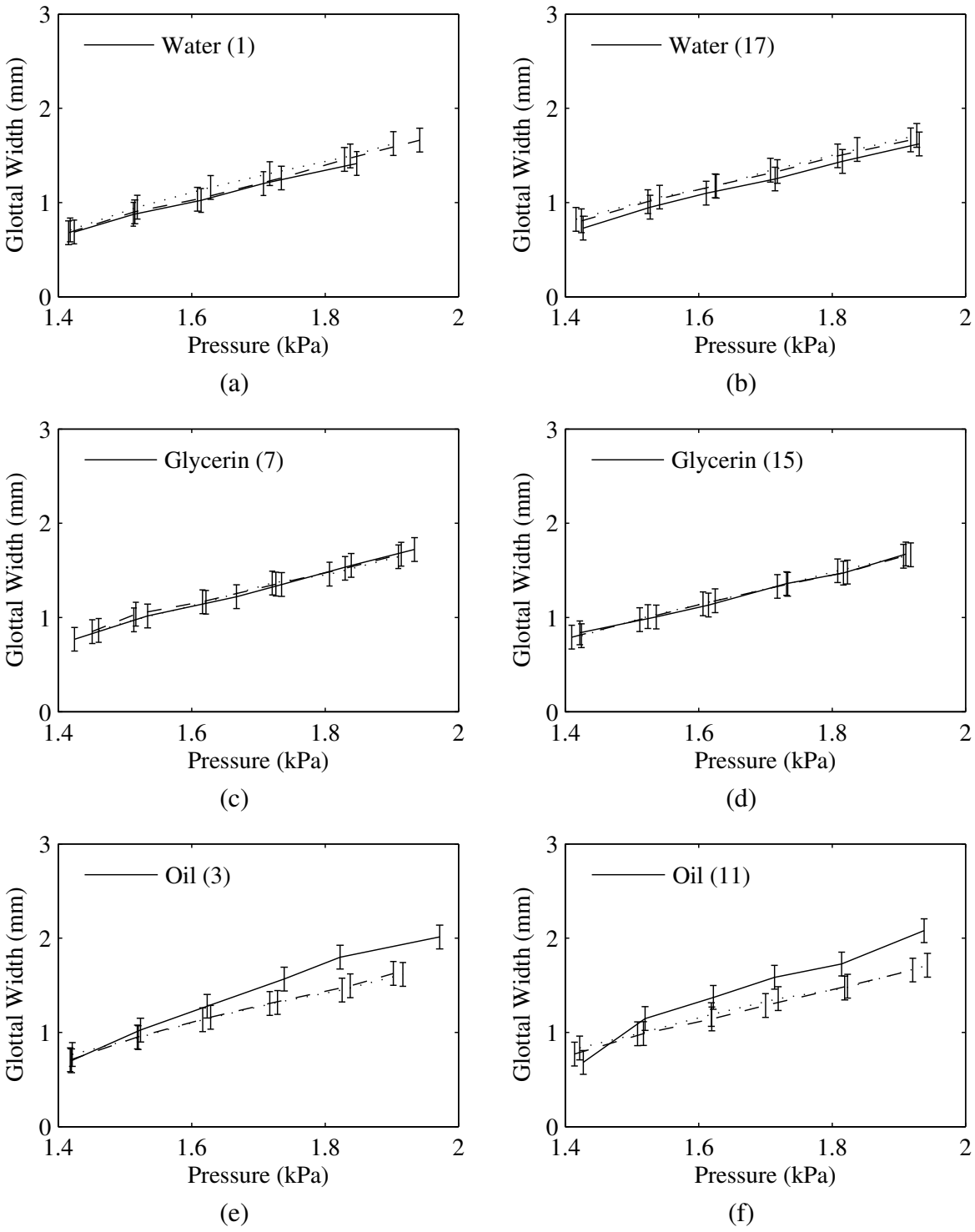

Figure 5.22: Glottal width vs. mean subglottal pressure for water, glycerin, and oil (err < .126 mm – ±6 pixels); (—) fluid case, (- -) dry before, (···) dry after. The number in parenthesis in the legend after the fluid name is the test case number which corresponds to the data given in Appendix B.

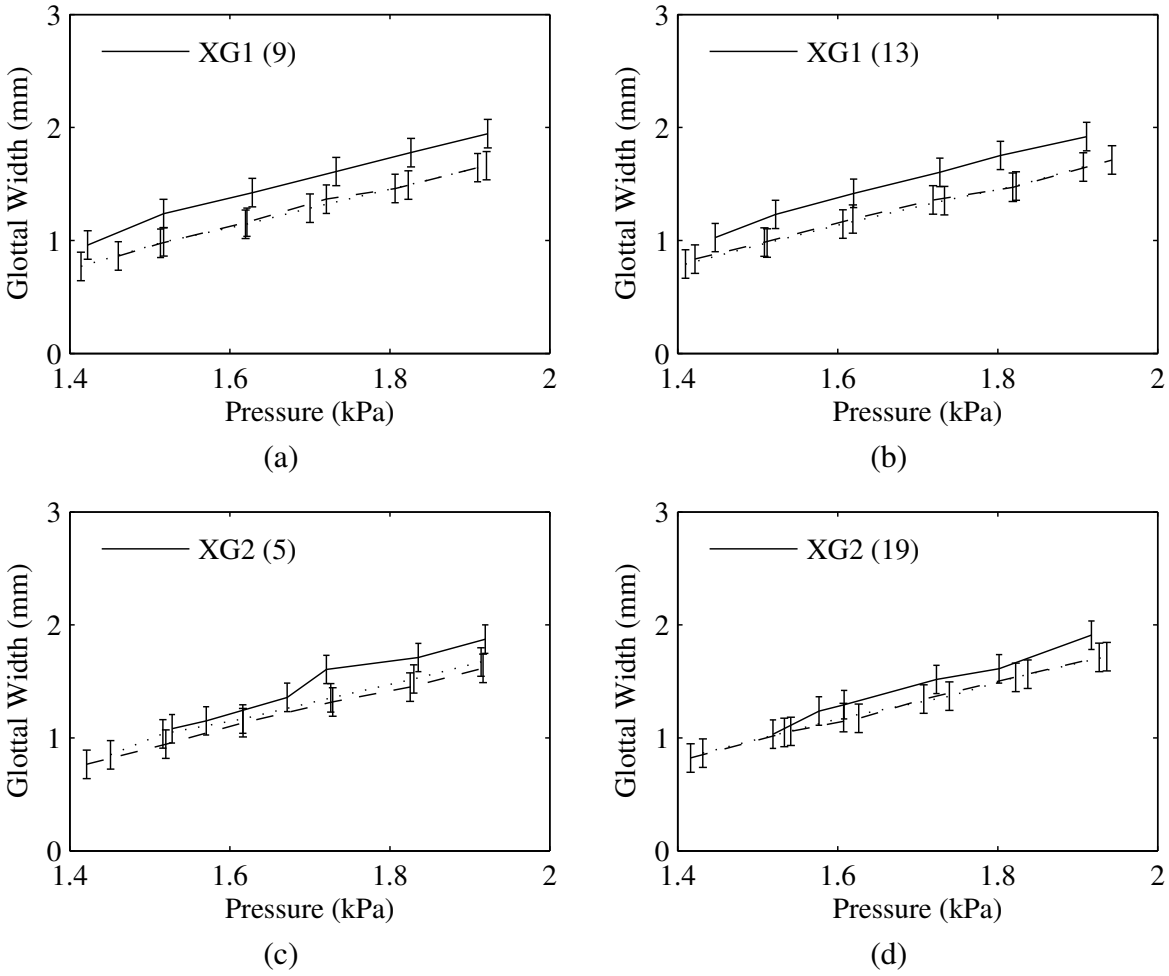

Figure 5.23: Glottal width vs. mean subglottal pressure for XG1 and XG2 (the measurement error was ±6 pixels which corresponds to an distance error of 0.126 mm); (—) fluid case, (- -) dry before, (···) dry after. The number in parenthesis in the legend after the fluid name is the test case number which corresponds to the data given in Appendix B.

In summary, it was concluded that the notable changes in peak-to-peak force, airflow rate, fundamental frequency, A_1/A_0 ratio, A_2/A_0 ratio, glottal width, and peak glottal area were either negligible or attributable to the protrusion of the foam insert in the faceplate. A surge of fluid into the glottis increased the peak-to-peak force as much as a sudden reduction of glottal area would. There was no significant change in the shape of the normalized glottal area waveform. However, onset and offset pressures were significantly increased or decreased for oil, glycerin, and XG2. Therefore, it is possible that the application of the fluid layer affects the operation of the model

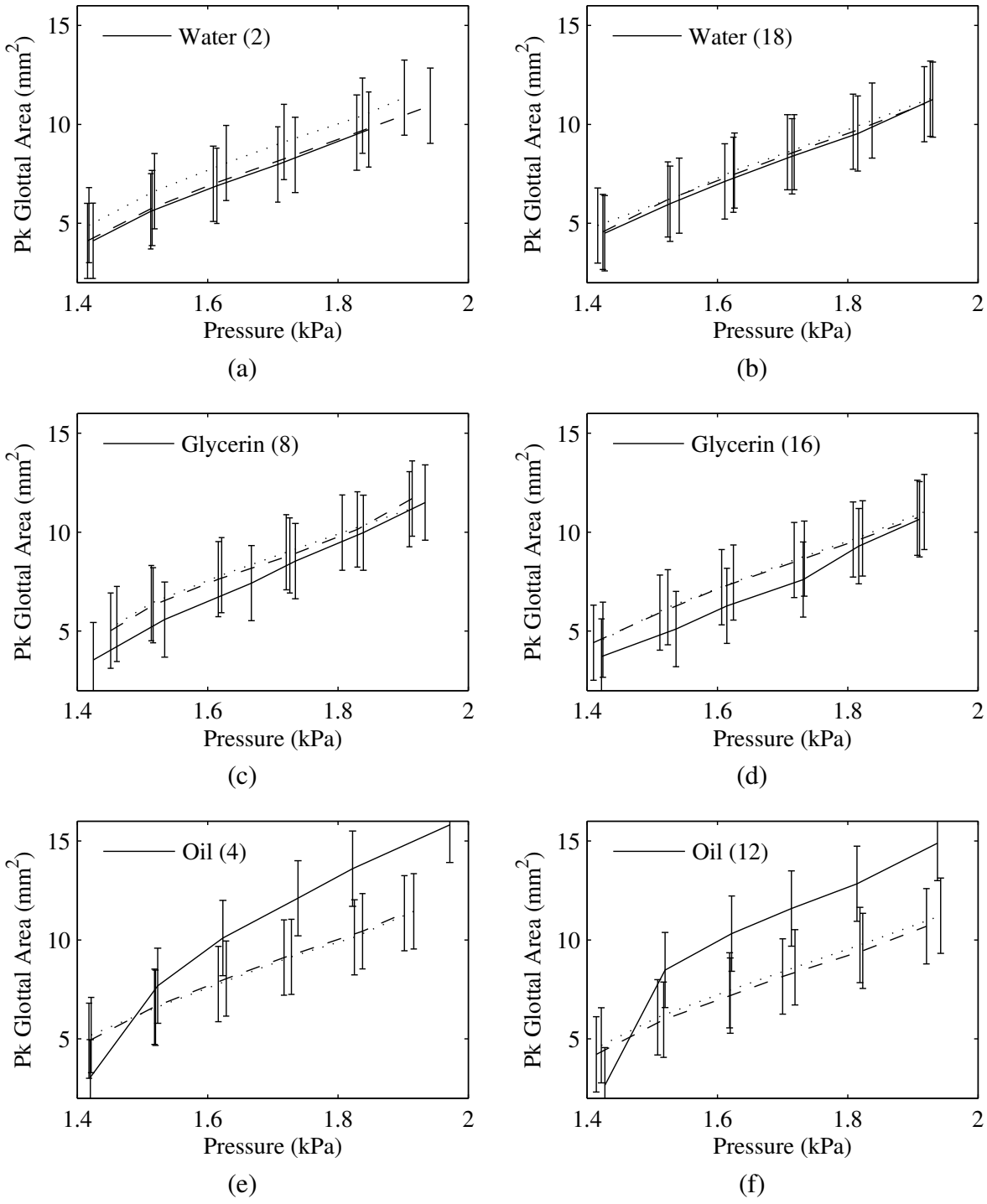

Figure 5.24: Glottal width vs. mean subglottal pressure (err < .126 mm – ±6 pixels); (—) fluid case, (- -) dry before, (···) dry after. The number in parenthesis in the legend after the fluid name is the test case number which corresponds to the data given in Appendix B.

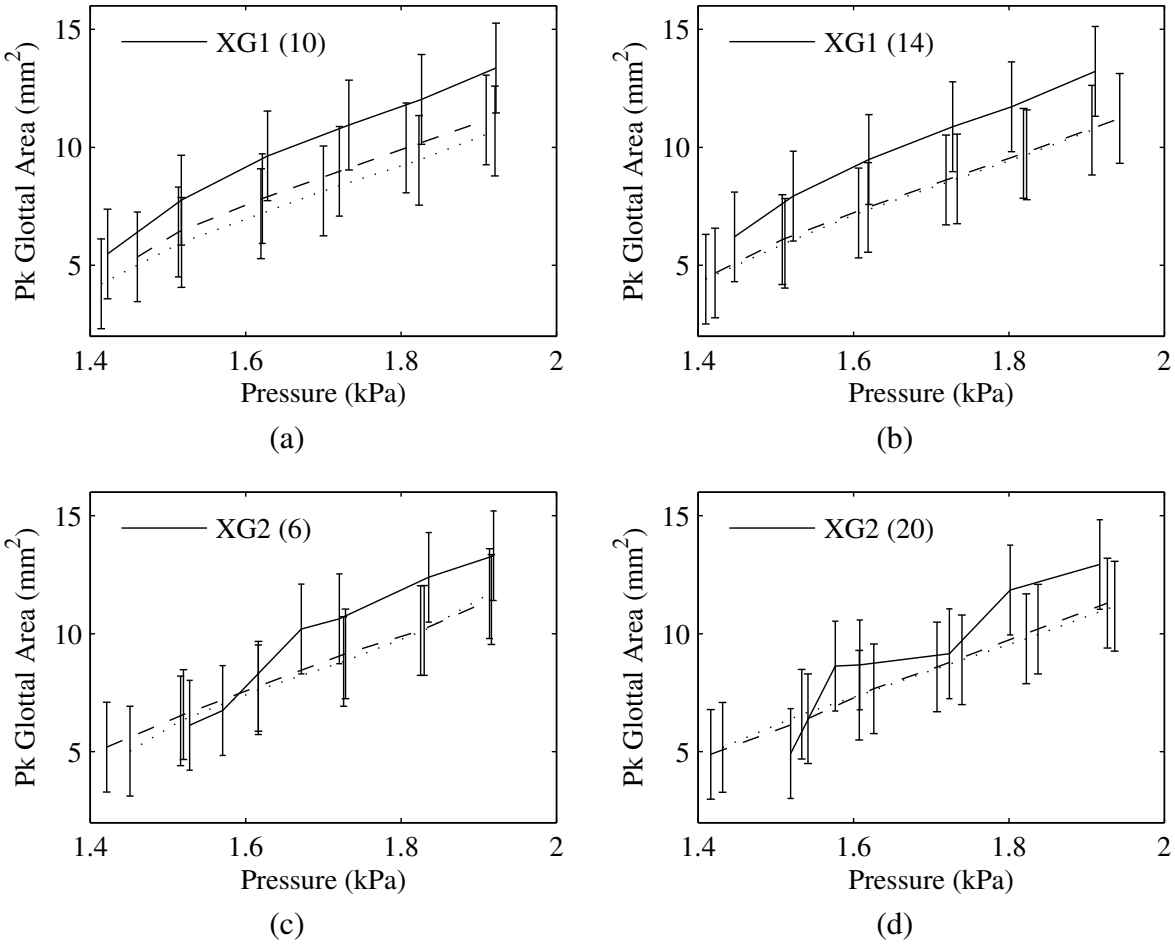

Figure 5.25: Glottal width vs. mean subglottal pressure (err < .126 mm – ±6 pixels); (—) fluid case, (- -) dry before, (···) dry after. The number in parenthesis in the legend after the fluid name is the test case number which corresponds to the data given in Appendix B.

(and potentially actual human vocal fold operation) insomuch as the layer of fluid reduces the glottal area and significantly onset and offset threshold pressures.

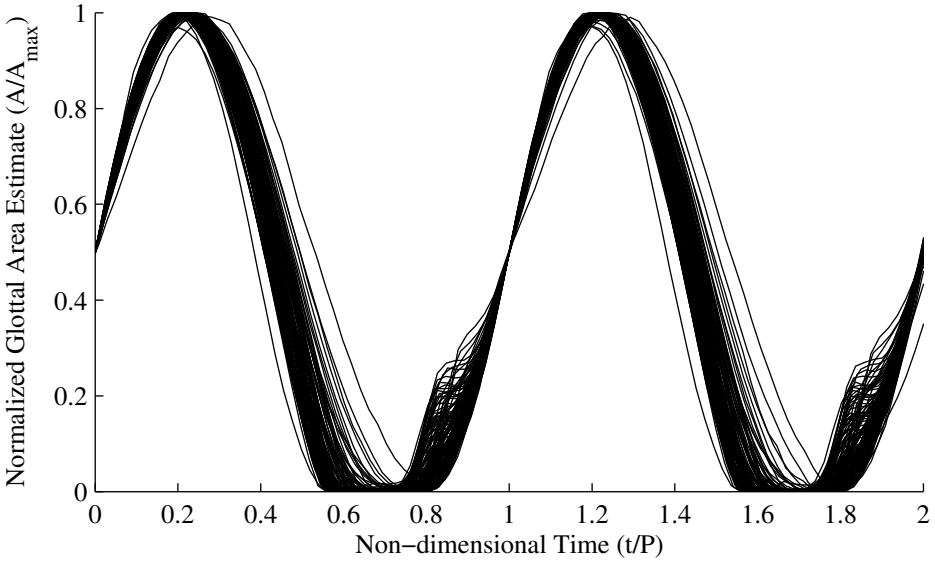

Figure 5.26: Normalized glottal areas.

Table 5.1: Summary of onset and offset pressure data (see Appendix A for additional fluid properties).

Fluid	**Mean Onset (kPa)**	**% Change**	**Mean Offset (kPa)**	**% Change**
Dry	1.33	–	1.30	–
Water	1.37	2.49%	1.33	2.07%
Oil	1.42	6.25%	1.38	5.92%
Glycerin	1.26	-5.39%	1.24	-4.48%
XG1	1.37	2.87%	1.34	2.84%
XG2	1.51	13.38%	1.48	13.62%

CHAPTER 6. CONCLUSIONS

6.1 Summary

The research described in this thesis consisted of three components which progressively led toward the study of the effects of the liquid layer on real human vocal fold operation. First, the experimental measurement of oscillatory and colliding/separating flows of Newtonian and non-Newtonian fluids in a parallel plate geometry was performed. The experimental results were compared with existing analytical equations for squeezing flow (roughly similar to the squeezing flow that may exist on vocal folds during phonation). The Newtonian fluids were found to be in agreement with the equation within measurement uncertainty which led the way to its use as an analytical model of the liquid layer. The analytical equation for non-Newtonian squeeze flow was found to have a constitutive model that did not match the measured fluid properties of the non-Newtonian fluid used. An analysis of the discrepancies was made and the experimental data obtained is summarized in this thesis for future use.

A well-known lumped parameter model of vocal fold dynamics was modified to incorporate the analytical Newtonian squeeze flow equation and preliminary results indicated that the presence of fluid and its thickness may affect vocal fold operation. This step confirmed, preliminarily, that the fluid layer may have the potential to influence vocal function. A more realistic model was needed to further investigate the effects the liquid layer may have on voice. Lacking a numerical model for a non-Newtonian fluid approximating the human mucus, a synthetic model was chosen for experimental testing.

An experimental investigation was performed using Newtonian and non-Newtonian fluids on a synthetic vocal fold test setup. Onset and offset phonation threshold pressures were observed to increase or decrease depending on the fluid applied by up to 13%. Other changes were observed, but could not be completely attributed to the presence of fluid in the present test setup. They were suspected to be a result of the protruding of the porous foam inserts approximately 0.35 mm beyond

the faceplate surface and consequently reducing the space between the surface of the porous foam and the vocal fold model.

6.2 Contributions

The primary contributions of this research can be summarized as follows:

- Experimental data was acquired which further validates the analytical expression used in this work for modeling the squeeze flow of a Newtonian fluid confined between parallel, axisymmetric disks,
- A body of experimental data regarding oscillatory squeeze flow of Newtonian and a shear-thinning, thixotropic, non-Newtonian, viscoelastic fluid were taken,
- A preliminary investigation of the effects of the presence and depth of fluid on the vocal folds was made using a lumped parameter numerical model,
- An experimental investigation was made using a synthetic vocal fold model and different Newtonian and non-Newtonian fluids,
- Developed test setup for measuring contact force with and without liquid layer application.

6.3 Future Work

The work described herein may be further extended in the following ways. A more precise model of the vocal folds (e.g., more masses, three-dimensional, or finite element) could be used in place of the highly simplified two-mass model used herein. This could potentially be a fluid-structure interaction finite element model which incorporates an additional boundary loading on the vocal fold surface based on a squeeze flow equation. One area that may yield important discoveries would be the investigation of the high-speed rupture of liquid bridges which may occur during human phonation.

Fluid spinnability, or the ability of a fluid to stretch into long slender strings was not investigated herein. However, it may be a significant factor influencing the physics of liquid bridges during phonation of actual vocal folds.

The hydrophobicity of the synthetic silicone vocal fold models was likely a factor influencing the flow physics during the testing described herein. The liquid layer on human vocal folds coats the entire surface of the vocal fold; however, on the model, the fluid did not coat the entire surface. Thus, using a material with hydrophilic properties which more closely resemble real vocal folds may yield different results than those reported. One way to accomplish this could be to use excised larynges and perform the same or similar testing as described herein. Another approach would be to use a silicone-wetting fluid.

The research described in this thesis is based on the measurement of film force. It could be potentially more valuable to be able to measure the pressure distribution of a fluid film or the impact of a vocal fold, synthetic or excised. To the best of the author's knowledge, no methods or sensors exist presently which are capable of measuring pressure at the high temporal and high spatial resolutions required. However, it is highly likely that such capabilities would be invaluable in many endeavors. Two potential methods that could result in such a capability are 1) a miniature piezoelectric array and 2) a thin layer of flexible, particle-laden, material affixed to a rigid, transparent substrate. The idea for the second case would be to use high-speed video to record the displacement of the the particles distributed throughout the flexible film during the application of pressure. Then, based on the particle displacements, derive the pressure-field that was applied and caused the measured displacements.

REFERENCES

[1] National Institute of Deafness and Other Communication Disorders, 2010. Statistics on voice, speech, and language `http://www.nidcd.nih.gov/health/statistics/vsl.asp`. 1

[2] Scherer, R. C., and Titze, I. R., 1982. "Vocal fold contact stress during phonation." *J. Acoust. Soc. Am.,* **71**(S1), pp. S55–S55. 1, 5

[3] Jiang, J. J., and Titze, I. R., 1994. "Measurement of vocal fold intraglottal pressure and impact stress." *J. Voice,* **8**(2), pp. 132–144. 1, 5

[4] Titze, I. R., 1994. "Mechanical stress in phonation." *J. Voice,* **8**(2), pp. 99–105. 1, 5

[5] Hess, M. M., Verdolini, K., Bierhals, W., Mansmann, U., and Gross, M., 1998. "Endolaryngeal contact pressures." *J. Voice,* **12**(1), pp. 50–67. 1, 5

[6] Verdolini, K., Chan, R., Titze, I. R., Hess, M., and Bierhals, W., 1998. "Correspondence of electroglottographic closed quotient to vocal fold impact stress in excised canine larynges." *J. Voice,* **12**(4), pp. 415–423. 1

[7] Verdolini, K., Hess, M. M., Titze, I. R., Bierhals, W., and Gross, M., 1999. "Investigation of vocal fold impact stress in human subjects." *J. Voice,* **13**(2), pp. 184–202. 1, 5

[8] Jiang, J. J., Shah, A. G., Hess, M. M., Verdolini, K., Banzali, F. M., and Hanson, D. G., 2001. "Vocal fold impact stress analysis." *J. Voice,* **15**(1), pp. 4–14. 1, 5

[9] Sonninena, A., and Laukkanen, A.-M., 2003. "Hypothesis of whiplike motion as a possible traumatizing mechanism in vocal fold vibration." *Folia Phoniatr. Logop.,* **55**(4), pp. 189–198. 1, 5

[10] Johns, M. M., 2003. "Update on the etiology, diagnosis, and treatment of vocal fold nodules, polyps, and cysts." *Otolaryngology & Head and Neck Surgery,* **11**(6), pp. 456–461. 1

[11] Hsiao, T. Y., Liu, C. M., and Lin, K. N., 2002. "Videostrobolaryngoscopy of mucus layer during vocal fold vibration in patients with laryngeal tension-fatigue syndrome." *Ann. Otol. Rhinol. Laryngol.,* **111**, pp. 537–541. 1, 2, 5

[12] Hirano, M., 1974. "Morphological structure of the vocal cord as a vibrator and its variations." *Folia Phoniatr.,* **26**, pp. 89–94. 2

[13] Gray, H., 1913. *Descriptive and Applied*. Philadelphia: Lea and Febiger. ix, 3

[14] Seikel, J. A., King, D. W., and Drumright, D. G., 2000. *Anatomy and Physiology for Speech, Language, and Hearing*., 2nd ed. Singular Publishing Group Inc. ix, 4

[15] Widdicombe, J. H., and Widdicombe, J. G., 1995. "Regulation of human airway surface liquid." *Respir. Phys.,* **99**, pp. 3–12. 2, 4

[16] Widdicombe, J. H., Bastacky, S. J., Wu, D.-Y., and Lee, C., 1997. "Regulation of depth and composition of airway surface liquid." *J. Eur. Respir.,* **10**, pp. 2892–2897. 2

[17] Tarran, R., Button, B., and Boucher, R. C., 2006. "Regulation of normal and cystic fibrosis airway surface liquid volume by phasic shear stress." *Annu. rev. Physiol.,* **68**, pp. 543–561. 2, 4

[18] Rahmoune, H., and Shepherd, K. L., 1995. "State of airway surface liquid on guinea pig trachea." *J. Appl. Physiol.,* **78**, pp. 2020–24. 2

[19] Sims, D. E., and Horne, M. M., 1997. "Heterogeneity of the composition and thickness of tracheal mucus in rats." *Am. J. Physiol.,* **273**, pp. L1036–41. 2

[20] Hsiung, M. W., 2004. "Videolaryngostroboscopic observation of mucus layer during vocal cord vibration in patients with vocal nodules before and after surgery." *Acta Oto-laryngol.,* **124**, pp. 186–191. 2, 5

[21] Bonilha, H. S., Aikman, A., Hines, K., and Deliyski, D. D., 2008. "Vocal fold mucus aggregation in vocally normal speakers." *Logopedics Phoniatrics Vocology,* **33**, pp. 136–142. 3, 5, 6

[22] Woodson, G. W., 1999. *The autonomic nervous system and laryngology*., 1 ed., Vol. 74 of *30* Elsevier Science B.V., Amsterdam, The Netherlands. 4, 6

[23] Leydon, C., Sivasankar, M., Falciglia, D. L., Atkins, C., and Fisher, K. V., 2009. "Vocal fold surface hydration: A review." *J. Voice,* **23**(6), pp. 658–665. 4

[24] Titze, I. R., 1994. *Principles of Voice Production*. Prentice Hall, New Jersey. 5

[25] Ayache, S., Ouaknine, M., Dejonkere, P., Prindere, P., and Giovanni, A., 2004. "Experimental study of the effects of surface mucus viscosity on the glottic cycle." *J. Voice,* **18**, pp. 107–115. 5, 6

[26] Roy, N., Tanner, K., Gray, S. D., Blomgren, M., and Fischer, K., 2003. "An evaluation of the effects of three laryngeal lubricants on phonation threshold pressure (ptp)." *J. Voice,* **17**(3), pp. 331–342. 5, 7

[27] Murugappan, S., Boyce, S., Khosla, S., Kelchner, L., and Gutmark, E., 2010. "Acoustic characteristics of phonation in "wet voice" conditions." *J. Acoust. Soc. Am.,* **127**(4), pp. 2578–2589. 5, 7

[28] Gunter, H. E., 2003. "A mechanical model of vocal-fold collision with high spatial and temporal resolution." *J. Acoust. Soc. Am.,* **113**(2), pp. 994–1000. 5

[29] Gunter, H. E., 2004. "Modeling mechanical stresses as a factor in the etiology of benign vocal fold lesions." *J. Biomechanics,* **37**(7), pp. 1119–1124. 5

[30] Gunter, H. E., Howe, R. D., Zeitels, S. M., Kobler, J. B., and Hillman, R. E., 2005. "Measurement of vocal fold collision forces during phonation." *J. Speech Lang. Hear. R.,* **48**, pp. 567–576. 5

[31] Spencer, M., Siegmund, T., and Mongeau, L., 2008. "Determination of superior surface strains and stresses, and vocal fold contact pressure in a synthetic larynx model using digital image correlation." *J. Acoust. Soc. Am.,* **123**, pp. 1089–1103. 5

[32] Tao, C., and Jiang, J. J., 2006. "Simulation of vocal fold impact pressures with a self-oscillating finite-element model." *J. Acoust. Soc. Am.,* **119**, pp. 3987–3994. 5, 7, 8

[33] Tao, C., and Jiang, J. J., 2007. "Mechanical stress during phonation in a self-oscillating finite-element vocal fold model." *J. Biomechanics,* **40**, pp. 2191–2198. 5, 7, 8

[34] Verdolini, K., Titze, I. R., and Druker, D. G., 1990. "Changes in phonation threshold pressure with induced conditions of hydration." *J. Voice,* **4**, pp. 142–151. 6

[35] Hemler, R. J. B., Wieneke, G. H., and Dejonckere, P. H., 1997. "The effect of relative humidity of inhaled air on acoustic parameters of voice in normal subjects." *J. Voice,* **11**(3), pp. 395–300. 6

[36] Jiang, J. J., Ng, J., and Hanson, D., 1999. "The effects of dehydration on phonation in excised canine larynges." *J. Voice,* **13**, pp. 15–59. 6

[37] Jiang, J. J., Verdolini, K., Aquino, B., Ng, J., and Hanson, D., 2000. "The effects of rehydration on phonation in excised canine larynges." *J. Voice*, pp. 568–575. 6

[38] Sivasankar, M., and Fisher, K. V., 2002. "Oral breathing increases pth and vocal effort by superficial drying of vocal fold mucosa." *J. Voice,* **16**, pp. 172–181. 6

[39] Sataloff, R. T., Hawkshaw, M., and Rosen, D. C., 1997. *Professional Voice: The Science and Art of Clinical Care*. Singular Publishing Group, Inc. 6

[40] Sataloff, R. T., Hawkshaw, M., and Rosen, D. C., 1995. *Manual of Voice Treatment: Pediatrics through Geriatrics*. Singular Publishing Group, Inc. 6

[41] Sataloff, R. T., Spiegel, J. R., Hawkshaw, M. J., and Heuer, R. J., 1994. *Professional Voice Users: Obtaining the History*. Thieme Medical Publishers, Inc., New York, New York. 6

[42] Verdolini, K., Min, Y., Titze, I. R., Lemke, J., Brown, K., van Mersbergen, M., Jiang, J. J., and Fisher, K., 2002. "Biological mechanisms underlying voice changes due to dehydration." *J. Speech Lang. Hear. R.,* **45**, pp. 268–281. 6

[43] Sivasankar, M., and Fisher, K. V., 2003. "Oral breathing challenges in participants with vocal attrition." *J. Speech Lang. Hear. R.,* **46**, pp. 1416–1427. 6

[44] King, M., and Macklem, P. T., 1977. "Rheological properties of microliter quantities of normal mucus." *J. Acoust. Soc. Am.,* **42**(6), pp. 797–802. 7, 54

[45] Flanagan, J. L., and Landgraf, L., 1968. "Self-oscillating source for vocal-tract synthesizers." *IEEE Trans. Audio Electroacoust.,* **AU-16**, pp. 57–64. 7

[46] Ishizaka, K., and Flanagan, J. L., 1972. "Synthesis of voiced sounds from a two-mass model of the vocal cords." *Bell Syst. Tech. J.,* **51**, pp. 1233–1268. 7, 57

[47] Story, B. H., and Titze, I. R., 1995. "Voice simulation with body-cover model of the vocal folds." *J. Acoust. Soc. Am.,* **97**, pp. 1249–1260. 7

[48] Titze, I. R., 1974. "The human vocal cords: A mathematical model - part ii." *Phonetica,* **21**, pp. 1–21. 7

[49] Yang, A., Lohscheller, J., Berry, D. A., Becker, S., Eysholdt, U., Voigt, D., and Dollinger, M., 2010. "Biomechanical modeling of the three-dimensional aspects of human vocal fold dynamics." *J. Acoust. Soc. Am.,* **127**(2), pp. 1014–1031. 7

[50] Alipour, F., Berry, D. A., and Titze, I. R., 2000. "A finite-element model of vocal-fold vibration." *J. Acoust. Soc. Am.,* **108**, pp. 3003–3012. 7

[51] Thomson, S. L., Mongeau, L., and Frankel, S. H., 2005. "Aerodynamic transfer of energy to the vocal folds." *J. Acoust. Soc. Am.,* **118**(3), pp. 1689–1700. 7, 8, 63

[52] Tropea, C., Yarin, A. L., and Foss, J. F., eds., 2007. *Springer Handbook of Experimental Fluid Mechanics*. Springer-Verlag. ix, 11, 13, 14, 15, 16, 17

[53] Constantinescu, V. N., 1970. "On the influence of inertia forces in turbulent and laminar self-acting films." *J. Lub. Tech.,* **92**, pp. 473–481. 18

[54] Hashimoto, H., 1994. "Viscoelastic squeeze film characteristics with inertia effects between two parallel circular plates under sinusoidal motion." *J. Trib.,* **116**, pp. 161–166. 20

[55] Leider, P. J., 1974. "Squeezing flow between parallel disks ii. experimental results." *Ind. Eng. Chem., Fundam.,* **13**(4), pp. 342–346. 28

[56] Esmonde, H., See, H., and Swain, M. V., 2009. "Cavitation in an oscillatory squeeze film rheometer." *Meas. Sci. Technol.,* **20**, p. 075404. 28

[57] Parkins, D. W., and Stanley, W. T., 1982. "Characteristics of an oil squeeze film." *J. Lub. Tech.,* **104**, pp. 497–503. 28

[58] Field, J. S., Swain, M. V., and Phan-Thien, N., 1996. "An experimental investigation of the use of random squeezing to determine the complex modulus of viscoelastic fluids." *J. Non-Newtonian Fluid Mech.,* **65**, pp. 177–194. 28

[59] Kuhn, E. C., and Yates, C. C., 1964. "Fluid inertia effects on the film pressure between axially oscillating parallel circular plates." *ASLE Transactions,* **7**, pp. 299–303. 48

[60] Maeda, S., 1982. "A digital simulation method of the vocal-tract system." *Speech Communication,* **1**, pp. 199–229. 57

[61] Zhang, J. J. J. Y., and Stern, J., 2001. "Modeling of chaotic vibrations in symmetric vocal folds." *J. Acoust. Soc. Am.,* **110**, pp. 2120–2128. 57

[62] Lous, N. J. C., Hofmans, G. C. J., Veldhuis, R. N. J., and Hirschberg, A., 1998. "A symmetrical two-mass vocal-fold model coupled to vocal tract and trachea, with application to prosthesis design." *Acta Acustica united with Acustica,* **16**, pp. 1135–1150. 57

[63] Mergell, P., and andIngo R. Titze, H. H., 2000. "Irregular vocal-fold vibrationhigh-speed observation and modeling." *J. Acoust. Soc. Am.,* **108**, pp. 2996–3002. 57

[64] Hans von Leden, M., 1986. "Voice problems in entertainers." *West J Med,* **144**, pp. 99–101. 84

APPENDIX A. RHEOLOGY

A.1 Newtonian Fluids

Table A.1: Newtonian fluid properties.

Fluid	Dynamic Viscosity Range (Pa·s)	Density (kg/m^3)
Olive Oil	0.035 - 0.075	900
90% Glycerin-Distilled Water	0.100 - 0.325	1201
Distilled Water	0.00112	999

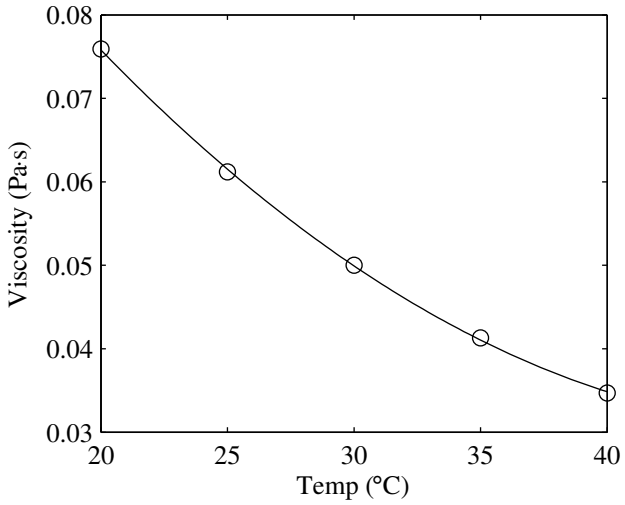

Figure A.1: Change in viscosity of olive oil with temperature. The circles indicate the viscosity measurements taken on the rheometer, the line indicates the quadratic polynomial curve fit used. There is less than 0.7% error between the curve fit and the measured data.

The data is fit over the temperature range shown in Fig. A.1 by the curve

$$V = 5.39E^{-5}T^2 - 5.2803E^{-3}T + 0.15983$$

where T is temperature in degrees Celsius, and V is viscosity in *Pa·s*. The uncertainty in the measurement of temperature is ±2.2°C. This corresponds to an error in calculated viscosity of less than 9.1% over the measured range (20-40 °C).

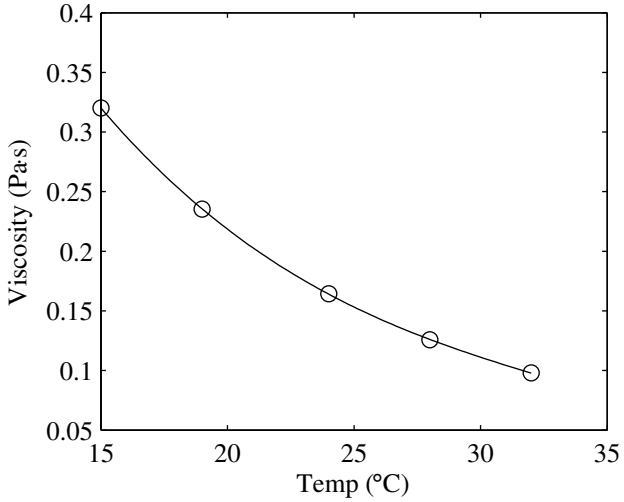

Figure A.2: Change in viscosity of 90%-wt glycerin-water mixture with temperature. The circles indicate the viscosity measurements taken on the rheometer, the line indicates the cubic polynomial curve fit used. There is less than 0.2% error between the curve fit and the measured data.

The data is fit over the temperature range shown in Fig. A.2 by the curve

$$V = -1.738723E^{-5}T^3 + 1.768068E^{-3}T^2 - 6.61077E^{-2}T + 0.9725754$$

where T is temperature in degrees Celsius, and V is viscosity in Pa·s. The uncertainty in the measurement of temperature is estimated to be ±2.2°C. This corresponds to an error in calculated viscosity of less than 17.1% over the measured range (15-32 °C).

A.2 Non-Newtonian Fluids

A.2.1 Fluids Used for Oscillatory Squeeze Flow Testing and Collision and Separation Testing

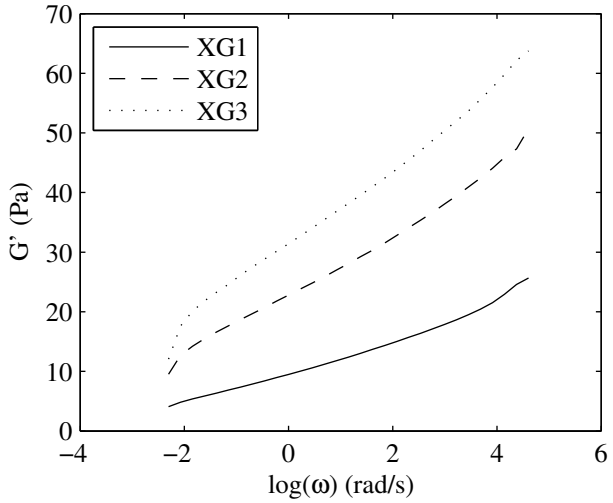

Figure A.3: Elastic moduli, G', for XG1, XG2, and XG3.

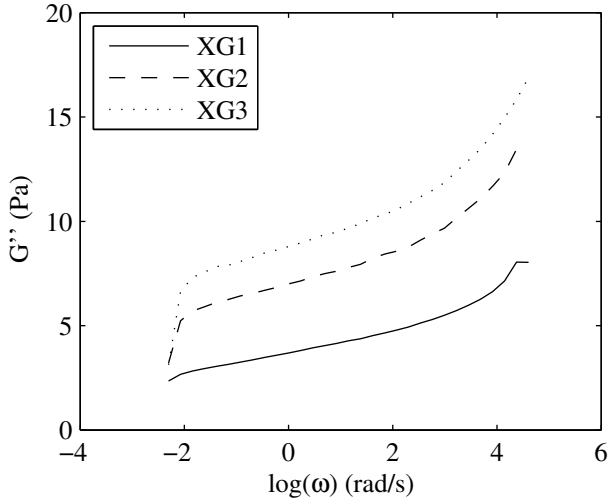

Figure A.4: Viscous moduli, G'', for XG1, XG2, and XG3.

A.2.2 Fluids Used in Hemilarynx Testing

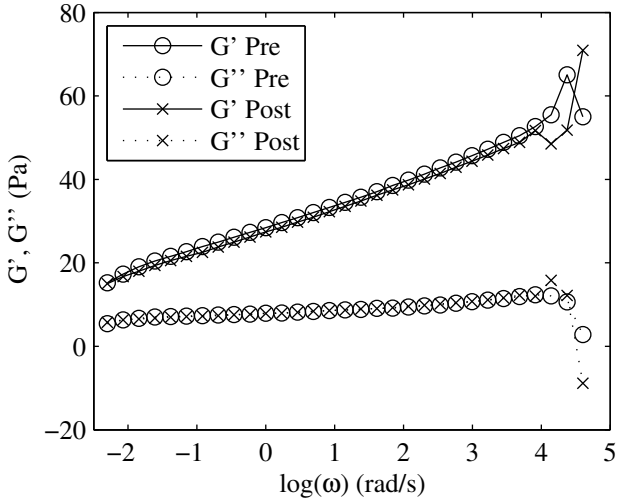

Figure A.5: Comparison of XG1 fluid properties G' and G'' before and after measurements were taken. Only small changes are seen between the two data sets. A change of less than 1.5% average, 6.3% max was observed in G' (neglecting the three highest frequency data points). A change of less than 3.5% average and 5.7% max was observed in G'' (neglecting the three highest frequency data points).

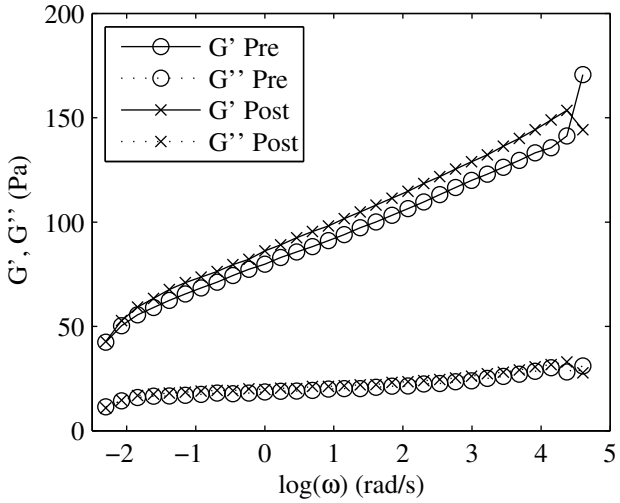

Figure A.6: Comparison of XG2 fluid properties G' and G'' before and after measurements were taken. Only small changes are seen between the two data sets. A change of less than 7.6% average, 11.1% max was observed in G' (neglecting the three highest frequency data points). A change of less than 8.3% average and 7.4% max was observed in G'' (neglecting the three highest frequency data points).

APPENDIX B. SUMMARY OF EXPERIMENTAL DATA

B.1 Nomenclature for Experimental Data

h_0	Mean film thickness
h_{pk}	Peak measured film thickness or film thickness amplitude
F_{pk}	Peak measured force or force amplitude
δ	Phase difference
μ	Fluid dynamic viscosity
SSE	Sum of squared error between curve-fit and measured data
v_0	Initial velocity or initial rate of change of film thickness
v_{pk}	Peak velocity or peak rate of change of film thickness
$t_{vel\,pk}$	Time at which v_{pk} occurs

B.2 Oscillatory Squeeze Flow Data

B.2.1 Newtonian Fluids

Table B.1: Summary of experimental data for glycerin under oscillatory squeeze flow conditions

Data Set #	Freq. (Hz)	h_0 (μm)	h_{pk} (μm)	F_{pk} (N)	δ (ms)	δ (deg)	Temp (°C)	μ (Pa·s)	SSE
1	20.0	98.9	0.9	1.989	7.315	146.4	20.3	0.214	4.94E-12
2	20.0	98.0	1.7	3.932	7.579	151.4	20.3	0.214	8.73E-12
3	20.0	105.6	7.6	15.707	7.205	144.1	20.3	0.214	6.38E-10
4	20.0	62.7	0.6	7.873	1.559	31.2	20.9	0.205	8.25E-12
5	19.9	53.7	0.5	9.821	1.172	23.4	21.0	0.203	1.12E-11
6	20.0	46.2	0.5	11.758	0.452	9.0	21.0	0.204	1.04E-11
7	39.9	100.9	0.7	3.416	2.599	103.8	22.1	0.187	3.91E-12

Data Set #	Freq. (Hz)	h_0 (μm)	h_{pk} (μm)	F_{pk} (N)	δ (ms)	δ (deg)	Temp (°C)	μ (Pa·s)	SSE
8	40.0	99.9	1.3	6.829	2.665	106.6	22.1	0.187	5.49E-12
9	40.0	103.6	2.7	13.652	2.572	103.0	22.1	0.188	1.69E-11
10	40.0	104.3	3.3	16.843	2.833	113.3	22.1	0.187	2.95E-11
11	39.9	60.5	0.7	16.753	1.050	41.9	22.2	0.186	8.59E-12
12	59.9	55.4	0.4	15.874	15.882	951.1	22.4	0.184	6.11E-12
13	60.0	125.4	0.9	4.040	1.812	108.7	22.5	0.182	1.73E-12
14	60.0	125.8	1.7	8.060	1.747	104.8	22.5	0.182	1.89E-12
15	60.0	128.6	2.7	12.058	1.816	109.0	22.5	0.182	2.44E-12
16	60.0	124.9	3.2	16.002	1.714	102.8	22.3	0.185	7.09E-12
17	60.0	102.4	1.7	15.931	1.011	60.6	22.6	0.181	4.96E-12
18	60.0	103.6	2.1	19.804	1.038	62.3	22.5	0.183	5.96E-12
19	60.0	99.0	1.9	19.699	0.955	57.3	22.8	0.179	5.04E-12
20	80.0	96.9	1.0	18.707	0.083	6.7	22.7	0.180	2.67E-12
21	80.0	101.7	1.5	22.354	0.103	8.3	22.7	0.179	6.21E-12
22	80.0	101.5	1.8	25.705	0.260	20.8	23.2	0.174	8.48E-12
23	100.0	98.3	1.0	24.482	-0.490	-48.9	23.4	0.171	3.30E-12
24	100.0	103.4	1.4	27.764	-0.343	-34.3	23.7	0.167	6.29E-12
25	10.0	245.0	4.6	0.425	16.943	169.4	23.8	0.166	3.44E-11
26	10.0	250.7	9.7	0.834	16.258	162.5	23.9	0.165	4.67E-10
27	20.0	249.3	4.8	0.871	9.171	183.3	23.9	0.165	2.27E-11
28	20.0	248.0	9.3	1.727	9.000	180.0	23.9	0.165	2.57E-10
29	20.0	245.2	17.7	3.432	8.611	172.2	23.8	0.166	2.59E-9
30	40.0	248.0	8.5	3.307	4.233	169.3	23.8	0.166	6.03E-11
31	40.0	249.7	4.4	1.674	4.298	171.9	23.8	0.166	1.40E-11
32	40.0	248.3	16.9	6.606	4.107	164.3	23.8	0.167	9.58E-10
33	60.0	247.3	10.2	6.275	2.427	145.6	23.7	0.167	6.35E-11
34	60.0	247.7	5.1	3.147	2.515	150.9	23.7	0.167	6.68E-12
35	60.0	252.4	21.2	12.486	2.325	139.5	18.9	0.237	1.21E-9
36	80.0	252.6	14.4	11.848	1.588	127.0	18.5	0.245	1.25E-10
37	80.0	246.6	6.8	5.995	1.659	132.7	16.4	0.288	1.04E-11
38	100.0	246.5	5.0	5.730	1.102	110.1	16.1	0.294	1.06E-12
39	100.0	246.1	4.9	5.736	1.079	108.0	23.5	0.170	3.00E-12
40	100.0	247.5	9.5	11.385	0.995	99.5	23.5	0.170	2.61E-12
41	120.0	244.7	5.3	10.958	0.172	20.7	23.5	0.170	8.62E-12
42	120.0	248.6	3.2	5.500	0.459	55.1	23.5	0.170	5.12E-12

Table B.2: Summary of experimental data for oil under oscillatory squeeze flow conditions

Data Set #	Freq. (Hz)	h_0 (μm)	h_{pk} (μm)	F_{pk} (N)	δ (ms)	δ (deg)	Temp (°C)	μ (Pa·s)	SSE
1	5.0	100.5	1.8	0.248	21.697	108.4	23.6	0.065	2.05E-11
2	5.0	99.0	3.7	0.513	22.768	113.9	23.8	0.065	8.77E-11
3	5.0	99.6	7.8	1.067	21.815	109.1	23.8	0.065	1.12E-9
4	5.0	99.8	15.7	2.165	19.307	96.5	23.7	0.065	1.54E-8
5	5.0	102.7	29.5	4.081	14.293	71.5	23.8	0.065	1.77E-7
6	5.0	113.8	52.0	6.852	7.277	36.4	23.8	0.065	1.42E-6
7	5.0	133.5	76.7	8.581	2.141	10.7	23.8	0.065	5.05E-6
8	10.0	101.7	1.1	0.333	16.003	159.9	23.7	0.065	1.24E-11
9	10.0	100.3	2.1	0.661	15.860	158.5	23.9	0.064	1.65E-11
10	10.0	99.7	4.1	1.312	15.935	159.3	23.9	0.064	1.02E-10
11	10.0	99.5	8.2	2.621	15.369	153.6	23.9	0.065	1.36E-9
12	10.0	100.6	15.5	4.904	13.985	139.8	23.9	0.064	1.61E-8
13	10.0	110.0	29.9	8.176	11.662	116.6	23.9	0.064	1.85E-7
14	10.0	105.3	32.5	10.186	10.955	109.6	23.9	0.064	2.78E-7
15	10.0	172.3	101.3	14.189	3.642	36.4	24.0	0.064	1.17E-5
16	20.0	99.0	1.1	0.684	8.882	177.6	24.2	0.064	7.04E-12
17	20.0	99.4	2.1	1.366	8.845	176.9	24.2	0.064	9.87E-12
18	20.0	98.0	4.0	2.718	8.639	172.8	24.2	0.064	5.82E-11
19	20.0	99.0	8.1	5.439	8.458	169.2	24.2	0.064	6.48E-10
20	20.0	103.0	17.2	10.818	7.738	154.8	24.2	0.064	1.13E-8
21	30.0	99.6	1.3	1.345	5.695	170.8	24.2	0.063	5.46E-12
22	30.0	100.2	2.7	2.682	5.813	174.4	24.3	0.063	7.69E-12
23	30.0	100.7	5.4	5.354	5.725	171.8	24.1	0.064	1.03E-10
24	30.0	105.0	12.0	10.635	5.535	166.1	24.4	0.063	1.59E-9
25	40.0	98.0	1.8	2.615	3.929	157.1	24.6	0.063	6.84E-12
26	40.0	99.4	3.8	5.222	4.015	160.6	24.6	0.063	2.44E-11
27	40.0	102.2	8.1	10.435	3.881	155.3	24.6	0.063	3.56E-10
28	40.0	106.7	10.6	12.184	3.819	152.8	24.6	0.062	9.17E-10
29	50.0	101.0	2.4	3.974	3.010	150.5	24.6	0.062	8.90E-11
30	50.0	100.8	4.8	7.936	2.997	149.9	24.6	0.062	3.22E-11
31	50.0	104.1	7.7	11.877	2.907	145.4	24.7	0.062	2.11E-10
32	50.0	103.5	10.0	15.738	2.806	140.3	24.7	0.062	5.94E-10
33	50.0	107.4	13.6	19.566	2.727	136.3	24.7	0.062	1.77E-9
34	50.0	102.9	12.2	19.495	2.774	138.7	24.7	0.062	1.21E-9
35	60.0	99.9	2.0	3.864	2.520	151.2	25.1	0.061	1.90E-12
36	60.0	100.3	3.9	7.716	2.464	147.8	25.0	0.061	8.57E-12
37	60.0	108.6	7.4	11.491	2.983	179.0	25.0	0.061	4.90E-12
38	60.0	101.2	6.3	11.499	3.274	196.4	25.1	0.061	4.91E-11
39	70.0	98.8	1.6	3.781	2.054	143.8	25.2	0.061	1.45E-12

Data Set #	Freq. (Hz)	h_0 (μm)	h_{pk} (μm)	F_{pk} (N)	δ (ms)	δ (deg)	Temp (°C)	μ (Pa·s)	SSE
40	70.0	100.8	3.3	7.537	2.085	145.9	25.2	0.061	3.85E-10
41	70.0	102.6	5.1	11.261	2.078	145.5	25.2	0.061	4.57E-12
42	70.0	100.5	5.1	11.612	2.210	154.7	25.2	0.061	2.70E-12
43	70.0	100.8	5.3	11.965	2.279	159.5	25.2	0.061	2.91E-12
44	70.0	102.9	5.8	12.315	2.394	167.6	25.1	0.061	8.50E-12
45	70.0	101.6	5.9	12.673	2.572	180.1	25.3	0.061	3.46E-11
46	70.0	96.6	5.4	13.041	2.684	187.9	25.3	0.061	6.53E-11
47	70.0	96.0	5.5	13.380	2.726	190.8	25.1	0.061	1.80E-10
48	80.0	101.1	2.8	7.320	2.221	177.7	25.4	0.061	1.60E-11
49	80.0	94.2	3.5	10.946	2.294	183.5	25.4	0.060	1.04E-10
50	80.0	99.0	2.7	7.320	2.338	187.0	25.4	0.060	2.21E-11
51	80.0	43.0	2.8	10.979	3.270	261.6	25.6	0.060	1.88E-12
52	80.0	43.1	2.8	10.976	3.286	262.9	25.6	0.060	2.57E-12
53	90.0	96.5	3.6	10.676	2.193	197.3	25.6	0.060	6.39E-11
54	90.0	85.1	3.7	11.389	2.674	240.7	25.6	0.060	3.69E-11
55	90.0	57.5	3.5	11.412	2.745	247.1	25.6	0.060	4.14E-12
56	100.1	36.7	1.2	10.502	2.023	202.4	25.7	0.060	1.27E-12
57	100.0	59.5	1.5	10.490	2.194	219.5	25.7	0.060	1.71E-12
58	100.0	68.7	1.5	10.490	2.101	210.1	25.7	0.060	3.62E-12
59	100.0	83.1	1.9	10.455	1.748	174.8	25.7	0.060	6.08E-12
60	100.0	93.2	2.3	10.461	1.567	156.7	25.6	0.060	4.64E-12
61	100.0	99.1	2.6	10.450	1.494	149.4	25.6	0.060	5.66E-12
62	109.9	31.2	0.4	3.466	1.668	183.3	25.7	0.060	9.47E-13
63	110.0	37.6	1.2	10.310	1.575	173.3	25.7	0.060	7.31E-13
64	110.0	54.9	1.7	10.291	1.865	205.2	25.7	0.060	1.41E-12
65	110.0	70.2	1.9	10.280	1.915	210.7	25.5	0.060	1.35E-12
66	110.0	81.9	2.0	10.265	1.754	193.0	25.7	0.060	2.65E-12
67	110.0	93.5	2.2	10.254	1.591	175.1	25.7	0.060	7.59E-12
68	120.0	34.8	1.1	10.086	1.206	144.7	25.7	0.060	6.83E-13
69	120.0	49.9	1.6	10.084	1.382	165.9	25.8	0.060	9.97E-13
70	120.0	75.4	2.1	10.078	1.562	187.5	25.7	0.060	2.97E-12
71	120.0	79.6	2.1	10.074	1.501	180.2	25.8	0.060	2.76E-12
72	120.0	90.4	2.3	10.067	1.543	185.1	25.8	0.060	4.27E-12
73	120.0	98.8	2.7	10.053	1.571	188.5	25.8	0.060	1.26E-11
74	130.0	36.6	1.2	9.907	0.983	127.7	25.9	0.059	6.28E-13
75	130.0	45.1	1.5	9.902	0.945	122.8	25.4	0.061	7.05E-13
76	130.1	73.1	2.4	9.897	1.194	155.3	25.9	0.059	3.34E-12
77	130.0	85.2	2.6	9.889	1.319	171.5	25.9	0.059	5.49E-12
78	130.0	88.8	2.8	9.889	1.346	175.0	25.9	0.059	8.22E-12
79	130.0	99.3	3.1	9.873	1.370	178.1	25.9	0.059	1.36E-11
80	130.0	40.5	1.9	13.147	0.931	121.1	26.0	0.059	8.88E-13
81	130.1	50.5	2.3	13.133	1.028	133.6	25.9	0.059	2.78E-12
82	130.1	62.5	2.8	13.109	1.115	145.1	25.8	0.059	5.34E-12

Data Set #	Freq. (Hz)	h_0 (μm)	h_{pk} (μm)	F_{pk} (N)	δ (ms)	δ (deg)	Temp (°C)	μ (Pa·s)	SSE
83	90.0	38.0	2.3	11.438	2.160	194.4	26.0	0.059	2.51E-12
84	90.0	45.1	2.5	11.391	2.255	203.1	26.1	0.059	2.98E-12
85	90.1	57.2	2.8	11.379	2.354	212.1	26.1	0.059	7.07E-12
86	90.3	69.1	3.3	11.369	2.261	204.3	26.1	0.059	3.84E-11
87	89.0	80.4	4.5	11.380	2.600	231.4	26.1	0.059	4.02E-10
88	80.0	252.4	4.0	1.035	1.703	136.2	22.8	0.068	6.61E-12
89	80.0	254.3	9.6	2.438	1.766	141.2	22.8	0.068	3.95E-11
90	80.0	246.9	19.4	5.330	1.743	139.4	22.8	0.067	6.32E-10
91	40.0	250.7	9.7	1.227	4.450	178.0	22.8	0.067	1.38E-10
92	40.0	247.6	20.1	2.627	4.288	171.5	22.8	0.067	1.92E-9
93	40.0	257.7	49.0	5.424	3.771	150.8	22.9	0.067	1.07E-7
94	40.0	262.2	65.7	6.841	3.554	142.1	22.8	0.067	3.63E-7
95	30.0	248.7	9.8	0.905	6.111	183.3	23.0	0.067	1.88E-10
96	30.0	250.1	20.9	1.918	5.935	178.0	22.9	0.067	2.78E-9
97	30.0	256.3	42.6	3.570	5.263	157.9	22.9	0.067	7.83E-8
98	30.0	262.5	64.3	5.042	4.503	135.1	23.1	0.067	4.42E-7
99	20.0	250.7	9.6	0.590	9.246	184.8	23.0	0.067	4.10E-10
100	20.0	252.1	19.1	1.153	8.971	179.4	23.0	0.067	3.25E-9
101	20.0	254.7	39.1	2.272	8.082	161.6	23.1	0.067	7.31E-8
102	20.0	266.2	66.3	3.425	6.208	124.2	23.1	0.067	7.35E-7
103	20.0	253.4	9.7	0.579	9.316	186.2	23.1	0.067	4.05E-10
104	20.0	251.2	18.7	1.154	8.856	177.1	23.1	0.067	2.44E-9
105	20.0	257.6	40.2	2.268	7.998	159.9	23.0	0.067	1.64E-7
106	20.0	264.1	64.6	3.434	6.296	125.9	23.1	0.067	6.70E-7
107	10.0	251.9	9.4	0.296	16.659	166.5	23.0	0.067	5.81E-10
108	10.0	250.8	18.7	0.569	15.959	159.5	23.0	0.067	6.97E-9
109	10.0	256.5	39.5	1.116	14.254	142.5	23.0	0.067	1.35E-7
110	10.0	264.4	64.2	1.683	10.340	103.4	23.0	0.067	1.17E-6
111	5.0	251.3	10.0	0.155	23.691	118.2	23.0	0.067	5.75E-10
112	5.0	249.6	20.1	0.275	24.193	120.8	23.0	0.067	5.39E-9
113	5.0	253.5	41.2	0.531	20.576	102.9	23.1	0.067	1.19E-7
114	5.0	259.0	61.8	0.760	13.917	69.6	23.1	0.067	7.78E-7
115	50.0	247.6	10.1	1.625	3.296	164.8	23.1	0.067	1.01E-10
116	50.0	248.6	19.9	3.177	3.271	163.6	23.1	0.067	1.17E-9
117	50.0	257.5	45.4	6.287	2.995	149.8	23.1	0.067	5.92E-8
118	50.0	261.3	56.3	7.312	2.944	147.2	23.2	0.066	1.48E-7
119	60.0	248.6	9.7	1.864	2.627	157.6	23.2	0.066	4.72E-11
120	60.0	248.9	19.2	3.701	2.571	154.3	23.2	0.066	8.82E-10
121	60.0	251.4	41.3	7.309	2.477	148.6	23.1	0.066	2.56E-8
122	60.0	261.1	59.9	8.173	2.688	161.3	23.4	0.066	9.92E-8
123	70.0	257.0	40.8	7.535	2.167	151.7	23.4	0.066	2.77E-8
124	70.0	252.9	17.9	3.858	2.133	149.3	23.5	0.066	4.99E-10
125	70.0	249.7	9.0	2.002	2.158	151.0	23.5	0.066	5.13E-11

Data Set #	Freq. (Hz)	h_0 (μm)	h_{pk} (μm)	F_{pk} (N)	δ (ms)	δ (deg)	Temp (°C)	μ (Pa·s)	SSE
126	90.0	250.5	9.6	2.831	1.417	127.5	23.5	0.066	2.68E-11
127	90.0	247.6	18.5	5.619	1.409	126.8	23.5	0.065	4.36E-10
128	90.0	257.1	39.8	10.903	1.434	129.0	23.6	0.065	8.17E-9
129	100.0	251.6	18.2	5.860	1.232	123.2	23.6	0.065	2.40E-10
130	100.0	249.4	9.0	2.942	1.235	123.5	23.6	0.065	2.23E-11
131	110.0	251.5	8.6	3.116	1.034	113.8	23.6	0.065	1.30E-11
132	110.0	250.4	17.3	6.322	1.023	112.5	23.7	0.065	1.69E-10
133	120.0	252.8	10.9	4.312	0.833	100.0	23.7	0.065	1.89E-11
134	130.0	248.8	9.7	5.096	0.749	97.3	23.7	0.065	2.59E-11
135	130.0	251.7	9.5	5.019	0.850	110.5	23.7	0.065	1.24E-11
136	130.0	243.6	11.4	6.743	0.897	116.6	23.7	0.065	4.20E-11
137	20.0	501.1	10.4	0.089	8.517	170.3	26.1	0.059	6.73E-9
138	20.0	499.6	21.8	0.164	9.492	189.8	26.1	0.059	5.00E-10
139	20.0	500.2	43.9	0.313	9.262	185.2	26.1	0.059	7.36E-9
140	40.0	500.5	9.8	0.150	4.359	174.3	26.1	0.059	2.19E-11
141	40.0	501.2	20.1	0.290	4.321	172.8	26.1	0.059	1.30E-10
142	40.0	499.2	39.9	0.568	4.349	174.0	26.1	0.059	1.25E-9
143	60.0	501.9	11.0	0.245	2.438	146.2	26.1	0.059	1.75E-11
144	60.0	500.9	21.4	0.470	2.450	147.0	26.1	0.059	2.18E-11
145	60.0	495.3	41.4	0.928	2.483	149.0	26.0	0.059	4.46E-10
146	80.0	502.0	10.6	0.325	1.562	125.0	26.0	0.059	7.17E-12
147	80.0	499.2	20.9	0.641	1.543	123.5	26.0	0.059	1.77E-11
148	80.0	500.2	41.8	1.278	1.585	126.8	26.0	0.059	2.18E-10
149	100.0	504.1	10.5	0.408	0.985	98.5	26.0	0.059	1.22E-11
150	100.0	498.8	20.5	0.809	0.974	97.4	25.9	0.059	6.24E-11
151	100.0	502.7	40.6	1.621	0.963	96.3	26.0	0.059	7.64E-11
152	120.0	497.5	10.2	0.522	0.555	66.6	25.9	0.059	1.91E-11
153	120.0	500.9	19.9	1.020	0.523	62.7	26.0	0.059	8.93E-12
154	120.0	502.2	39.8	2.064	0.507	60.8	26.0	0.059	5.78E-11
155	20.0	126.6	4.6	0.990	10.522	210.4	25.9	0.059	2.43E-11
156	20.0	124.8	9.5	2.081	10.358	207.1	25.9	0.059	3.73E-10
157	20.0	122.2	17.4	3.991	9.828	196.6	25.9	0.059	4.72E-9
158	40.0	124.0	3.9	1.903	4.342	173.7	25.9	0.059	1.25E-11
159	40.0	129.6	8.9	3.852	4.243	169.7	25.7	0.060	1.73E-10
160	40.0	128.7	19.5	8.749	3.898	155.9	26.0	0.059	4.57E-9
161	60.0	127.4	11.2	7.740	2.424	145.4	26.0	0.059	3.12E-10
162	60.0	127.8	5.8	3.866	2.523	151.3	26.2	0.058	2.88E-11
163	80.0	120.1	5.0	5.287	1.695	135.6	26.3	0.058	6.38E-12
164	80.0	120.1	9.9	10.517	1.648	131.8	26.3	0.058	8.93E-11
165	80.0	251.1	5.4	0.971	1.642	131.4	26.2	0.059	9.22E-12
166	80.0	247.4	9.7	1.770	1.693	135.4	26.2	0.059	4.21E-11
167	80.0	239.5	19.0	3.762	1.702	136.2	26.2	0.058	4.59E-10
168	40.0	247.4	12.0	1.057	4.317	172.6	26.2	0.059	2.63E-10

Data Set #	Freq. (Hz)	h_0 (μm)	h_{pk} (μm)	F_{pk} (N)	δ (ms)	δ (deg)	Temp (°C)	μ (Pa·s)	SSE
169	40.0	248.7	24.3	2.097	4.258	170.3	26.2	0.059	3.28E-9
170	40.0	252.5	49.3	4.199	4.045	161.8	26.2	0.059	5.83E-8
171	40.0	260.9	66.4	5.254	3.911	156.5	26.2	0.059	2.13E-7
172	30.0	250.6	8.5	0.533	6.050	181.4	26.2	0.059	1.13E-10
173	30.0	249.1	18.6	1.199	5.846	175.3	26.2	0.059	1.60E-9
174	30.0	255.0	43.6	2.685	5.619	168.6	26.2	0.059	4.28E-8
175	30.0	258.0	64.1	3.907	5.078	152.3	26.1	0.059	2.50E-7
176	20.0	252.4	11.8	0.494	9.040	180.7	26.1	0.059	5.80E-10
177	20.0	252.1	46.6	1.977	8.143	162.9	26.1	0.059	8.79E-8
178	20.0	268.9	74.7	2.768	6.769	135.4	25.8	0.059	7.18E-7
179	10.0	251.8	10.0	0.213	16.210	162.0	26.1	0.059	8.39E-10
180	10.0	251.6	20.4	0.422	15.324	153.2	26.1	0.059	6.23E-9
181	10.0	254.0	42.0	0.857	14.246	142.4	26.1	0.059	1.03E-7
182	10.0	263.6	67.8	1.293	11.702	117.0	26.1	0.059	8.72E-7
183	5.0	249.3	8.9	0.094	21.297	106.3	26.1	0.059	3.06E-10
184	5.0	250.2	18.8	0.179	22.188	111.0	26.1	0.059	3.73E-9
185	5.0	250.4	38.6	0.359	19.918	99.5	26.1	0.059	6.52E-8
186	5.0	257.4	60.4	0.537	17.310	86.5	26.0	0.059	3.95E-7
187	50.0	248.9	9.4	1.036	3.237	161.8	26.0	0.059	6.05E-11
188	50.0	249.9	19.0	2.031	3.250	162.5	25.8	0.059	7.18E-10
189	50.0	253.1	38.6	4.054	3.198	159.9	25.8	0.059	1.37E-8
190	50.0	257.7	60.5	6.074	3.132	156.6	26.1	0.059	1.03E-7
191	60.0	249.7	9.9	1.296	2.507	150.4	26.1	0.059	5.28E-11
192	60.0	253.0	20.3	2.551	2.571	154.2	26.1	0.059	6.32E-10
193	60.0	253.0	40.4	5.088	2.589	155.3	25.9	0.059	1.04E-8
194	60.0	255.8	60.4	7.334	2.661	159.7	26.2	0.059	6.16E-8
195	70.0	250.4	9.4	1.450	2.108	147.5	26.0	0.059	3.82E-11
196	70.0	251.4	19.0	2.860	2.129	149.0	26.1	0.059	4.48E-10
197	70.0	255.5	39.1	5.645	2.174	152.2	26.1	0.059	8.87E-9
198	70.0	260.0	61.0	8.463	2.334	163.4	26.2	0.058	6.39E-8
199	90.0	250.4	10.2	2.068	1.361	122.5	26.2	0.058	4.55E-11
200	90.0	252.5	20.8	4.099	1.407	126.6	26.2	0.059	4.19E-10
201	90.0	254.2	42.1	8.099	1.514	136.3	26.3	0.058	8.60E-9
202	90.0	252.6	54.3	10.603	1.627	146.4	26.5	0.058	2.52E-8
203	100.0	251.5	9.8	2.200	1.171	117.2	26.4	0.058	1.65E-11
204	100.0	253.8	19.8	4.323	1.194	119.4	26.5	0.058	2.76E-10
205	100.0	250.1	37.6	8.594	1.236	123.6	26.4	0.058	3.62E-9
206	110.0	248.0	10.0	2.576	1.020	112.1	26.5	0.058	3.52E-11
207	110.0	252.3	20.5	5.024	1.045	114.9	26.5	0.058	2.80E-10
208	120.0	252.4	9.5	2.807	0.692	83.0	26.4	0.058	1.51E-11
209	120.0	249.8	18.8	5.559	0.722	86.6	26.5	0.058	1.32E-10
210	130.0	248.1	8.7	3.358	0.906	117.7	26.3	0.058	1.19E-11
211	130.0	252.5	19.3	6.565	0.867	112.7	26.4	0.058	2.20E-10

Table B.3: Summary of experimental data for water under oscillatory squeeze flow conditions

Data Set #	Freq. (Hz)	h_0 (μm)	h_{pk} (μm)	F_{pk} (N)	δ (ms)	δ (deg)	Temp (°C)	μ (Pa·s)	SSE
1	19.9	92.2	1.1	0.032	11.113	221.7	24.3	0.001	1.85E-11
2	20.0	89.5	2.6	0.056	8.811	176.1	24.3	0.001	3.68E-11
3	20.0	87.4	5.3	0.104	8.416	168.2	24.3	0.001	1.87E-10
4	20.0	85.8	7.7	0.158	8.072	161.3	24.3	0.001	5.48E-10
5	20.0	84.3	9.9	0.209	7.893	157.8	24.3	0.001	1.14E-9
6	20.0	82.7	11.9	0.263	7.587	151.7	24.3	0.001	2.68E-9
7	20.0	81.9	14.0	0.314	7.417	148.3	24.3	0.001	4.93E-9
8	20.0	79.5	15.2	0.370	7.279	145.6	24.2	0.001	7.81E-9
9	20.0	70.2	11.5	0.386	7.487	149.7	24.3	0.001	3.89E-9
10	20.0	50.2	5.3	0.414	8.159	163.2	24.3	0.001	3.68E-10
11	20.0	42.3	3.5	0.415	8.492	169.8	24.4	0.001	1.28E-10
12	20.0	31.8	1.8	0.426	8.864	177.2	24.3	0.001	2.53E-11
13	40.0	25.0	1.0	0.830	3.950	158.0	24.4	0.001	5.04E-12
14	40.0	32.5	1.9	0.822	4.094	163.8	24.4	0.001	8.34E-12
15	40.0	37.6	2.6	0.811	4.028	161.1	24.4	0.001	2.91E-11
16	40.0	45.9	4.1	0.794	3.994	159.7	24.4	0.001	6.99E-11
17	40.0	51.5	5.4	0.780	3.881	155.2	24.4	0.001	1.57E-10
18	40.0	60.9	8.0	0.750	3.720	148.8	24.4	0.001	4.19E-10
19	40.0	71.1	11.3	0.720	3.542	141.7	24.4	0.001	9.68E-10
20	40.0	82.0	15.1	0.683	3.275	131.0	24.4	0.001	1.97E-9
21	40.0	92.4	19.0	0.648	3.024	120.9	24.4	0.001	4.75E-8
22	40.0	102.6	22.8	0.616	2.703	108.1	24.2	0.001	3.49E-9
23	60.0	102.7	13.5	0.567	1.246	74.7	24.4	0.001	1.08E-10
24	60.0	90.9	11.5	0.620	1.566	93.9	24.4	0.001	1.31E-10
25	60.0	80.9	9.4	0.667	1.734	104.0	24.4	0.001	1.23E-10
26	60.0	71.0	7.3	0.710	1.964	117.9	24.4	0.001	9.07E-11
27	60.0	60.9	5.3	0.750	2.111	126.7	24.4	0.001	4.04E-11
28	60.0	50.7	3.5	0.789	2.197	131.8	24.4	0.001	1.84E-11
29	60.0	38.8	1.9	0.824	2.327	139.6	24.4	0.001	5.39E-12
30	80.0	37.7	1.2	0.785	1.398	111.8	24.4	0.001	1.78E-12
31	80.0	36.9	1.6	1.044	1.468	117.4	24.2	0.001	4.21E-12
32	80.0	49.2	3.0	0.996	1.463	117.0	24.4	0.001	5.42E-12
33	80.0	58.6	4.4	0.949	1.325	106.0	24.4	0.001	1.10E-11
34	80.0	69.3	6.2	0.882	1.189	95.1	24.4	0.001	1.81E-11
35	80.0	77.8	7.5	0.827	1.030	82.4	24.4	0.001	2.07E-11
36	80.0	88.2	9.1	0.753	0.832	66.5	24.4	0.001	2.54E-11
37	80.0	99.4	10.4	0.680	0.635	50.8	24.4	0.001	1.34E-11
38	100.0	94.3	13.5	1.390	0.105	10.5	24.4	0.001	6.99E-11

Data Set #	Freq. (Hz)	h_0 (μm)	h_{pk} (μm)	F_{pk} (N)	δ (ms)	δ (deg)	Temp (°C)	μ (Pa·s)	SSE
39	100.0	84.1	12.0	1.531	0.310	31.0	24.4	0.001	4.52E-11
40	100.0	73.6	9.9	1.685	0.483	48.3	24.5	0.001	6.54E-11
41	100.0	63.3	7.7	1.825	0.682	68.2	24.5	0.001	5.40E-11
42	100.0	53.1	5.6	1.951	0.829	82.9	24.5	0.001	2.94E-11
43	100.0	43.4	3.6	2.057	0.916	91.6	24.5	0.001	1.08E-11
44	100.0	31.6	1.8	2.148	1.022	102.2	24.4	0.001	1.54E-12
45	100.0	29.5	2.1	3.004	0.948	94.8	24.5	0.001	6.24E-11

B.2.2 Non-Newtonian Fluids

Table B.4: Summary of experimental data for XG1 under oscillatory squeeze flow conditions

Data Set #	Freq. (Hz)	h_0 (μm)	h_{pk} (μm)	F_{pk} (N)	δ (ms)	δ (deg)	Temp (°C)	SSE
1	5.0	100.3	4.6	0.576	31.032	155.0	21.3	4.65E-10
2	5.0	96.5	11.8	0.759	26.018	130.1	21.3	6.61E-9
3	5.0	92.8	19.4	0.942	21.956	109.7	21.0	3.94E-8
4	10.0	110.1	17.6	1.075	16.177	161.7	21.1	1.77E-8
5	10.0	110.8	9.9	0.871	17.885	178.8	21.3	2.98E-9
6	10.0	100.9	34.6	1.730	12.572	125.7	21.3	2.99E-7
7	20.0	99.0	19.2	1.722	8.506	170.1	21.3	1.33E-8
8	20.0	107.1	3.9	0.910	10.959	219.2	21.3	1.26E-10
9	40.0	101.1	9.8	1.641	4.450	178.0	21.3	4.20E-10
10	40.0	88.2	15.3	2.428	4.057	162.3	21.3	2.63E-9
11	40.0	74.8	17.1	3.289	3.843	153.7	21.1	5.60E-9
12	60.0	99.7	5.5	1.569	2.875	172.5	21.3	3.15E-11
13	60.0	100.6	20.9	2.842	2.437	146.2	21.3	2.64E-9
14	60.0	78.1	12.0	3.052	2.430	145.8	21.3	5.63E-10
15	80.0	81.7	9.0	2.855	1.697	135.8	21.3	1.37E-10
16	80.0	108.1	16.6	2.588	1.704	136.3	21.3	5.29E-10
17	80.0	95.0	17.9	3.320	1.632	130.6	21.3	1.06E-9
18	100.0	105.1	15.5	3.015	1.082	108.2	21.3	2.14E-10
19	100.0	75.4	14.7	4.900	0.988	98.8	21.3	7.76E-10
20	100.0	85.0	18.3	4.726	0.993	99.3	21.3	8.23E-10
21	120.0	102.7	16.4	4.148	0.358	43.0	21.3	2.59E-10
22	120.0	140.8	11.1	2.053	0.602	72.2	21.3	2.20E-11

Data Set #	Freq. (Hz)	h_0 (μm)	h_{pk} (μm)	F_{pk} (N)	δ (ms)	δ (deg)	Temp (°C)	SSE
23	120.0	106.5	6.7	2.407	0.578	69.3	21.3	1.56E-11
24	140.0	108.3	5.6	2.286	1.070	149.8	21.1	2.81E-12
25	140.0	101.1	6.9	2.796	0.980	137.2	21.3	5.00E-12
26	140.0	87.8	7.9	3.694	0.948	132.7	21.3	1.13E-11
27	140.0	88.9	10.8	4.386	0.836	117.1	21.3	3.32E-11
28	140.0	113.5	15.3	3.830	0.612	85.7	21.3	4.38E-11
29	140.0	73.6	7.9	4.722	0.963	134.9	21.4	2.41E-11
30	140.0	60.0	5.1	5.022	1.102	154.2	21.1	1.34E-11
31	140.0	48.9	3.2	5.252	1.280	179.1	21.2	5.30E-12
32	120.0	45.8	2.6	5.532	0.139	16.6	21.4	9.11E-12
33	120.0	53.6	4.2	5.379	0.244	29.3	21.4	2.77E-11
34	120.0	61.8	6.2	5.201	0.286	34.3	21.4	7.47E-11
35	120.0	72.4	9.2	4.984	0.345	41.4	21.2	1.57E-10
36	120.0	86.5	13.2	4.729	0.395	47.4	21.4	2.77E-10
37	100.0	85.0	10.0	3.275	1.090	109.0	21.4	1.13E-10
38	100.0	72.6	6.9	3.438	1.067	106.7	21.4	4.54E-11
39	100.0	60.2	4.3	3.597	1.038	103.7	21.4	1.18E-11
40	80.0	57.1	5.6	3.788	1.681	134.4	21.5	3.41E-11
41	80.0	66.0	7.6	3.698	1.625	130.0	21.4	1.09E-10
42	80.0	75.6	10.4	3.578	1.634	130.7	21.5	2.54E-10
43	80.0	86.2	14.0	3.445	1.645	131.6	21.4	5.44E-10
44	60.0	80.1	17.4	3.737	2.335	140.1	21.4	2.33E-9
45	60.0	71.4	13.5	3.837	2.315	138.9	21.5	1.19E-9
46	60.0	62.3	10.0	3.942	2.346	140.7	21.5	5.02E-10
47	60.0	52.4	6.8	4.031	2.384	143.0	21.5	1.73E-10
48	60.0	41.1	4.0	4.119	2.423	145.4	21.2	3.17E-11
49	40.0	41.0	4.3	3.501	4.192	167.7	21.4	7.93E-11
50	40.0	50.9	6.9	3.451	4.135	165.4	21.5	3.15E-10
51	40.0	63.2	11.2	3.375	3.987	159.5	21.5	1.44E-9
52	40.0	73.9	15.9	3.299	3.879	155.2	21.5	4.25E-9
53	40.0	84.9	21.7	3.220	3.811	152.4	21.4	1.13E-8
54	20.0	82.7	11.7	1.775	8.873	177.4	21.3	3.22E-9
55	20.0	66.0	6.2	1.812	9.339	186.7	21.5	5.09E-10
56	20.0	50.8	2.9	1.843	9.609	192.1	21.5	7.96E-11
57	20.0	35.3	1.0	1.862	9.921	198.2	21.5	7.98E-11
58	20.0	216.2	15.4	0.598	11.136	222.7	21.3	1.54E-9
59	20.0	214.5	30.8	0.730	9.904	198.1	21.5	1.51E-8
60	20.0	214.8	4.0	0.461	15.541	311.0	21.5	1.32E-11
61	20.0	181.0	9.0	0.647	11.500	230.0	21.5	4.98E-10
62	20.0	176.2	18.7	0.803	10.076	201.5	21.5	4.60E-9
63	40.0	155.5	5.9	0.839	5.755	230.2	21.5	4.82E-11
64	60.0	155.3	3.6	0.832	3.939	236.3	21.6	6.17E-12
65	60.0	151.7	9.4	1.086	3.153	189.2	21.6	7.63E-11

Data Set #	Freq. (Hz)	h_0 (μm)	h_{pk} (μm)	F_{pk} (N)	δ (ms)	δ (deg)	Temp (°C)	SSE
66	80.0	152.1	6.6	1.069	2.376	190.0	21.6	1.36E-11
67	80.0	149.5	10.8	1.301	2.125	170.0	21.6	5.23E-11
68	100.0	149.9	7.6	1.263	1.528	152.8	21.6	7.72E-12
69	100.0	147.7	10.5	1.479	1.402	140.2	21.4	2.12E-11
70	120.0	148.7	6.5	1.425	0.880	105.6	21.4	4.76E-12
71	120.0	147.2	8.2	1.609	0.788	94.6	21.5	7.77E-12
72	120.0	144.7	9.9	1.823	0.708	85.0	21.6	8.51E-12
73	120.0	141.2	11.5	2.059	0.634	76.1	21.6	1.50E-11
74	120.0	146.6	13.8	2.198	0.537	64.5	21.6	3.49E-11
75	140.0	149.9	10.5	2.008	0.861	120.5	21.4	4.39E-12
76	140.0	148.6	11.7	2.186	0.803	112.5	21.6	6.89E-12
77	140.0	152.7	14.6	2.459	0.638	89.3	21.6	8.79E-12
78	140.0	151.3	16.0	2.651	0.565	79.1	21.6	3.85E-9

Table B.5: Summary of experimental data for XG2 under oscillatory squeeze flow conditions

Data Set #	Freq. (Hz)	h_0 (μm)	h_{pk} (μm)	F_{pk} (N)	δ (ms)	δ (deg)	Temp (°C)	SSE
1	20.0	102.3	11.8	2.558	8.706	174.1	21.6	3.71E-9
2	20.0	106.8	6.2	1.947	9.375	187.5	21.6	4.61E-10
3	20.0	99.6	10.6	2.562	8.784	175.7	21.6	2.69E-9
4	20.0	94.3	11.5	2.886	8.566	171.3	21.6	4.05E-9
5	20.0	75.9	4.9	2.938	8.914	178.2	21.6	3.59E-10
6	20.0	58.2	1.3	2.972	8.762	175.1	21.6	2.76E-11
7	20.0	35.6	1.4	5.953	6.834	136.7	21.6	4.58E-11
8	40.0	100.0	12.3	3.605	3.976	159.0	21.6	1.68E-9
9	40.0	86.3	13.1	4.860	3.773	150.9	21.6	3.07E-9
10	60.0	91.0	9.5	4.544	2.334	140.0	21.6	4.03E-10
11	60.0	103.1	14.4	4.398	2.307	138.4	21.4	1.34E-9
12	80.0	109.0	11.4	4.087	1.598	127.8	21.6	3.64E-10
13	80.0	102.8	11.8	4.634	1.574	125.9	21.6	4.46E-10
14	80.0	134.1	6.9	2.330	1.883	150.7	21.6	3.49E-11
15	100.0	108.9	10.0	4.319	1.031	103.1	21.6	1.40E-10
16	100.0	104.6	9.7	4.596	0.996	99.6	21.6	2.60E-10
17	120.0	110.2	6.6	4.330	0.448	53.7	21.6	5.36E-11
18	120.0	101.4	6.5	5.094	0.368	44.2	21.4	5.89E-11
19	120.0	109.3	9.7	5.355	0.424	50.9	21.5	1.82E-10
20	140.0	100.5	6.2	5.269	1.115	156.1	21.6	1.62E-11
21	140.0	85.5	3.4	5.584	1.301	182.1	21.4	6.31E-12
22	140.0	79.1	2.5	5.722	1.447	202.6	21.6	2.47E-12
23	140.0	72.1	1.6	5.848	1.677	234.7	21.7	1.49E-12

Data Set #	Freq. (Hz)	h_0 (μm)	h_{pk} (μm)	F_{pk} (N)	δ (ms)	δ (deg)	Temp (°C)	SSE
24	120.0	74.8	2.0	6.037	0.106	12.7	21.8	6.65E-12
25	120.0	79.7	2.7	5.941	0.160	19.1	21.7	1.00E-11
26	120.0	86.2	3.9	5.813	0.248	29.7	21.6	2.22E-11
27	120.0	91.6	5.1	5.708	0.318	38.2	21.8	3.94E-11
28	100.0	92.7	9.7	5.926	0.970	97.0	21.8	1.79E-10
29	100.0	97.5	11.2	5.836	0.986	98.6	21.8	2.70E-10
30	100.0	88.9	8.3	6.019	0.970	97.0	21.7	1.11E-10
31	100.0	84.1	6.8	6.108	0.954	95.4	21.9	5.38E-11
32	100.0	78.5	5.3	6.217	0.937	93.7	21.9	1.90E-11
33	100.0	67.4	2.8	6.395	0.915	91.5	21.7	4.09E-12
34	100.0	55.1	1.1	6.513	0.699	69.9	21.9	1.23E-12
35	80.0	50.3	1.3	6.828	1.329	106.3	21.9	2.98E-12
36	80.0	53.9	1.8	6.808	1.428	114.3	22.0	3.81E-12
37	80.0	59.3	2.7	6.758	1.561	124.9	22.0	5.67E-12
38	80.0	64.4	3.7	6.707	1.535	122.8	21.9	1.50E-11
39	80.0	70.0	5.1	6.633	1.545	123.6	22.0	3.55E-11
40	80.0	75.6	6.7	6.548	1.559	124.7	22.0	7.70E-11
41	80.0	80.5	8.3	6.476	1.552	124.1	22.0	1.52E-10
42	80.0	85.2	9.9	6.388	1.534	122.7	22.0	3.00E-10
43	80.0	89.8	11.7	6.310	1.530	122.4	22.1	5.65E-10
44	80.0	94.1	13.5	6.228	1.537	122.9	22.0	8.66E-10
45	60.0	100.7	17.8	5.471	2.243	134.6	22.1	3.18E-9
46	60.0	96.1	15.6	5.532	2.238	134.3	21.9	2.31E-9
47	60.0	129.1	12.3	2.900	2.563	153.8	22.1	4.03E-10
48	60.0	99.8	4.7	3.132	2.692	161.5	21.9	3.57E-11
49	60.0	73.2	6.5	5.825	2.301	138.1	22.1	1.75E-10
50	60.0	68.0	5.0	5.873	2.317	139.0	22.1	6.92E-11
51	60.0	62.1	3.5	5.920	2.321	139.3	22.1	2.45E-11
52	60.0	49.5	1.4	5.998	1.996	119.7	22.2	4.44E-12
53	40.0	44.6	1.8	6.325	3.748	149.9	22.0	1.51E-11
54	40.0	53.1	3.5	6.285	3.877	155.1	22.1	7.29E-11
55	40.0	58.8	5.1	6.260	3.939	157.6	22.2	1.85E-10
56	40.0	64.7	7.1	6.216	3.850	154.0	22.2	5.08E-10
57	40.0	76.3	12.1	6.125	3.722	148.9	22.2	2.80E-9
58	40.0	87.3	18.1	6.021	3.574	143.0	22.1	1.02E-8
59	40.0	99.3	18.5	4.742	3.735	149.4	22.0	8.00E-9
60	40.0	106.9	18.5	4.116	3.859	154.3	22.2	6.72E-9
61	40.0	114.9	17.5	3.504	3.966	158.6	22.2	4.60E-9
62	40.0	124.2	15.7	2.900	4.144	165.8	22.2	2.48E-9

Data Set #	Freq. (Hz)	h_0 (μm)	h_{pk} (μm)	F_{pk} (N)	δ (ms)	δ (deg)	Temp (°C)	SSE
63	40.0	133.6	12.3	2.334	4.372	174.9	22.2	8.81E-10
64	40.0	135.0	12.8	2.326	4.371	174.8	22.2	1.02E-9
65	40.0	154.2	20.2	2.209	4.297	171.9	22.3	3.64E-9
66	40.0	176.3	29.9	2.082	4.303	172.1	22.3	1.08E-8
67	20.0	113.3	15.4	2.523	8.655	173.1	22.2	7.75E-9
68	20.0	103.8	11.2	2.548	8.897	177.9	22.3	2.88E-9
69	20.0	94.2	7.6	2.578	9.056	181.1	22.3	1.02E-9
70	20.0	85.0	4.9	2.602	9.332	186.6	22.3	3.17E-10
71	20.0	75.4	2.8	2.621	9.628	192.5	22.1	8.27E-11
72	20.0	81.3	4.0	2.610	9.459	189.1	22.3	1.91E-10
73	20.0	72.8	2.3	2.631	9.438	188.8	22.3	5.18E-11
74	20.0	46.5	1.3	3.961	8.806	176.0	22.4	2.66E-11
75	21.1	56.5	0.5	2.651	8.419	177.3	22.4	8.21E-11
76	20.0	100.9	9.9	2.561	9.033	180.7	22.4	1.87E-9
77	20.0	146.4	32.7	2.413	8.059	161.2	22.4	7.08E-8
78	20.0	159.7	23.7	1.812	8.920	178.4	22.4	1.71E-8
79	40.0	154.1	19.4	2.219	4.297	171.9	22.4	3.38E-9
80	60.0	158.3	12.4	2.083	2.776	166.6	22.4	2.64E-10
81	60.0	153.4	14.7	2.313	2.694	161.6	22.2	4.94E-10
82	60.0	149.0	16.9	2.557	2.624	157.4	22.4	9.07E-10
83	80.0	153.9	12.2	2.404	1.904	152.3	22.4	1.48E-10
84	80.0	150.3	13.8	2.613	1.843	147.5	22.4	2.70E-10
85	80.0	145.4	14.8	2.850	1.810	144.8	22.4	3.77E-10
86	80.0	144.8	14.7	2.855	1.813	145.0	22.5	3.08E-10
87	80.0	139.7	15.4	3.104	1.776	142.1	22.5	4.73E-10
88	80.0	148.3	18.2	3.011	1.795	143.6	22.3	6.65E-10
89	100.0	156.3	14.4	2.789	1.249	124.9	22.3	1.12E-10
90	100.0	164.2	12.2	2.394	1.315	131.5	22.5	6.32E-11
91	100.0	170.7	9.2	2.037	1.393	139.4	22.5	1.77E-11
92	100.0	160.4	15.4	2.748	1.241	124.1	22.3	1.40E-10
93	120.0	165.0	10.1	2.609	0.738	88.5	22.5	3.09E-11
94	120.0	156.4	8.8	2.708	0.712	85.4	22.4	3.19E-11
95	120.0	149.4	10.1	3.096	0.657	78.8	22.5	4.38E-11
96	120.0	144.7	10.3	3.323	0.618	74.2	22.6	6.79E-11
97	120.0	140.3	10.5	3.547	0.590	70.7	22.5	7.59E-11
98	120.0	141.5	13.0	3.869	0.566	67.9	22.5	1.32E-10
99	120.0	138.3	13.3	4.101	0.564	67.7	22.6	1.54E-10
100	120.0	143.2	3.4	2.400	0.807	96.9	22.6	5.12E-12

Data Set #	Freq. (Hz)	h_0 (μm)	h_{pk} (μm)	F_{pk} (N)	δ (ms)	δ (deg)	Temp (°C)	SSE
101	100.0	140.3	5.9	2.457	1.330	133.0	22.6	1.51E-11
102	80.0	137.1	7.9	2.560	1.915	153.2	22.6	5.53E-11
103	60.0	146.9	15.4	2.584	2.665	159.9	22.6	5.68E-10
104	40.0	162.2	10.5	1.747	4.783	191.3	22.7	3.21E-10
105	20.0	160.7	22.7	1.812	9.010	180.2	22.5	1.46E-8
106	20.0	167.1	7.2	1.267	10.776	215.5	22.7	3.81E-10
107	10.0	167.0	15.0	1.226	18.033	180.3	22.7	8.96E-9
108	10.0	167.8	4.6	0.946	21.379	213.8	22.7	3.23E-10
109	5.0	167.6	8.9	0.804	30.126	150.6	22.7	2.31E-9
110	5.0	188.2	13.5	0.793	30.006	150.1	22.7	5.32E-9

Table B.6: Summary of experimental data for XG3 under oscillatory squeeze flow conditions

Data Set #	Freq. (Hz)	h_0 (μm)	h_{pk} (μm)	F_{pk} (N)	δ (ms)	δ (deg)	Temp (°C)	SSE
1	40.0	113.6	10.1	3.572	4.303	172.1	–	7.01E-10
2	20.0	122.0	5.9	1.916	9.988	199.8	–	3.24E-10
3	20.0	96.2	16.9	3.768	7.981	159.6	–	1.56E-8
4	20.0	112.5	27.2	3.706	7.468	149.4	–	6.98E-8
5	40.0	116.0	15.5	3.476	4.066	162.6	–	2.96E-9
6	40.0	133.6	2.9	1.858	5.453	218.1	–	1.48E-11
7	40.0	133.3	6.7	2.155	4.741	189.6	–	1.55E-10
8	40.0	124.6	12.0	2.797	4.295	171.8	–	1.04E-9
9	60.0	127.5	7.1	2.664	2.703	162.2	–	9.09E-11
10	60.0	122.8	8.6	2.971	2.626	157.5	–	1.59E-10
11	60.0	118.0	9.7	3.285	2.539	152.3	–	2.22E-10
12	60.0	99.8	5.0	3.431	2.632	157.9	–	4.67E-11
13	60.0	95.5	5.4	3.769	2.531	151.9	–	6.39E-11
14	80.0	96.4	3.3	3.606	1.788	143.1	–	7.00E-12
15	80.0	92.7	4.6	4.211	1.684	134.7	–	2.93E-10
16	80.0	86.1	5.1	4.856	1.635	130.8	–	2.69E-11
17	80.0	98.3	8.2	4.705	1.629	130.3	–	1.19E-10
18	80.0	112.0	12.7	4.506	1.644	131.5	–	4.50E-10
19	80.0	125.7	18.0	4.306	1.689	135.1	–	1.17E-9
20	100.0	137.2	16.2	3.917	1.175	117.5	–	3.09E-10
21	100.0	120.0	11.1	4.181	1.125	112.5	–	1.59E-10

Data Set #	Freq. (Hz)	h_0 (μm)	h_{pk} (μm)	F_{pk} (N)	δ (ms)	δ (deg)	Temp (°C)	SSE
22	100.0	104.3	6.9	4.427	1.080	108.0	–	4.38E-11
23	100.0	97.4	7.0	5.033	1.029	102.9	–	5.62E-11
24	100.0	108.0	10.1	4.854	1.080	108.0	–	1.42E-10
25	120.0	113.7	7.5	4.572	0.566	67.9	–	3.59E-11
26	120.0	100.0	4.3	4.826	0.462	55.4	–	1.45E-11
27	120.0	93.2	4.2	5.429	0.425	51.0	–	1.10E-11
28	120.0	87.7	4.1	6.040	0.386	46.3	–	1.14E-11
29	120.0	98.6	6.9	5.812	0.500	60.0	–	4.12E-11
30	120.0	113.0	10.7	5.520	0.610	73.1	–	9.56E-11
31	120.0	133.9	16.7	5.112	0.656	78.7	–	2.60E-10
32	120.0	124.1	15.8	5.759	0.637	76.5	–	3.26E-10
33	120.0	113.8	14.1	6.465	0.606	72.7	–	3.08E-10
34	120.0	128.5	19.1	6.122	0.633	76.0	–	4.88E-10
35	120.0	174.1	32.7	5.080	0.523	62.8	–	5.56E-10
36	120.0	157.9	28.3	5.461	0.560	67.2	–	6.69E-10
37	120.0	138.2	22.2	5.906	0.615	73.8	–	6.30E-10
38	120.0	193.5	26.7	3.674	0.636	76.3	–	1.98E-10
39	120.0	170.7	22.4	4.079	0.670	80.4	–	1.99E-10
40	100.0	146.4	24.3	4.750	1.128	112.8	–	1.13E-9
41	100.0	172.4	33.3	4.324	1.116	111.6	–	1.34E-9
42	100.0	159.7	29.0	4.530	1.129	112.9	–	1.28E-9
43	80.0	164.8	31.3	3.866	1.765	141.2	–	3.35E-9
44	80.0	153.7	26.6	4.009	1.740	139.2	–	2.55E-9
45	80.0	144.3	22.5	4.140	1.723	137.8	–	1.93E-9
46	80.0	135.3	18.8	4.268	1.719	137.5	–	1.28E-9
47	80.0	138.4	20.0	4.223	1.723	137.8	–	1.40E-9
48	80.0	144.2	22.5	4.142	1.736	138.9	–	1.87E-9
49	80.0	163.5	21.3	3.228	1.835	146.8	–	9.69E-10
50	60.0	153.2	26.3	3.542	2.518	151.1	–	4.48E-9
51	60.0	160.5	29.8	3.471	2.538	152.3	–	6.09E-9
52	60.0	165.8	32.3	3.423	2.543	152.6	–	7.42E-9
53	60.0	169.8	34.3	3.385	2.571	154.3	–	8.20E-9
54	60.0	180.3	37.6	3.189	2.616	156.9	–	8.90E-9
55	60.0	171.8	33.2	3.276	2.577	154.6	–	7.08E-9
56	60.0	162.9	28.7	3.358	2.559	153.5	–	5.16E-9
57	60.0	146.2	20.8	3.536	2.529	151.8	–	2.30E-9
58	60.0	137.6	17.1	3.631	2.512	150.7	–	1.37E-9
59	60.0	122.4	11.2	3.796	2.541	152.5	–	4.65E-10
60	60.0	127.5	8.8	3.309	2.656	159.3	–	1.68E-10
61	40.0	130.6	16.7	3.450	4.162	166.5	–	2.97E-9

Data Set #	Freq. (Hz)	h_0 (μm)	h_{pk} (μm)	F_{pk} (N)	δ (ms)	δ (deg)	Temp (°C)	SSE
62	40.0	149.3	25.6	3.315	4.060	162.4	–	1.10E-8
63	40.0	167.3	35.3	3.187	4.045	161.8	–	2.85E-8
64	40.0	160.5	31.2	3.237	4.024	161.0	–	2.03E-8
65	20.0	186.8	33.1	2.103	8.718	174.4	–	4.99E-8
66	20.0	177.7	27.8	2.138	8.819	176.4	–	2.84E-8
67	20.0	156.9	17.5	2.208	9.174	183.5	–	7.66E-9
68	20.0	134.0	8.8	2.279	9.699	194.0	–	1.10E-9
69	20.0	141.5	10.7	2.265	9.599	192.0	–	1.82E-9
70	10.0	142.0	4.5	1.491	19.247	192.5	–	5.08E-10
71	10.0	141.8	11.4	1.846	17.401	174.0	–	5.61E-9
72	10.0	131.6	8.0	1.855	17.781	177.8	–	2.28E-9
73	10.0	116.2	9.3	2.228	16.977	169.7	–	2.75E-8
74	10.0	104.6	5.4	2.244	17.481	174.7	–	1.38E-9
75	10.0	88.3	4.3	2.625	17.258	172.4	–	6.90E-10
76	5.0	84.9	1.6	1.583	27.084	135.3	–	8.82E-11
77	5.0	84.7	3.5	1.896	26.197	130.9	–	4.12E-10
78	5.0	82.5	5.7	2.203	25.135	125.5	–	1.41E-9
79	5.0	88.0	8.2	2.205	24.110	120.5	–	3.74E-9
80	5.0	110.4	21.6	2.198	19.579	97.9	–	7.32E-8
81	5.0	115.0	16.5	1.884	22.402	112.0	–	2.56E-8
82	5.0	144.1	34.9	1.875	18.084	90.4	–	2.54E-7
83	5.0	155.7	41.9	1.872	17.289	86.4	–	4.70E-7
84	5.0	160.1	29.6	1.561	21.207	106.0	–	1.16E-7
85	5.0	162.1	15.0	1.256	26.398	132.0	–	1.09E-8
86	5.0	162.5	4.8	0.955	30.486	152.5	–	5.32E-10

B.3 Collision & Separation

B.3.1 Newtonian Fluids

Table B.7: Summary of experimental data for glycerin under collision/separation flow conditions. Temperature was measured at 24.5°C ±2.2°C.

#	h_0 (μm)	F_{pk} (N)	v_0 (mm/s)	v_{pk} (mm/s)	t_{velpk} (ms)
1	75	-1.174	0.070	0.665	1780.2
2	77	-1.175	0.067	0.663	1713.4
3	78	-2.670	0.139	11.286	619.8
4	83	-2.665	0.157	11.440	548.4
5	84	-2.669	0.160	11.343	540.4
6	86	-2.673	0.171	11.676	516.4
7	91	-1.173	0.079	0.698	1296.4
8	94	-1.174	0.084	0.743	1202.6
9	99	-1.175	0.104	0.721	1123.6
10	101	-1.172	0.100	0.769	1046.4
11	517	0.913	-5.383	-5.383	7.0
12	519	0.912	-5.430	-5.430	6.8
13	522	0.908	-5.526	-5.526	7.2
14	523	0.908	-5.531	-5.531	7.0
15	534	0.899	-5.781	-5.781	6.8
16	562	0.877	-6.431	-6.431	6.8
17	1273	0.961	-40.506	-40.506	9.0
18	1274	0.959	-40.551	-40.551	9.0
19	1286	0.939	-40.749	-40.749	9.0
20	1332	0.887	-42.095	-42.095	9.2

Table B.8: Summary of experimental data for oil under collision/separation flow conditions. Temperature was measured at 24.5°C ±2.2°C.

#	h_0 (μm)	F_{pk} (N)	v_0 (mm/s)	v_{pk} (mm/s)	t_{velpk} (ms)
1	35	-0.725	0.038	0.196	5171.4
2	45	-0.725	0.042	0.189	3541.2
3	46	-0.724	0.040	0.183	3170.6
4	47	-0.436	0.034	0.051	1097.6
5	65	-0.723	0.058	0.201	1908.8
6	67	-1.164	0.092	1.466	863.8
7	69	0.399	-0.053	-0.058	245.4
8	69	-1.164	0.092	1.443	832.2
9	71	-1.467	0.137	3.323	586.4
10	72	-1.466	0.138	3.384	570.8
11	73	-1.163	0.108	1.432	766.2
12	82	-1.164	0.148	1.553	617.0
13	84	-1.460	0.207	3.493	441.4
14	155	0.393	-0.257	-0.257	8.8
15	174	0.677	-0.425	-0.425	8.2
16	182	-1.003	2.961	3.568	124.6
17	185	-1.001	3.126	3.620	124.6
18	189	-0.998	3.336	3.620	119.6
19	194	-0.995	3.483	3.702	110.4
20	268	0.624	-1.572	-1.572	7.6
21	271	0.622	-1.635	-1.635	7.2
22	275	0.617	-1.675	-1.675	7.4
23	407	-1.000	14.610	14.610	23.8
24	408	-0.999	14.591	14.591	23.2
25	409	-0.996	14.619	14.619	22.6
26	411	-0.989	14.693	14.693	23.2
27	511	0.757	-9.514	-9.514	7.4
28	514	0.752	-9.646	-9.646	7.8
29	519	0.746	-9.815	-9.815	7.6
30	545	0.718	-10.642	-10.642	7.6
31	559	-0.416	10.637	10.637	12.2
32	560	-0.414	10.622	10.622	12.6
33	560	-0.415	10.651	10.651	12.4
34	670	0.752	-17.123	-17.123	8.4
35	676	0.744	-17.303	-17.303	8.2

#	h_0 (μm)	F_{pk} (N)	v_0 (mm/s)	v_{pk} (mm/s)	t_{velpk} (ms)
36	679	0.462	-12.752	-12.752	8.6
37	681	0.460	-12.776	-12.776	8.6
38	685	0.457	-12.896	-12.896	8.6
39	687	0.726	-17.628	-17.628	8.2
40	690	0.451	-12.961	-12.961	8.4
41	711	-0.193	8.443	8.443	9.8
42	712	-0.192	8.468	8.468	10.0
43	713	-0.192	8.478	8.478	10.2
44	713	-0.192	8.474	8.474	10.0
45	713	-0.191	8.488	8.488	10.0
46	715	-0.190	8.489	8.489	10.2
47	971	0.174	-14.580	-14.580	9.8
48	973	0.173	-14.550	-14.550	9.6
49	974	0.099	-9.706	-9.706	9.8
50	974	0.099	-9.708	-9.708	10.2
51	975	0.099	-9.690	-9.690	9.6
52	975	0.099	-9.698	-9.698	10.0
53	975	0.099	-9.731	-9.731	9.6
54	977	0.099	-9.734	-9.734	9.6
55	979	0.170	-14.604	-14.604	9.4
56	1109	0.287	-25.857	-25.857	9.6
57	1109	0.285	-25.811	-25.811	9.6
58	1110	0.285	-25.805	-25.805	9.6
59	1122	0.265	-25.743	-25.743	9.8

Table B.9: Summary of experimental data for water under collision/separation flow conditions. Temperature was measured at 24.5°C ±2.2°C.

#	h_0 (μm)	F_{pk} (N)	v_0 (mm/s)	v_{pk} (mm/s)	t_{velpk} (ms)
1	20	-0.827	0.182	5.562	214.8
2	26	-0.747	1.023	5.657	138.8
3	27	-0.747	1.234	5.749	135.0
4	44	-0.654	5.908	5.908	63.6
5	47	-0.648	6.043	6.043	59.4
6	48	-0.647	6.094	6.094	58.4
7	54	-0.904	12.073	12.073	37.6

#	h_0 (μm)	F_{pk} (N)	v_0 (mm/s)	v_{pk} (mm/s)	t_{velpk} (ms)
8	55	-0.899	12.127	12.127	37.0
9	87	-0.848	18.581	18.581	20.6
10	90	-0.825	18.712	18.712	20.4
11	93	-0.802	18.825	18.825	19.6
12	131	-0.530	18.936	18.936	15.8
13	135	-0.519	18.988	18.988	15.8
14	140	-0.502	19.119	19.119	15.4
15	182	-0.347	18.707	18.707	14.0
16	187	-0.338	18.752	18.752	13.6
17	268	-0.201	16.917	16.917	12.6
18	274	-0.197	16.974	16.974	12.2
19	284	-0.192	16.970	16.970	12.4
20	359	0.103	-12.963	-12.963	10.8
21	361	0.147	-14.111	-14.111	11.0
22	365	0.098	-12.984	-12.984	11.2
23	365	0.081	-11.755	-11.755	10.8
24	367	0.080	-11.785	-11.785	11.2
25	388	0.073	-12.044	-12.044	11.4
26	521	0.079	-18.277	-18.277	10.8
27	525	0.078	-18.299	-18.299	11.2
28	548	0.073	-18.510	-18.510	11.4
29	682	0.072	-23.354	-23.354	11.2
30	685	0.072	-23.386	-23.386	11.0
31	690	0.071	-23.334	-23.334	11.0
32	698	0.059	-20.390	-20.390	11.0
33	699	0.064	-21.868	-21.868	11.4
34	706	0.058	-20.321	-20.321	11.0
35	709	0.047	-17.452	-17.452	11.0
36	774	0.042	-17.477	-17.477	11.4

B.3.2 Non-Newtonian Fluids

Table B.10: Summary of experimental data for XG1 under collision/separation flow conditions. Temperature was measured at 24.5°C ±2.2°C.

#	h_0 (μm)	F_{pk} (N)	v_0 (mm/s)	v_{pk} (mm/s)	t_{velpk} (ms)
1	19	-2.989	0.041	10.409	5162.8
2	25	-2.993	0.035	10.842	2067.8
3	26	-2.999	0.047	10.577	1830.6
4	27	-2.993	0.042	10.873	1461.8
5	28	-2.993	0.037	10.765	1358.0
6	44	-1.152	0.507	1.584	225.6
7	45	-1.154	0.537	1.617	207.6
8	47	-1.154	0.623	1.624	205.2
9	51	-1.153	0.818	1.712	176.6
10	115	-0.912	2.060	2.060	78.8
11	117	-0.911	2.092	2.092	71.0
12	120	-0.909	2.172	2.172	68.4
13	128	-0.909	2.231	2.231	55.0
14	207	0.588	-1.615	-1.615	23.0
15	239	-0.579	2.135	2.135	24.6
16	242	-0.574	2.207	2.207	24.2
17	244	-0.571	2.232	2.232	23.4
18	247	-0.562	2.212	2.212	23.6
19	421	0.652	-11.442	-11.442	10.4
20	424	0.649	-11.491	-11.491	10.0
21	429	0.637	-11.657	-11.657	10.0
22	433	0.532	-8.193	-8.193	9.4
23	437	0.529	-8.275	-8.275	9.4
24	441	0.516	-8.462	-8.462	9.8
25	448	0.732	-10.626	-10.626	13.0
26	449	0.384	-4.945	-4.945	6.8
27	452	0.382	-4.946	-4.946	6.8
28	458	0.385	-4.976	-4.976	7.0
29	461	0.571	-7.741	-7.741	8.2
30	464	0.398	-4.973	-4.973	7.0
31	607	-0.212	2.865	2.865	7.0
32	608	-0.211	2.895	2.895	6.8
33	614	-0.204	2.965	2.965	7.0
34	615	-0.336	9.148	9.148	9.8
35	616	-0.336	9.153	9.153	9.8

#	h_0 (μm)	F_{pk} (N)	v_0 (mm/s)	v_{pk} (mm/s)	t_{velpk} (ms)
36	620	-0.331	9.214	9.214	9.8
37	708	0.167	-3.224	-3.224	7.2
38	709	0.164	-3.257	-3.257	7.6
39	714	0.164	-3.290	-3.290	7.0
40	744	0.172	-3.366	-3.366	7.2
41	856	1.507	-50.776	-50.776	10.2
42	861	1.480	-50.496	-50.496	10.4
43	865	1.474	-50.733	-50.733	10.4
44	866	1.446	-50.185	-50.185	10.4
45	873	1.433	-50.491	-50.491	10.4
46	921	0.212	-11.167	-11.167	9.2
47	924	0.209	-11.176	-11.176	9.0
48	936	0.246	-10.837	-10.837	8.6

Table B.11: Summary of experimental data for XG2 under collision/separation flow conditions. Temperature was measured at 24.5°C ±2.2°C.

#	h_0 (μm)	F_{pk} (N)	v_0 (mm/s)	v_{pk} (mm/s)	t_{velpk} (ms)
1	7	-8.750	0.046	98.503	9455.0
2	10	-8.721	0.043	104.429	4989.6
3	10	-8.733	0.039	104.326	4810.8
4	10	-8.740	0.039	102.638	3899.0
5	13	-8.742	0.035	101.304	1698.8
6	2597	7.233	-186.379	-186.379	11.0
7	2602	9.502	-186.213	-186.213	11.0
8	2603	8.152	-186.374	-186.374	11.0
9	2605	7.294	-186.243	-186.243	11.0

Table B.12: Summary of experimental data for XG3 under collision/separation flow conditions. Temperature was measured at 24.5°C ±2.2°C.

#	h_0 (μm)	F_{pk} (N)	v_0 (mm/s)	v_{pk} (mm/s)	t_{velpk} (ms)
1	171	-2.668	128.777	128.777	12.4
2	171	-2.670	128.827	128.827	12.4
3	187	-1.957	131.163	131.163	11.8
4	187	-1.953	131.241	131.241	11.8
5	187	-1.952	131.177	131.177	11.8
6	187	-1.957	131.271	131.271	11.8
7	188	-1.943	131.179	131.179	11.8
8	203	-1.600	129.121	129.121	11.8
9	203	-1.593	129.097	129.097	11.8
10	204	-1.589	129.092	129.092	11.8
11	204	-1.588	129.082	129.082	11.8
12	204	-1.593	129.085	129.085	11.8
13	2643	-0.019	-134.438	-134.438	10.8
14	2643	-0.019	-134.365	-134.365	10.6
15	2643	-0.019	-134.398	-134.398	10.6
16	2643	-0.019	-134.431	-134.431	10.6
17	2643	-0.019	-134.459	-134.459	10.6
18	2643	-0.014	-131.371	-131.371	10.8
19	2643	-0.014	-131.397	-131.397	10.8
20	2643	-0.017	-131.331	-131.331	10.8
21	2643	-0.018	-131.315	-131.315	10.8
22	2643	-0.018	-131.312	-131.312	10.8
23	2643	-0.018	-131.323	-131.323	10.8

APPENDIX C. OSCILLATORY SQUEEZE FLOW TEST FIXTURE DRAWINGS

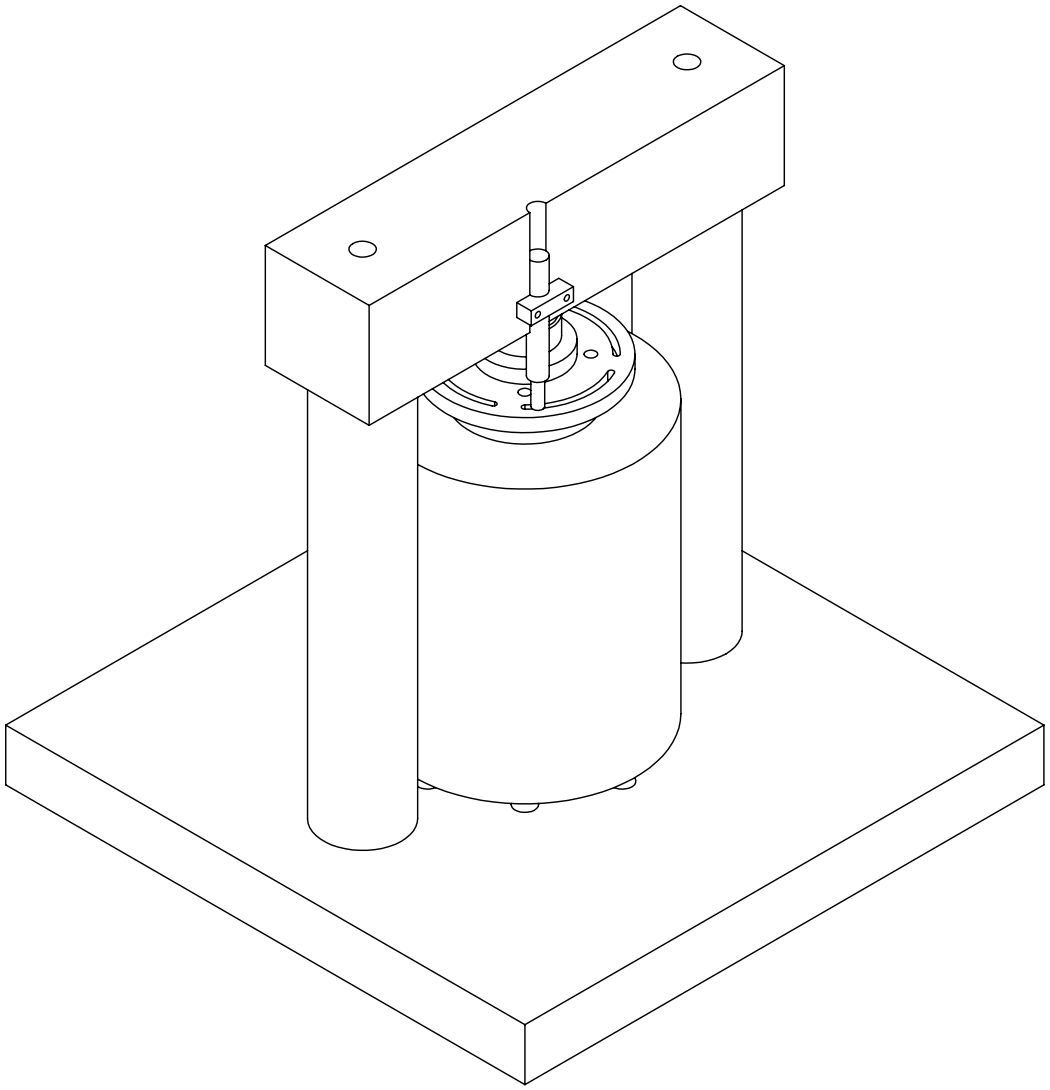

		DIMENSIONS ARE IN INCHES TOLERANCES: FRACTIONAL ± ANGULAR: MACH ± BEND ± TWO PLACE DECIMAL ± THREE PLACE DECIMAL ±		NAME	DATE
			DRAWN		
			CHECKED		
			ENG APPR.		
			MFG APPR.		
			Q.A.		
		MATERIAL	COMMENTS:		
		FINISH			
NEXT ASSY	USED ON				
APPLICATION		DO NOT SCALE DRAWING			

SIZE	DWG. NO.	REV.
A	ShakerFixture	
SCALE:1:8	WEIGHT:	SHEET 1 OF 6

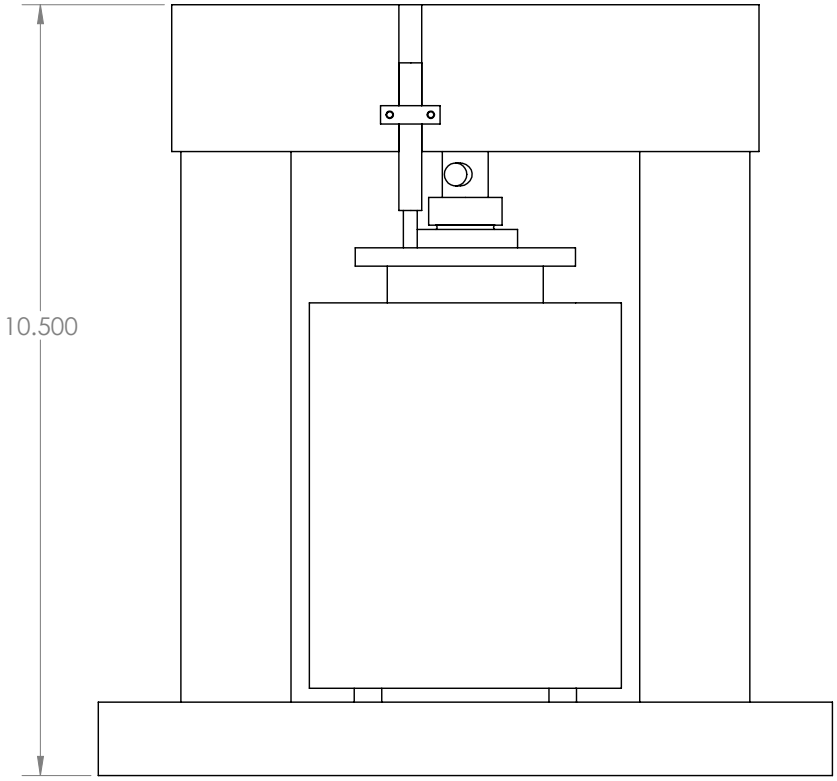

		DIMENSIONS ARE IN INCHES TOLERANCES: FRACTIONAL ± ANGULAR: MACH ± BEND ± TWO PLACE DECIMAL ± THREE PLACE DECIMAL ±		NAME	DATE
			DRAWN		
			CHECKED		
			ENG APPR.		
			MFG APPR.		
		MATERIAL	Q.A.		
			COMMENTS:		
NEXT ASSY	USED ON	FINISH			
APPLICATION		DO NOT SCALE DRAWING			

SIZE	DWG. NO.	REV.
A	ShakerFixture	
SCALE:1:8	WEIGHT:	SHEET 2 OF 6

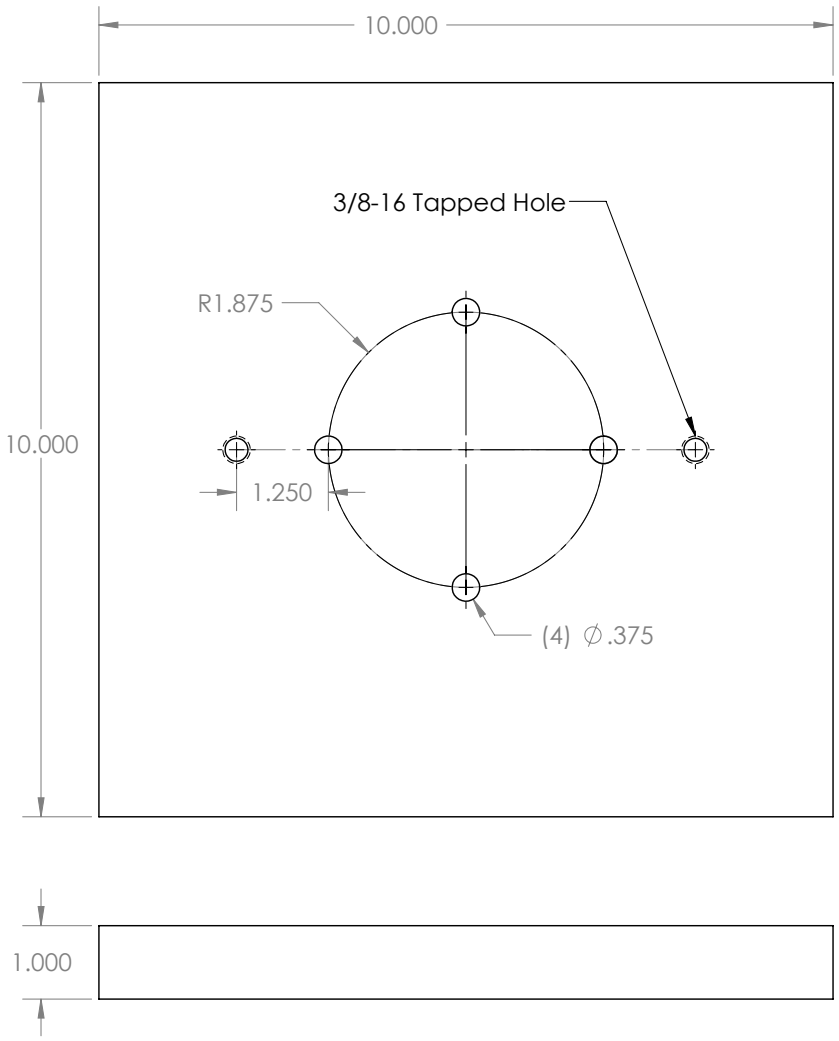

		DIMENSIONS ARE IN INCHES TOLERANCES: FRACTIONAL ± ANGULAR: MACH ± BEND ± TWO PLACE DECIMAL ± THREE PLACE DECIMAL ±		NAME	DATE
			DRAWN		
			CHECKED		
			ENG APPR.		
			MFG APPR.		
		MATERIAL	Q.A.		
			COMMENTS:		
NEXT ASSY	USED ON	FINISH			
APPLICATION		DO NOT SCALE DRAWING			

SIZE	DWG. NO.	REV.
A	ShakerFixture	
SCALE:1:8	WEIGHT:	SHEET 3 OF 6

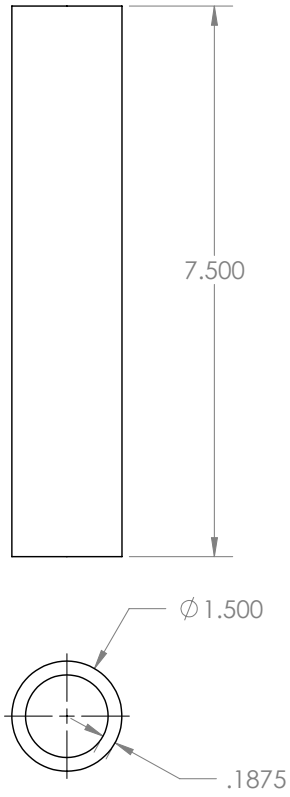

		DIMENSIONS ARE IN INCHES TOLERANCES: FRACTIONAL ± ANGULAR: MACH ± BEND ± TWO PLACE DECIMAL ± THREE PLACE DECIMAL ±		NAME	DATE
			DRAWN		
			CHECKED		
			ENG APPR.		
			MFG APPR.		
			Q.A.		
		MATERIAL	COMMENTS:		
		FINISH			
NEXT ASSY	USED ON				
APPLICATION		DO NOT SCALE DRAWING			

SIZE	DWG. NO.	REV.
A	ShakerFixture	
SCALE:1:8	WEIGHT:	SHEET 4 OF 6

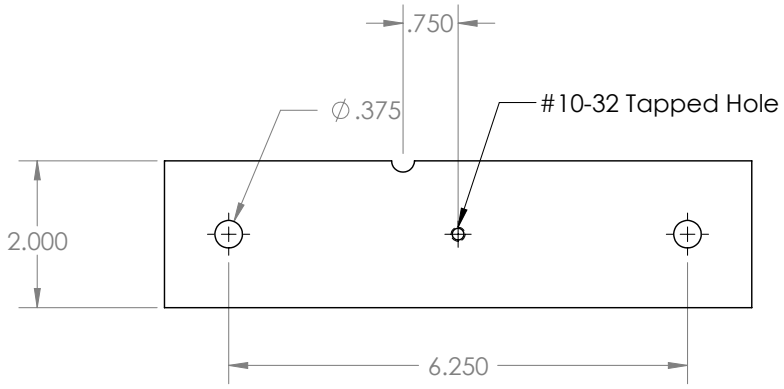

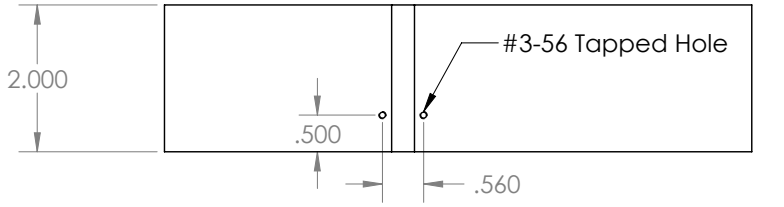

		DIMENSIONS ARE IN INCHES TOLERANCES: FRACTIONAL ± ANGULAR: MACH ± BEND ± TWO PLACE DECIMAL ± THREE PLACE DECIMAL ±		NAME	DATE
			DRAWN		
			CHECKED		
			ENG APPR.		
			MFG APPR.		
		MATERIAL	Q.A.		
			COMMENTS:		
NEXT ASSY	USED ON	FINISH			
APPLICATION		DO NOT SCALE DRAWING			

SIZE	DWG. NO.	REV.
A	ShakerFixture	
SCALE:1:8	WEIGHT:	SHEET 5 OF 6

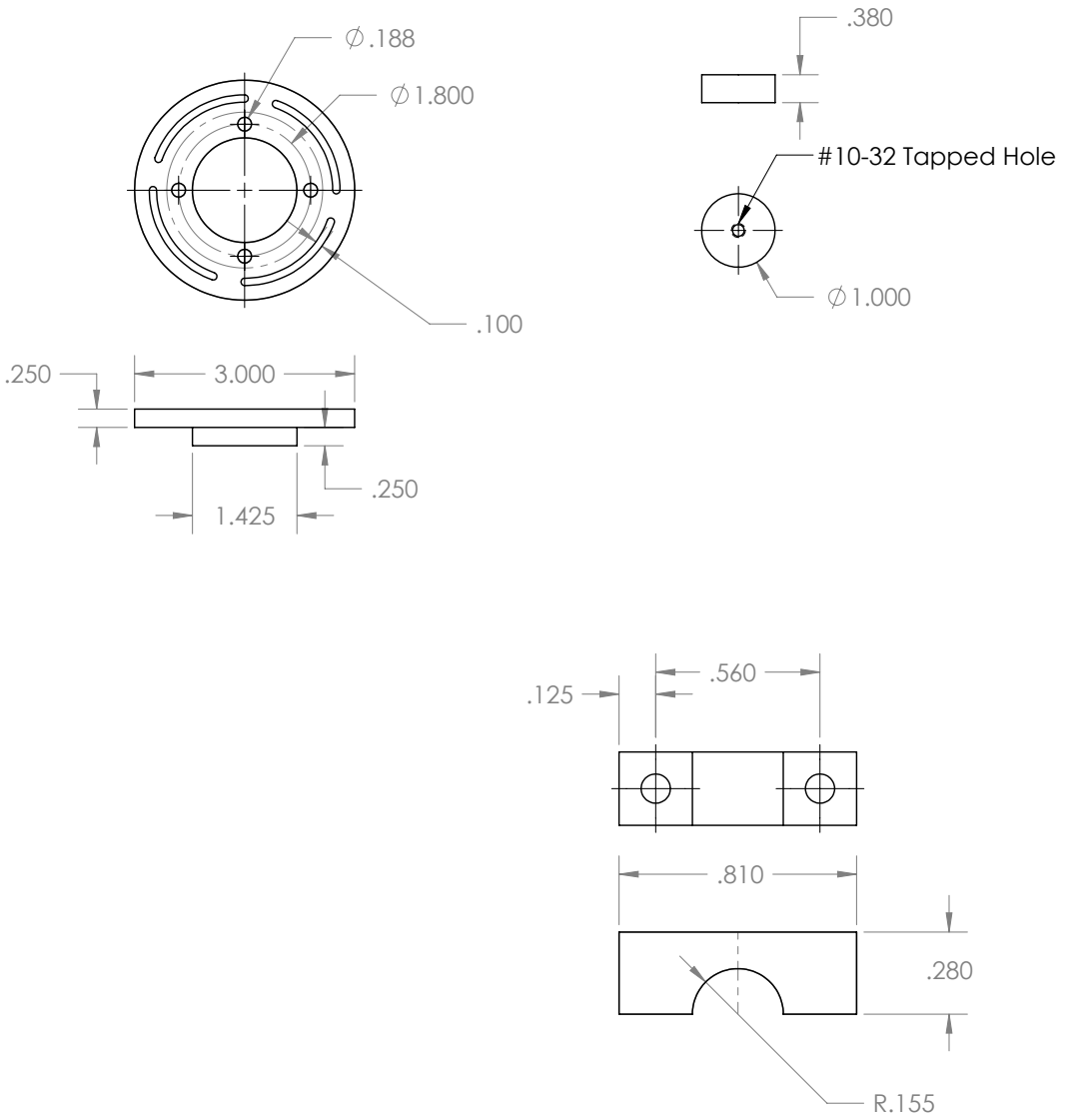

		DIMENSIONS ARE IN INCHES TOLERANCES: FRACTIONAL ± ANGULAR: MACH ± BEND ± TWO PLACE DECIMAL ± THREE PLACE DECIMAL ±		NAME	DATE
			DRAWN		
			CHECKED		
			ENG APPR.		
			MFG APPR.		
		MATERIAL	Q.A.		
			COMMENTS:		
NEXT ASSY	USED ON	FINISH			
APPLICATION		DO NOT SCALE DRAWING			

SIZE	DWG. NO.	REV.
A	ShakerFixture	
SCALE:1:8	WEIGHT:	SHEET 6 OF 6

APPENDIX D. EQUIPMENT TESTING

D.1 Equipment Testing

Table D.1:

Test	Additional information	Summary of Results
Compared LVDT displacement with high speed camera while LVDT in contact with the surface of a n elliptical cam.	Freq range (5-50Hz, limited by inertia of LVDT armature, above 50Hz armature comes off cam surface)	Verified that LVDT and high-speed camera are triggering and recording synchronously across broad frequency range.
Checked LabVIEW for triggering delays		LabVIEW documentation indicates a 38.9 data point delay between digital triggering and converted analog data and 0 data point delay for analog triggering. Analog triggering was used throughout experimental testing.
Force gauge impact timing	High-speed images of an object impacting the force gauge and comparison of high-speed image timing with measured force timing	In phase
Calibration of LVDT with range of feeler gauge thicknesses		LVDT was calibrated

Test	Additional information	Summary of Results
Tests with aluminum cylinder in place of force gauge	Moved force gauge to top of beam, Fastened an aluminum cylinder in place where force gauges was. Performed testing with shaker and fixture plates in contact and sinusoidal input to shaker. Also, with plates not in contact and compared measured forces, accelerometer measurements and LVDT measurements with those taken with force gauge in normal location.	Force gauge measurements when mounted to top of beam are negligibly small even when largest forces would be experienced by the aluminum cylinder dummy force gauge.
Looked at accelerometer data with test fixture on test stand with and without cinder blocks on test stand.		Generally, increasing number of concrete masonry blocks (mass) reduced peak amplitude of accelerometer data on test fixture.
Looked at accelerometer data for test fixture mounted on test stand and on massive table		Peak amplitudes measured were comparable on both setups.
Compared data taken on isolation table with data taken on test stand with 5 concrete masonry blocks on test stand base.		Measurements were in very good agreement.
Eccentric force measurement effects	An object was placed on the edge between the upper and lower plates to create an eccentric loading on the force gauge.	Virtually no difference in the force measurement was observed.

APPENDIX E. CODE

The following code gives an example of how Equation 2.6 was implemented. The purpose of giving this example was to demonstrate that there were no errors associated with the implementation of the equation that contributed to the discrepancy between the measured and calculated film force.

```
%%%%% Define constants
dt = 1/5000;     % timestep (sec)

R0 = 0.0127;     % Plate radius (m)
mu = 0.060;      % Fluid viscosity (Pa*s)
rho = 894;       % Fluid density (kg/m^3)
alph = 1.54;     % Velocity profile correction factor

h0 = 37.6e-6;    % Mean film thickness (m)
A = 1.2e-6;      % Displacement Amplitude (m)
f = 110;         % Displacement frequency (Hz)
w = 2*pi*f;      % Displacement frequency (rad/sec)

%%%%% Create time array
t = 0:dt:0.1;

%%%%% Create film thickness and its derivatives (sinusoidal)
h = A*sin(w*t) + h0;
hdot = A*w*cos(w*t);
hdotdot = -A*w^2*sin(w*t);

%%%%% Calculate film force
Ffilm = -pi.*R0.^4./4.*(6.*mu.*hdot./h.^3.*(1-(1+3.*alph./2) ./ ...
            (12.*mu).*rho.*hdot.*h)+rho.*hdotdot./(2.*h));

%%%%% Plot film force vs. time
plot(t,Ffilm);

%%%%% Get peak film force value
Fpk = (max(Ffilm) - min(Ffilm)) / 2;
```

APPENDIX F. SYNTHETIC HEMILARYNX FORCE GAUGE TEST SETUP DRAWINGS

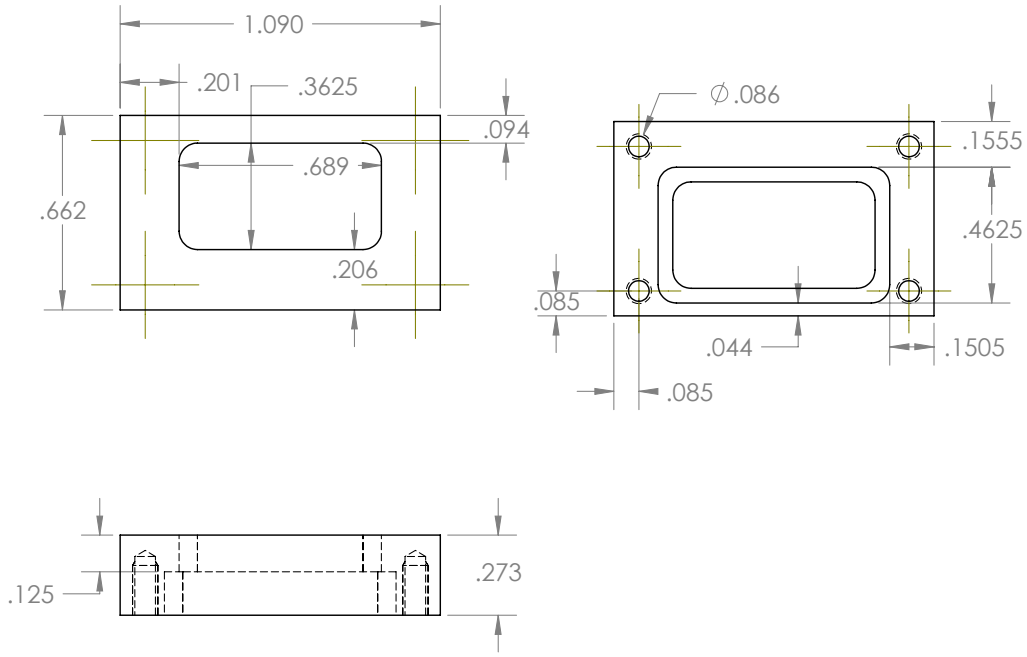

		DIMENSIONS ARE IN INCHES TOLERANCES: FRACTIONAL ± ANGULAR: MACH ± BEND ± TWO PLACE DECIMAL ± THREE PLACE DECIMAL ±		NAME	DATE
			DRAWN		
			CHECKED		
			ENG APPR.		
			MFG APPR.		
		MATERIAL	Q.A.		
			COMMENTS:		
NEXT ASSY	USED ON	FINISH			
APPLICATION		DO NOT SCALE DRAWING			

SIZE	DWG. NO.	REV.
A	ForceGaugeBlockFacePlate	
SCALE:2:1	WEIGHT:	SHEET 1 OF 1

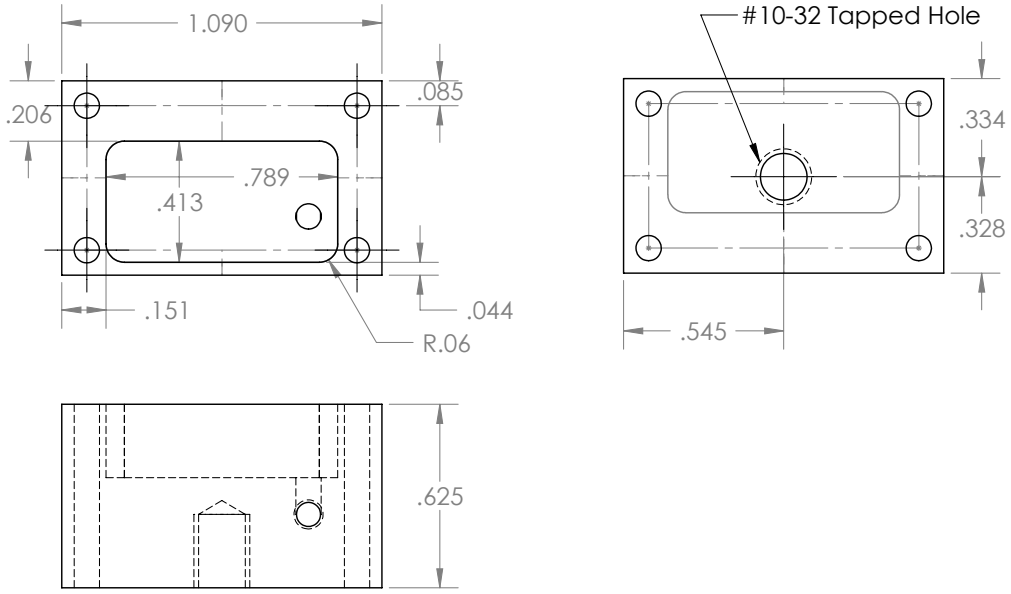

		DIMENSIONS ARE IN INCHES TOLERANCES: FRACTIONAL ± ANGULAR: MACH ± BEND ± TWO PLACE DECIMAL ± THREE PLACE DECIMAL ±		NAME	DATE
			DRAWN		
			CHECKED		
			ENG APPR.		
			MFG APPR.		
		MATERIAL	Q.A.		
			COMMENTS:		
NEXT ASSY	USED ON	FINISH			
APPLICATION		DO NOT SCALE DRAWING			

SIZE	DWG. NO.	REV.
	AForceGaugeSpacerBody	
SCALE:2:1	WEIGHT:	SHEET 1 OF 1

APPENDIX G. UNCERTAINTY IN OSCILLATORY SQUEEZE FLOW CALCULATIONS

Equation 2.6 is reproduced below for convenience

$$F_y = \frac{\pi R_0^4}{4}\left[\frac{6\mu\dot{h}}{h^3}\left(1-\frac{1+\frac{3\alpha}{2}}{12\mu}\rho h\dot{h}\right)+\frac{\rho\ddot{h}}{2h}\right] \tag{G.1}$$

where R_0 is the plate radius, μ is the fluid dynamic viscosity, α is the velocity profile correction factor, and h, $\dot{h}$, and $\ddot{h}$ are the film thickness and its first and second temporal derivatives, respectively.

A sinusoidal displacement of the lower moving plate is assumed which gives the film thickness, h, as a function of time, t, and its temporal derivatives

$$h(t) = A\sin(\omega t) + h_0 \tag{G.2}$$

$$\dot{h}(t) = A\omega\cos(\omega t) \tag{G.3}$$

$$\ddot{h}(t) = -A\omega^2\sin(\omega t) \tag{G.4}$$

where A is the amplitude of displacement, ω is the angular frequency (equal to $2\pi f$, f is frequency of oscillation), and h_0 is the mean film thickness. Thus, the parameters A, h_0, and ω, which were all measured from the displacement sensor (e.g., LVDT) completely determine the film thickness waveform and its temporal derivatives.

Substituting equations G.2 through G.4 into 2.6 in order to put the expression in terms of h_0 and A instead of h and its derivatives gives

$$F_y = \frac{\pi R_0^4}{4}\left[\frac{6\mu\left(A\omega\cos(\omega t)\right)}{\left(A\sin(\omega t)+h_0\right)^3}\left(1-\frac{1+\frac{3\alpha}{2}}{12\mu}\rho\left(A\sin(\omega t)+h_0\right)\left(A\omega\cos(\omega t)\right)\right)+\frac{\rho\left(-A\omega^2\sin(\omega t)\right)}{2\left(A\sin(\omega t)+h_0\right)}\right]. \tag{G.5}$$

Substituting $S = \sin(\omega t)$ and $C = \cos(\omega t)$ to simplify the expression gives

$$F_y = \frac{\pi R_0^4}{4}\left[\frac{6\mu\,(A\omega C)}{(AS+h_0)^3}\left(1-\frac{1+\frac{3\alpha}{2}}{12\mu}\rho\,(AS+h_0)\,(A\omega C)\right)+\frac{\rho\,(-A\omega^2 S)}{2\,(AS+h_0)}\right], \tag{G.6}$$

The partial derivatives of Eq. G.6 with respect to h_0, μ, and A respectively, are

$$\begin{aligned}\frac{\partial F_y}{\partial h_0} = \frac{\pi R_0^4}{4}\Bigg[&-\frac{18\mu\omega AC}{(AS+h_0)^4}\left(1-\frac{\left(\frac{3\alpha}{2}+1\right)\omega\rho AC\,(AS+h_0)}{12\mu}\right)\\ &+\frac{\omega^2\rho AS}{2(AS+h_0)^2}-\frac{\left(\frac{3\alpha}{2}+1\right)\omega^2\rho A^2C^2}{2(AS+h_0)^3}\Bigg]\end{aligned} \tag{G.7}$$

$$\frac{\partial F_y}{\partial \mu} = \frac{\pi R_0^4}{4}\left[\frac{6\omega AC\left(1-\frac{\left(\frac{3\alpha}{2}+1\right)\omega\rho AC\,(AS+h_0)}{12\mu}\right)}{(AS+h_0)^3}+\frac{\left(\frac{3\alpha}{2}+1\right)\omega^2\rho A^2C^2}{2\mu\,(AS+h_0)^2}\right] \tag{G.8}$$

$$\begin{aligned}\frac{\partial F_y}{\partial A} = \frac{\pi R_0^4}{4}\Bigg[&\frac{6\mu\omega C}{(AS+h_0)^3}\left(1-\frac{\omega\rho AC}{12\mu}\left(\frac{3\alpha}{2}+1\right)(AS+h_0)\right)\\ &-\frac{18\mu\omega ACS}{(AS+h_0)^4}\left(1-\frac{\omega\rho AC}{12\mu}\left(\frac{3\alpha}{2}+1\right)(AS+h_0)\right)\\ &+\frac{6\mu\omega AC}{12\mu\,(AS+h_0)^3}\left(-\left(\frac{3\alpha}{2}+1\right)\omega\rho C\,(AS+h_0)-\left(\frac{3\alpha}{2}+1\right)\omega\rho ACS\right)\\ &-\frac{\omega^2\rho S}{2\,(AS+h_0)}+\frac{\omega^2\rho AS^2}{2(AS+h_0)^2}\Bigg]\end{aligned} \tag{G.9}$$

Then the propagated error, E, is

$$E = \sqrt{\left(\frac{\partial F_y}{\partial h_0}\Delta h_0\right)^2+\left(\frac{\partial F_y}{\partial \mu}\Delta\mu\right)^2+\left(\frac{\partial F_y}{\partial A}\Delta A\right)^2} \tag{G.10}$$

where Δh_0 is error in the measurement of h_0, $\Delta\mu$ is error in the measurement of μ, and ΔA is the error in the measurement of A.

The error in the measurement of the mean film thickness, h_0, and the amplitude, A, came from the measurement uncertainty of the LVDT which was reported by the manufacturer to be 0.25% of the full-scale of the LVDT. The full-scale of the LVDT was 1000 μm which gives an uncertainty of ±2.5 μm. Therefore,

$$\Delta h_0 = \Delta A = \pm 2.5\,\mu\text{m} \tag{G.11}$$

The error in viscosity, $\Delta\mu$, was found by calculating the error propagated through the viscosity curve-fit functions as follows

$$\Delta\mu = \sqrt{\left(\frac{\partial\mu}{\partial T}\Delta T\right)^2}. \tag{G.12}$$

where, μ, the curve-fit function for olive oil viscosity as a function of temperature is given in Appendix A as

$$\mu = 5.39E^{-5}T^2 - 5.2803E^{-3}T + 0.15983. \tag{G.13}$$

which gives

$$\frac{\partial\mu}{\partial T} = 2\left(5.39E^{-5}T\right) - 5.2803E^{-3} \tag{G.14}$$

All olive oil data taken had measured temperatures between 16 and 27°C. Figure G.1 shows the error and percent error of calculated viscosity over the measured temperature range.

The propagation of error is then plotted in Fig. G.2 by evaluating Eq. G.10 for each olive oil case with a mean film thickness less than 91 μm (since this is the region where the largest errors in calculated force are observed). The film force was calculated for one full cycle using the measured mean film thickness, measured amplitude of film thickness oscillation, measured frequency of plate oscillation, fluid density, and calculated fluid dynamic viscosity. The peak calculated force amplitude was obtained by taking half of the difference between the maximum and minimum calculated forces for the cycle (the same method used to measure the force amplitude or peak force reported in Ch. 3). The propagated uncertainty due to the measurement of amplitude accounts for about 80% of the total uncertainty. The propagated uncertainty from measured mean film thickness and calculated viscosity are about the same and together account for about 20% of the

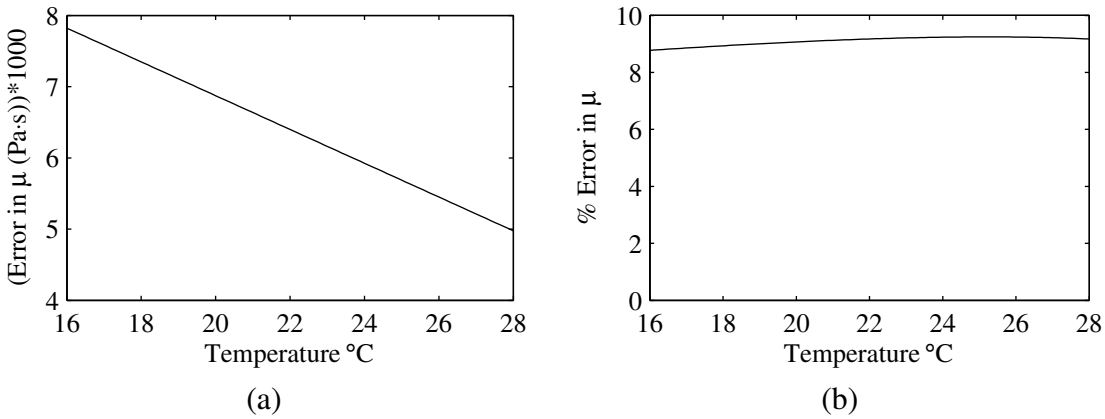

(a) (b)

Figure G.1: Error in olive oil viscosity as a function of measured temperature. Varies from 0.0078 Pa·s at 16°C to 0.0050 Pa·s at 28°C. The percent error in calculated viscosity varies between 8.8% and 9.2% over the temperature range.

total uncertainty. Propagated uncertainty from density was neglected since even with an error of 25% in density, the propagated uncertainty accounted for less than 0.2% of the total uncertainty. The figure shows that the propagated uncertainty accounts for all of the error observed in 29 of the 31 cases. Therefore, the large errors between the peak calculated force and the peak measured force are the result of measurement uncertainty in the measurement of mean film thickness, oscillatory film thickness amplitude, and fluid temperature.

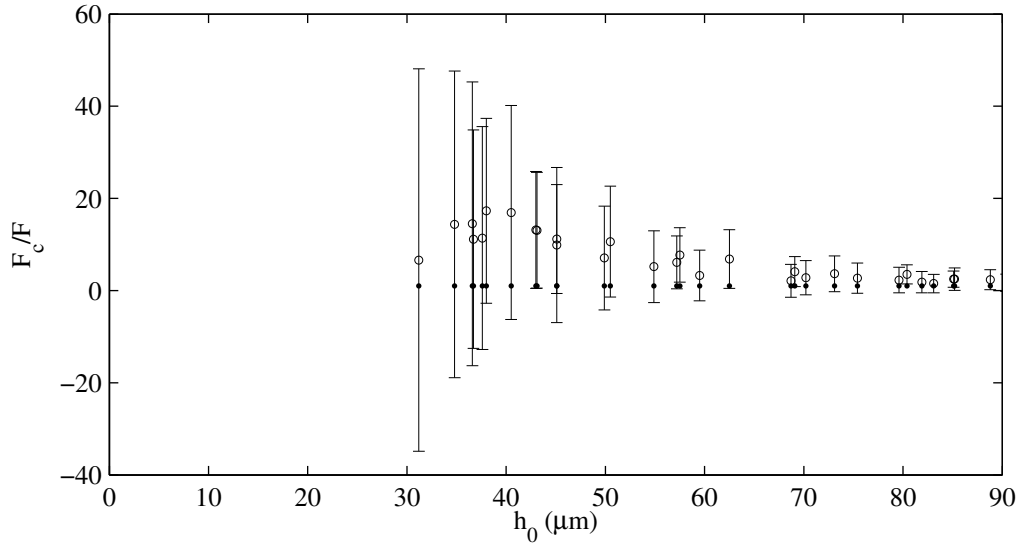

Figure G.2: Error propagation of olive oil data with mean film thickness less than 91 μm. The calculated force is shown as a circle with error bars indicating the error propagated through the force calculation. The solid dot shows the measured force for each case.

APPENDIX H. SENSOR SPECIFICATIONS AND ERROR

H.1 Sensor Specifications

Table H.1: Summary of sensors specifications.

Measurement	Description	Manufacturer	Model No.	Range	Uncertainty	Comments
Force	Piezoelectric	PCB Electronics	208C01	45 N	0.45 N	50 sec discharge time constant, AC-coupled
Pressure	Silicon	Omega	PX138-001D5V	> 7000 kPa	±6.9 kPa	
Sound Pressure Level	1/4” Mic	Larson-Davis	2520	4-80 kHz	0.2 Hz	Uncertainty based on FFT frequency discrimination for 5 seconds audio sampled at 40 kHz.
Sound Pressure Level	1/4” Mic	Larson-Davis	2520	> 164 dB	-48 ± 2.4 dB	
Displacement	LVDT	Honeywell	S5	1000 μm	2.5 μm	
Air Flow Rate	Variable Area	Omega	FL4217	100 SCFH	±5 SCFH	

APPENDIX I. SYNTHETIC MODEL TESTING ORDER

Table I.1: Hemilarynx random run order

ID	Set	Group	Fluid	Pressure
1	1	1	Dry	1.6
2	1	1	Dry	1.5
3	1	1	Dry	1.4
4	1	1	Dry	1.7
5	1	1	Dry	1.8
6	1	1	Dry	1.9
7	1	2	Water	1.9
8	1	2	Water	1.8
9	1	2	Water	1.6
10	1	2	Water	1.5
11	1	2	Water	1.7
12	1	2	Water	1.4
13	1	3	Dry	1.8
14	1	3	Dry	1.7
15	1	3	Dry	1.5
16	1	3	Dry	1.6
17	1	3	Dry	1.4
18	1	3	Dry	1.9
19	1	4	Olive Oil	1.9
20	1	4	Olive Oil	1.8
21	1	4	Olive Oil	1.7
22	1	4	Olive Oil	1.5
23	1	4	Olive Oil	1.6
24	1	4	Olive Oil	1.4
25	1	5	Dry	1.8
26	1	5	Dry	1.5
27	1	5	Dry	1.4
28	1	5	Dry	1.6
29	1	5	Dry	1.9
30	1	5	Dry	1.7
31	1	6	XG2	1.55
32	1	6	XG2	1.6
33	1	6	XG2	1.8
34	1	6	XG2	1.7
35	1	6	XG2	1.5
36	1	6	XG2	1.9
37	1	7	Dry	1.7
38	1	7	Dry	1.4
39	1	7	Dry	1.6
40	1	7	Dry	1.5
41	1	7	Dry	1.8
42	1	7	Dry	1.9
43	1	8	Glycerin	1.4
44	1	8	Glycerin	1.5
45	1	8	Glycerin	1.6
46	1	8	Glycerin	1.8
47	1	8	Glycerin	1.9
48	1	8	Glycerin	1.7
49	1	9	Dry	1.6
50	1	9	Dry	1.8
51	1	9	Dry	1.9
52	1	9	Dry	1.4
53	1	9	Dry	1.7
54	1	9	Dry	1.5
55	1	10	XG1	1.8
56	1	10	XG1	1.6
57	1	10	XG1	1.5
58	1	10	XG1	1.7
59	1	10	XG1	1.9
60	1	10	XG1	1.4
61	1	11	Dry	1.4
62	1	11	Dry	1.6
63	1	11	Dry	1.9
64	1	11	Dry	1.5
65	1	11	Dry	1.8
66	1	11	Dry	1.7
67	2	12	Oil	1.9
68	2	12	Oil	1.7
69	2	12	Oil	1.4
70	2	12	Oil	1.8
71	2	12	Oil	1.6
72	2	12	Oil	1.5
73	2	13	Dry	1.9
74	2	13	Dry	1.6